



HAL
open science

Experimental determination of the incorporation of Th into orthophosphates and the resetting of geochronological systems of monazite

Anne-Magali Seydoux-Guillaume

► **To cite this version:**

Anne-Magali Seydoux-Guillaume. Experimental determination of the incorporation of Th into orthophosphates and the resetting of geochronological systems of monazite. Applied geology. Technische Universität Berlin, 2001. English. NNT : . tel-00007675

HAL Id: tel-00007675

<https://theses.hal.science/tel-00007675>

Submitted on 7 Dec 2004

HAL is a multi-disciplinary open access archive for the deposit and dissemination of scientific research documents, whether they are published or not. The documents may come from teaching and research institutions in France or abroad, or from public or private research centers.

L'archive ouverte pluridisciplinaire **HAL**, est destinée au dépôt et à la diffusion de documents scientifiques de niveau recherche, publiés ou non, émanant des établissements d'enseignement et de recherche français ou étrangers, des laboratoires publics ou privés.

Experimental determination of the incorporation of Th into orthophosphates and the resetting of geochronological systems of monazite

Vorgelegt von

Dipl. Geol. **Anne-Magali SEYDOUX-GUILLAUME**

an der Fakultät VI

- Bauingenieurwesen und Angewandte Geowissenschaften -
der **Technischen Universität Berlin**

zur Erlangung des akademischen Grades

Doktorin der Naturwissenschaften

- Dr. rer. nat. -

genehmigte Dissertation

Berichter: Prof. Dr. **G. Franz**
Berichter: Prof. Dr. **W. Heinrich**
Berichter: Prof. Dr. **J.M. Montel**

Tag der wissenschaftlichen Aussprache: **15. Oktober 2001**

Berlin 2001

D83

Table of contents

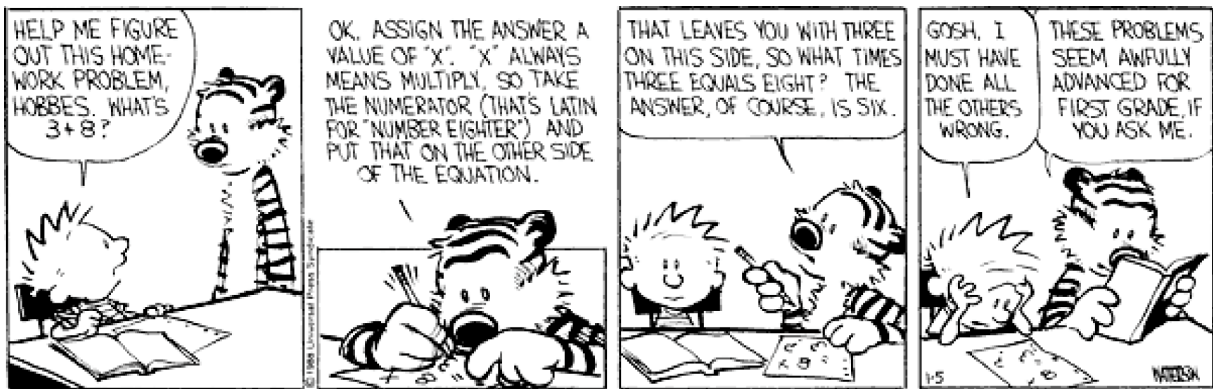


Table of contents

ABSTRACT - ZUSAMMENFASSUNG - RESUME	1
INTRODUCTION	4
CHAPTER I - Th partitioning between monazite and xenotime	
An experimental determination of the Th partitioning between monazite and xenotime using Analytical Electron Microscopy	12
• Abstract	12
• Introduction	13
• Experimental and analytical techniques	15
- <i>Starting materials</i>	15
- <i>Experimental procedure</i>	15
- <i>Analytical Electron Microscopy (AEM)</i>	17
- <i>X-ray diffraction (XRD)</i>	20
• Results	20
- <i>Compositions of monazite and xenotime determined by AEM</i>	23
- <i>Rietveld refinement results and composition-volume relationships</i>	25
• Discussion	29
- <i>A tentative diagram of phase relations in the ternary system</i>	
<i>CePO₄-YPO₄-ThSiO₄</i>	29
- <i>The monazite-xenotime thermobarometer in presence of ThSiO₄</i>	31
• Concluding remarks	33
• Acknowledgements	34
• References	34
CHAPTER II - Structure of a natural monazite: behaviour under heating	
An XRD, TEM and Raman study of experimental annealing of natural monazite	38
• Abstract	38
• Introduction	39
• Experimental	42
- <i>Starting material</i>	42
- <i>Annealing experiments</i>	42
- <i>Analytical methods</i>	44
XRD	44
TEM	45
Raman analysis	45

Cathodoluminescence	45
● Results	46
- <i>X-ray diffraction analysis</i>	46
- <i>Selected area diffraction and HRTEM observations</i>	50
- <i>Dark field images</i>	50
- <i>Raman measurements</i>	53
- <i>Cathodoluminescence</i>	53
● Discussion	53
- <i>Interpretation of the results</i>	53
- <i>Comparison with previous studies</i>	60
- <i>Differences between monazite and zircon</i>	61
- <i>Applications for geochronology</i>	61
- <i>Implications for nuclear waste</i>	62
● Conclusions	63
● Acknowledgements	64
● References	64
CHAPTER III - Resetting of U-Pb isotopic geochronological system	
An experimental resetting of the U-Th-Pb systems in monazite	70
● Abstract	70
● Introduction	71
● Sample selection and description, and experimental procedure	75
● Analytical methods	77
● Results	78
- <i>Grain-surface morphology</i>	78
- <i>Modifications of chemical compositions</i>	80
- <i>Isotopic modifications</i>	84
● Discussion	86
● Conclusions	90
● Acknowledgements	91
● Appendix: SIMS analytical details	91
● References	92
CONCLUSIONS	98
REFERENCES	101
ACKNOWLEDGEMENTS	109

Abstract

Zusammenfassung

Résumé

“La terre nous en apprend plus long sur nous mêmes que tous les livres. Parce qu'elle nous résiste.
L'homme se découvre quand il se mesure avec l'obstacle.”
Antoine de Saint-Exupéry - *Terre des homme*

Abstract

This PhD thesis is divided into three parts: (1) the experimental incorporation of Th in monazite and xenotime, (2) the behaviour of the monazite structure under temperature-induced healing, and (3) the experimental resetting of the U-Pb geochronological system in monazite.

(1) The Th distribution between monazite and xenotime as a result of the Th + Si = REE + P substitution mechanism was experimentally determined in the T-P-range of 600 to 1100°C and 2Kbar. Starting mixtures consisted of gels and were composed of equal amounts of CePO₄ and YPO₄ with addition of 10, 20 and 50 mole % of ThSiO₄. Run products were analysed using AEM and XRD. At all temperatures, the ThSiO₄ component is partitioned almost exclusively into monazite for a ThSiO₄ component of 10 and 20 mole %. Xenotime is apparently ThSiO₄-free. In the T-range 600°C-900°C and for ThSiO₄ = 50 mole %, thorite is additionally formed indicating ThSiO₄ saturation within monazite at these conditions. At 1000°C, only monazite and a small amount of xenotime crystallised. No thorite was observed.

(2) The healing of radiation damage in a natural and chemically homogeneous concordant (474±1 Ma) monazite has been experimentally investigated (500-1200°C/~7days). XRD, TEM, Raman microprobe and Cathodoluminescence analysis were performed. The unheated monazite has a mosaic structure consisting of two domains corresponding to two monazite crystals with different lattice parameters. (A) domains correspond to well-crystallised areas where He atoms are trapped, thus inducing their lattice expansion. (B) domains are interpreted to exhibit a He-free distorted monazite crystal lattice which can be referred to old alpha-recoil tracks. With increasing temperature, He diffuses out of the monazite lattice, thus inducing its relaxation. Additionally, the nm-sized defect domains (B) are getting healed. The complete healing is achieved at 900°C after 7 days.

(3) In order to investigate the influence of fluid composition and temperature on resetting, abraded fragments (200-400 µm) from monazite used in (2) were experimentally treated (800-1000°C/14-39 days) within solutions of different compositions (H₂O up to 1200°C/5 days, NaCl, SrCl₂ CaCl₂-fluids and a Pb-spike-fluid). Products were analysed using SEM, EMP, SIMS and ID-TIMS. For all runs, EMP traverses revealed no Pb-diffusion profiles. Significant overgrowths of newly formed monazite occurred only in the 1000°C experiments when either CaCl₂ or Pb-bearing fluids were present. For CaCl₂, inherited core and newly formed Ca-rich and Pb-free monazite rim were produced by dissolution/precipitation. Significant discordancy was only observed when grains were treated with SrCl₂ (16%) and CaCl₂ (68%) solutions at 1000°C. Finally, experiments performed in the presence of Pb-standard produced sub-concordant monazite with a ²⁰⁷Pb/²⁰⁶Pb apparent age older than prior to the experiment indicating Pb-contamination by the fluid.

Zusammenfassung

Die vorgelegte Dissertation beschäftigt sich mit (1) der Th Verteilung zwischen Monazit und Xenotim, (2) der Veränderung der Monazit Struktur beim Aufheizen, und (3) dem „Resetting“ des U-Pb Systems in Monaziten.

(1) Die Th Verteilung zwischen Monazit und Xenotim wurde, als Resultat der Th + Si = REE + P Substitution, experimentell (600-1100°C/2 kbar) untersucht. Dazu wurden Gele mit den gleichen Gehalten an CePO₄ und YPO₄ plus 10, 20 und 50 Mol % ThSiO₄ als Anfangsmaterial benutzt. Nach den Experimenten wurden die Produkte mit AEM und XRD analysiert. Für alle Temperaturen und für Ausgangszusammensetzungen von 10 und 20 Mol % ThSiO₄ wird ThSiO₄ fast vollständig in Monazit eingebaut. Für 50 Mol % ThSiO₄, kristallisiert zwischen 600° und 900°C Thorit. Das belegt, daß bei diesen Bedingungen Monazit an ThSiO₄ gesättigt ist. Bei 1000°C kristallisierten Monazit, wenig Xenotim und kein Thorit.

(2) Die Ausheilung von Strahlungsdefekten in einem natürlichen, homogenen, bei 474 ± 1 Ma konkordanten Monazit, wurde unter Verwendung von XRD, TEM, Raman und Kathodolumineszenz experimentell untersucht (500-1200°C/~7Tage). Der unbehandelte Monazit besteht aus einem Mosaik zweier Domäentypen (A) und (B), die zwei Monaziten mit unterschiedlichen Gitterkonstanten entsprechen. Die Domänen (A) entsprechen gut kristallisierten Bereichen, in denen He Atome, die eine Gitterexpansion induzieren, eingeschlossen sind. Die Domänen (B) entsprechen einem beschädigten Gitter (ohne He), dessen Defekte durch Alpha-Rückstoß Nuclei verursacht wurden. Während der Ausheilung, diffundiert das He aus dem Monazit-Gitter und induziert eine Gitterrelaxation. Gleichzeitig werden die defektreichen Domänen (B) ausgeheilt. Die komplette Heilung ist bei 900 nach 7 Tagen erreicht.

(3) Um den Einfluß verschiedener Flüssigkeitszusammensetzungen und Temperaturen auf den Prozess des „Resettings“ in Monazit zu untersuchen, wurden im Luftstrom gerundete Partikel (200-400 µm) des in (2) verwendeten Monazit experimentell (800-1000°C/14-39 Tage) in verschiedenen Lösungen (H₂O bis 1200°C/5 Tage, NaCl, SrCl₂, CaCl₂, und „Pb-spike“) behandelt. Die Produkte wurden mit REM, EMP, SIMS und ID-TIMS analysiert. Für alle Experimente wurden mit EMP keine Pb Diffusionsprofile nachgewiesen. Signifikantes Aufwachsen von Monazit wurde nur bei 1000°C, in CaCl₂ oder „Pb-spike“ haltigen Experimenten beobachtet. In CaCl₂-Lösungen erfolgte das Aufwachsen von neuem Monazit auf alten Monazitkörnern entsprechend einem Auflösungs/Ausfällungs Mechanismus. Signifikante Diskordanz wurde nur für den bei 1000°C in SrCl₂ (16%) und CaCl₂ (68%)-Lösungen ausgesetzten Monazit beobachtet. Monazite, die mit „Pb-spike“ Lösungen koexistierten, zeigen nach den Experimenten höhere ²⁰⁷Pb/²⁰⁶Pb Alter.

Résumé

Cette thèse présente les résultats d'étude expérimentales sur (1) le partage du Th entre la monazite et le xenotime, (2) l'effet du recuit sur la structure de la monazite ainsi que (3) la remise à zéro des systèmes géochronologiques U-Pb dans la monazite.

(1) Le partage du Th entre la monazite et le xenotime a été déterminé expérimentalement (600-1100°C/2Kbar) en considérant le mécanisme de substitution suivant: $\text{Th} + \text{Si} = \text{REE} + \text{P}$. Le matériel de départ est un gel constitué d'un mélange de CePO_4 et YPO_4 (1:1) plus 10, 20 ou 50 mole % de ThSiO_4 . Les produits sont analysés au MET et en DRX. Quelque soit la température et pour une composition initiale de 10 ou 20 mole % de ThSiO_4 , le Th est presque entièrement réparti dans la monazite. Entre 600 et 900°C et pour une composition initiale de 50 mole % de ThSiO_4 , la cristallisation de la thorite montre une saturation en Th de la monazite. A 1000°C, seuls la monazite et un peu de xénotime sont observés; la thorite est absente.

(2) Le recuit des dégats d'irradiation dans une monazite naturelle, homogène chimiquement et concordante à 474 ± 1 Ma, a été étudié expérimentalement (500-1200°C/~7 jours). Les produits ont été analysés en DXR, MET, Raman et cathodoluminescence. La monazite non-chauffée révèle une structure en "mosaïque" composée de 2 domaines, qui sont 2 cristaux de monazites de paramètres de maille différents. Les domaines (A) correspondent aux domaines parfaitement cristallisés, où l'hélium emprisonné provoque une expansion du réseau. Les domaines (B) correspondraient à des domaines exempts d'hélium, où le réseau a été détérioré par les noyaux de recul-alpha. Lors du recuit de la monazite l'hélium diffuse hors du cristal, ce qui induit une relaxation du réseau dans les domaines (A). En même temps, les domaines (B), défectueux, sont recuits. A 900°C, le réseau de la monazite est entièrement recuit.

(3) Afin d'étudier l'effet de fluides et de la température sur le "resetting" des systèmes U-Pb dans la monazite, des fragments abrasés (200-400 μm) de l'échantillon utilisé en (2) ont été chauffés (800-1000°C/14-39 jours) en présence de solutions de diverses compositions (eau pure jusqu'à 1200°C/5 jours, fluides à NaCl , SrCl_2 , CaCl_2 et standard de Pb) puis analysés au MEB, EMP, SIMS et ID-TIMS. Quelle que soient les expériences aucun profil de diffusion du Pb n'est observé (EMP). En présence de fluide à CaCl_2 ou à standard de Pb et uniquement pour les expériences réalisées à 1000°C on observe des surcroissances. A 1000°C et dans un fluide à CaCl_2 on observe une zonation, coeur hérité et bordure enrichie en Ca et exempt de Pb, formée par dissolution/précipitation. Des discordances significatives sont observées uniquement pour les expériences réalisées à 1000°C dans les fluides à SrCl_2 (16%) ou CaCl_2 (68%). Enfin, l'utilisation du fluide à standard de Pb induit un vieillissement des monazites initiales, ce qui indique une contamination de la monazite par ce fluide.

Introduction

“Le savant n’est pas l’homme qui fournit les vraies réponses; c’est celui qui pose les vraies questions.”

Claude Lévi-Strauss - *Le Cru et le cuit*

INTRODUCTION

Rare earth elements (REE), Y, Th and U are very powerful tools for modelling petrogenetic processes in granites. Accessory minerals, like zircon, monazite, apatite, allanite, xenotime, Th-orthosilicates (thorite and huttonite), control the behaviour from these elements. For example, depletion of LREE in granite can be attributed to crystallisation of the LREE-orthophosphate monazite. In particular, the REE-orthophosphates monazite and xenotime are in the centre of our interest. Monazite occurs in many pelitic schists and gneisses of upper amphibolite and granulite metamorphic grade and pelitic compositions, and in metaluminous to peraluminous granitoid rocks (Overstreet, 1967; Parrish, 1990; Nabelek et al., 1995; Franz et al., 1996). This LREE-phosphate contains also high U and Th content (1.5 wt.% UO₂ and 14 wt.% ThO₂). Surprisingly, minor importance has been given to the HREE-Y-orthophosphate xenotime, which also may incorporate relatively high amounts of U (2 wt.% UO₂) and, to a somewhat minor extent, also Th (< 1 wt.% ThO₂) (values from metapelite after Franz et al., 1996). Xenotime also occurs in granitoids and metamorphic rocks too and was found together with monazite for a large range of metamorphic and magmatic conditions. The compositions of these coexisting minerals depend on bulk composition and on the partitioning coefficients between them. These coefficients are pressure and temperature dependent and therefore appropriate for use as geothermobarometer (Franz et al., 1996; Gratz and Heinrich, 1997; Heinrich et al., 1997; Andrehs and Heinrich, 1998).

The LREE Sm-Nd, U-Pb, and Th-Pb are very powerful geochronometers. Monazite is widely used in U-Th-Pb geochronology to determine the timing of magmatic and metamorphic events (Parrish, 1990). This is because monazite contains very high U and Pb contents and commonly occurs in peraluminous rocks, where zircon often is full of inherited cores and thus not useful for U-Pb dating. Mostly, ²⁰⁶Pb/²³⁸U and ²⁰⁷Pb/²³⁵U ages in monazites are concordant. However, discordant U-Pb ages have also been reported (Cocherie et al., 1998; Paquette et al., 1999). Any correct interpretation of measured isotope ratios requires a detailed understanding of the resetting process that may affect the isotope system of monazite. Two processes are commonly considered to explain the resetting of an isotopic system: (1) loss of Pb by volume diffusion out of the monazite grain, or (2) dissolution via a coexisting fluid and precipitation of a newly formed Pb-free monazite. For the U-Th-Pb systems, the radioactive decay produces radiation damages that may partially or totally destroy the crystal lattice, thus producing a so-called metamict crystal. Whatever the mechanism of resetting is

considered to be, it can be anticipated that the kinetics of resetting will strongly be influenced by the degree of metamictization of the crystal. A good knowledge of the structure of the studied monazite and its behaviour under irradiation and heating is strongly required. No detailed model for dissolution/precipitation resetting is available, but we can predict that the kinetics of dissolution, the solubility of the crystal, and the nature of the fluid phase should be important parameters.

This experimental work is divided in three parts, each of them consisting of one article. These publications were submitted in different international journals and are written together with other scientists. The first chapter is focused on the Th partitioning between monazite and xenotime. The second part reports investigations on the monazite structure using X-Ray diffraction (XRD), transmission electron microscopy (TEM) and Raman spectroscopy, and on the annealing of radiation damages of a natural monazite. Finally, in the last chapter, an experimental study of the resetting of the U-Pb geochronological system of natural monazite is developed. In the following an introduction of each part is given.

I- Th partitioning between monazite and xenotime

Monazite is monoclinic, with space group $P2_1/n$, and isostructural with huttonite (ThSiO_4). Xenotime is tetragonal, with space group $I4_1/amd$, and isostructural with thorite, which is the dimorph of huttonite. Both atomic arrangements are based on [001] chains of alternative edge-sharing phosphate tetrahedra and REE polyhedra, with a REEO_8 polyhedron in xenotime and a REEO_9 polyhedron in monazite (figure 1). Monazite preferentially incorporates the larger light REE, i.e. elements with ionic radii between La (1.216 Å) and Gd (1.107 Å), whereas xenotime incorporates Y (1.019 Å) and the smaller, heavy REE, i.e. elements between Tb (1.040 Å) and Lu (0.977 Å) (figure 2). Th may be incorporated as two components in monazite and xenotime: the brabantite $[\text{REE}_2\text{Ca}_1\text{Th}_1]$ and the Th-silicate $[\text{P}_1\text{REE}_1\text{Si}_1\text{Th}_1]$ component (Franz et al., 1996; Van Emden et al., 1997; Förster 1998).

In this study, only incorporation of Th as ThSiO_4 was investigated. ThSiO_4 naturally occurs as the 2 dimorphs thorite and huttonite. In our experiments pressure was set at 2 Kbar and temperatures were in the range of 600 to 1100°C. For these conditions thorite is stable (Seydoux and Montel, 1997). A simple ternary system $\text{CePO}_4\text{-YPO}_4\text{-ThSiO}_4$ was chosen as a model system. CePO_4 and YPO_4 are, respectively, suitable representatives of monazite and

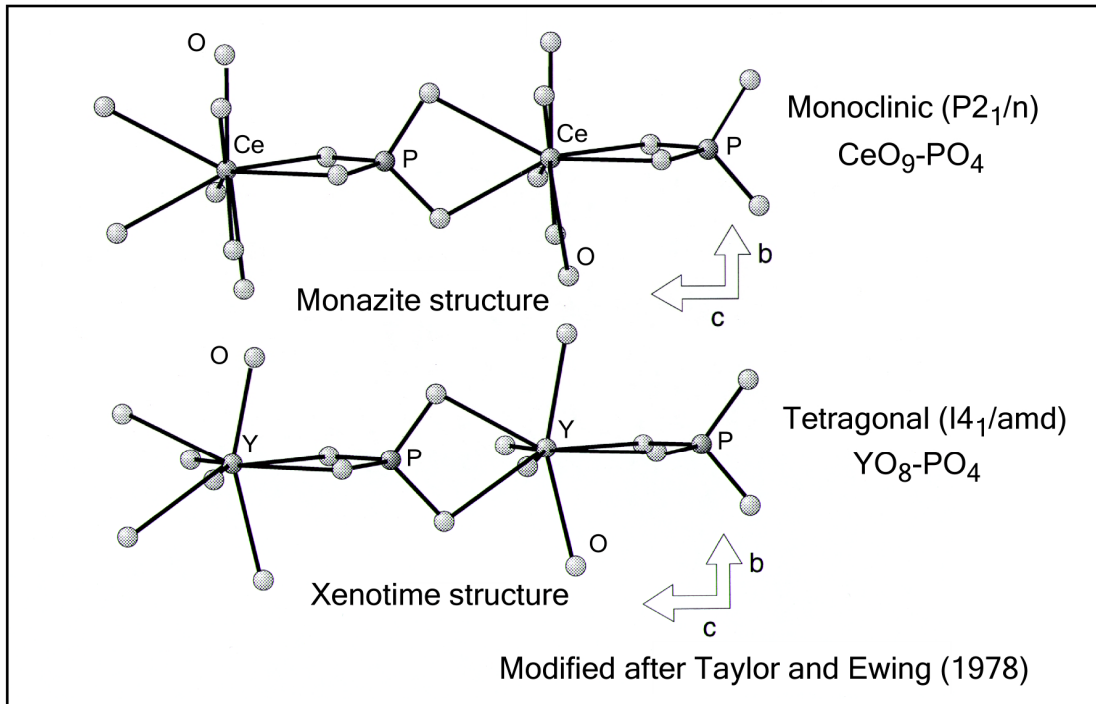


Figure 1: Comparison between monazite $CePO_4$ and xenotime YPO_4 structures. Both arrangements are based on [001] chains of intervening phosphate tetrahedra and REE polyhedra with a $REEO_8$ polyhedron in xenotime and a $REEO_9$ polyhedron in monazite. The transition between the two consists in a distortion around [010] (Ni et al. 1995).

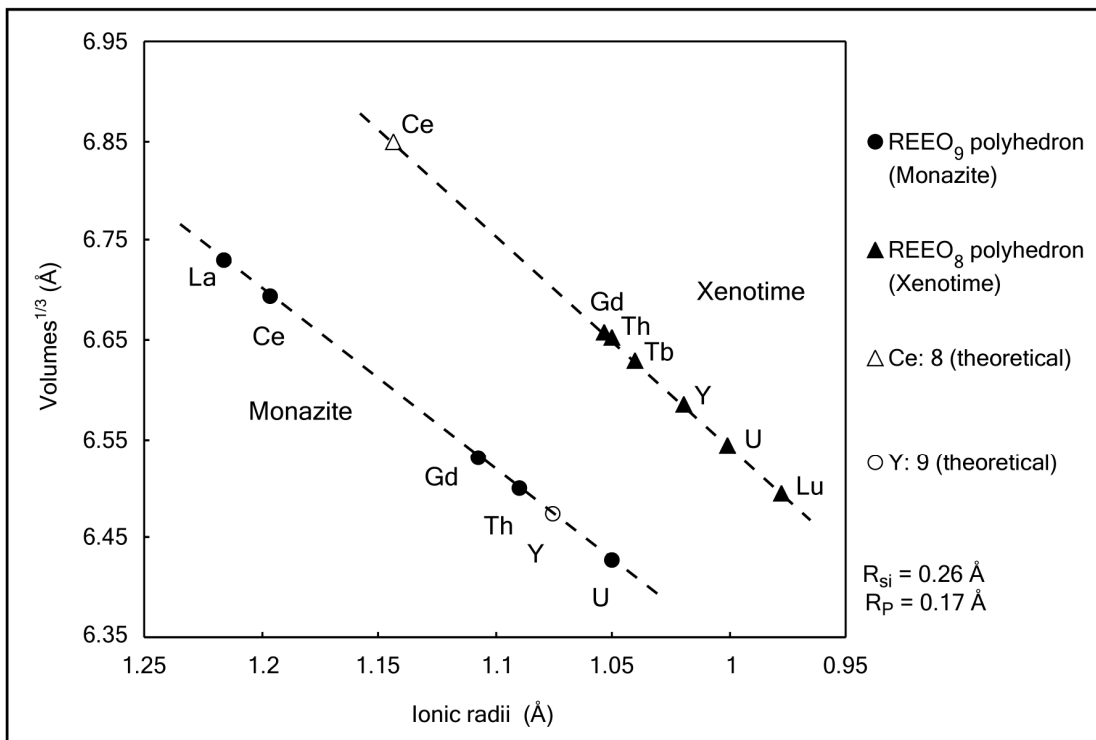


Figure 2: Unit-cell volumes of pure $REEPO_4$ vs. ionic radii modified after Ni et al. (1995). Open symbols correspond to theoretical values calculated by linear regression. The values of ionic radii (Shannon, 1976) are the effective radii in 9- and 8-fold coordination in monazite (black dots) and xenotime (black squares) structure, respectively.

xenotime of natural compositions. From the three binaries that compose this system, only the $\text{CePO}_4\text{-YPO}_4$ binary is well-constrained (Gratz and Heinrich, 1997). From experimental works of Podor and Cuney (1995; 1997) it is known that total miscibility exists along the two binaries $\text{LaPO}_4\text{-Ca}_{0.5}\text{Th}_{0.5}\text{PO}_4$ and $\text{LaPO}_4\text{-Ca}_{0.5}\text{U}_{0.5}\text{PO}_4$ at 2 kbar and 780°C. However, nothing is known about the $\text{CePO}_4\text{-ThSiO}_4$ or $\text{YPO}_4\text{-ThSiO}_4$ binaries. In this first part the ThSiO_4 partitioning between monazite and xenotime is investigated in order to test the effect of ThSiO_4 on the monazite-xenotime geothermobarometer.

II- Structure of a natural monazite: behaviour under heating

Monazite contains considerable amounts of ^{232}Th , ^{238}U and ^{235}U . Their radioactive decay produces 6, 8, and 7 α -particles, respectively, resulting in ^{208}Pb , ^{206}Pb and ^{207}Pb . During an α -event a heavy atom nucleus liberates its energy by ejecting an α -particle (^4He -nuclei), which carries 98% of the initial energy. The α -particle, which has an energy between 3.9 to 8.4 MeV, is ejected to about 10-40 μm from the point of disintegration. It dissipates most of its energy by ionisation and produces isolated defects (~ 100 atomic displacements). In contrast, the remaining nucleus is recoiled in the opposite direction to about 10-20 nm from the α -particle, according to the principle of momentum conservation, and causes collision cascades ($\sim 700\text{-}1000$ atomic displacements). Most of the atomic displacements leading to amorphization of a crystal lattice are caused by alpha-recoil nuclei (Ewing et al. 1995; 2000; Weber et al. 1998) (figure 3).

In contrast to zircon (Speer 1982), metamict monazite is rarely found in nature (Ewing 1975). Even old, radioactive monazites are mostly crystalline, despite the intensive radiation doses they received. However, there is some evidence of radiation damage in natural monazite grains, which are limited to isolated domains within the crystal (Black et al. 1984; Meldrum et al. 1998). This suggests that, even at low temperature, the monazite lattice is healed easily (Boatner and Sales 1988). Radiation damages in minerals can be induced by using external heavy-ion irradiation. For most crystals it is possible to define an amorphization dose above which the crystal is totally metamict (amorphous state). The amorphization dose increases with increasing temperature and reaches a critical temperature above which amorphization can no longer be achieved, because the crystal lattice is faster thermally reconstructed than it is destroyed. It has been shown that monazite is not more resistant to irradiation than zircon,

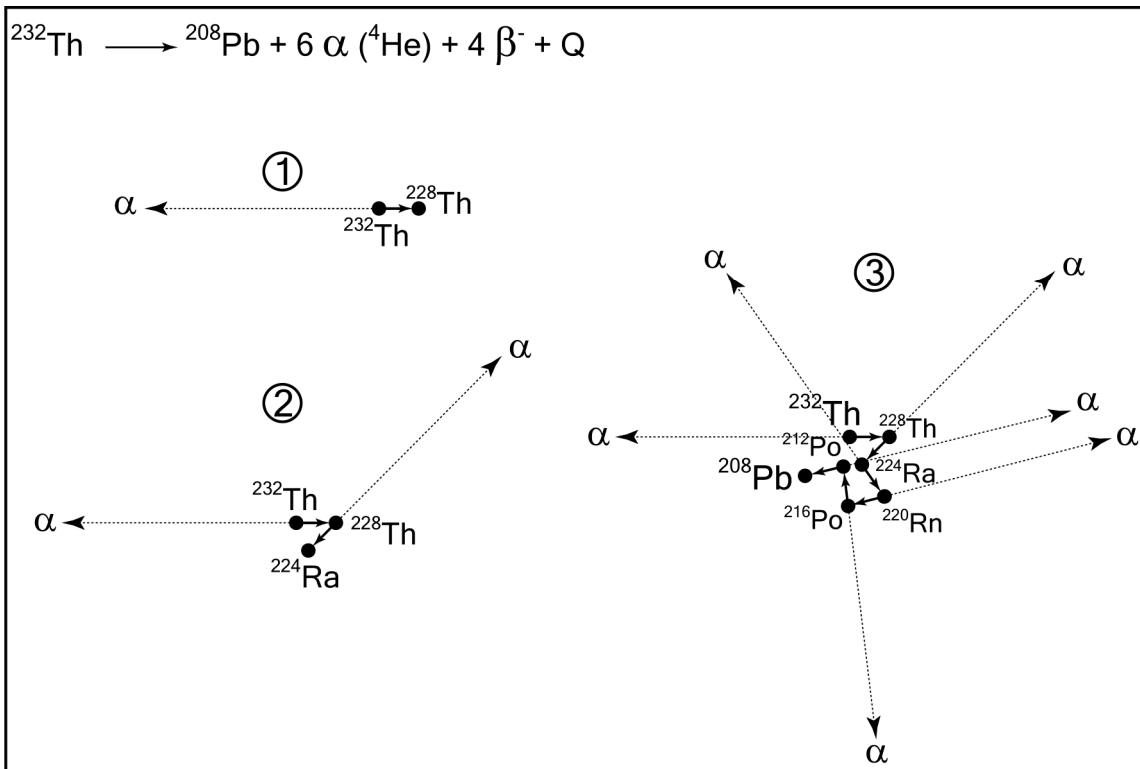


Figure 3: Formation of α -particles and α -recoil nuclei during α -decay event (example of the decay of Th). Note that the α and α -recoil nuclei are ejected in an opposite direction and that the α -particle is ejected at a greater distance than the α -recoil nucleus (~ 1000 times as long). 1, 2 and 3 correspond to different steps of the decay and step 3 is the last one, at which Pb is produced.

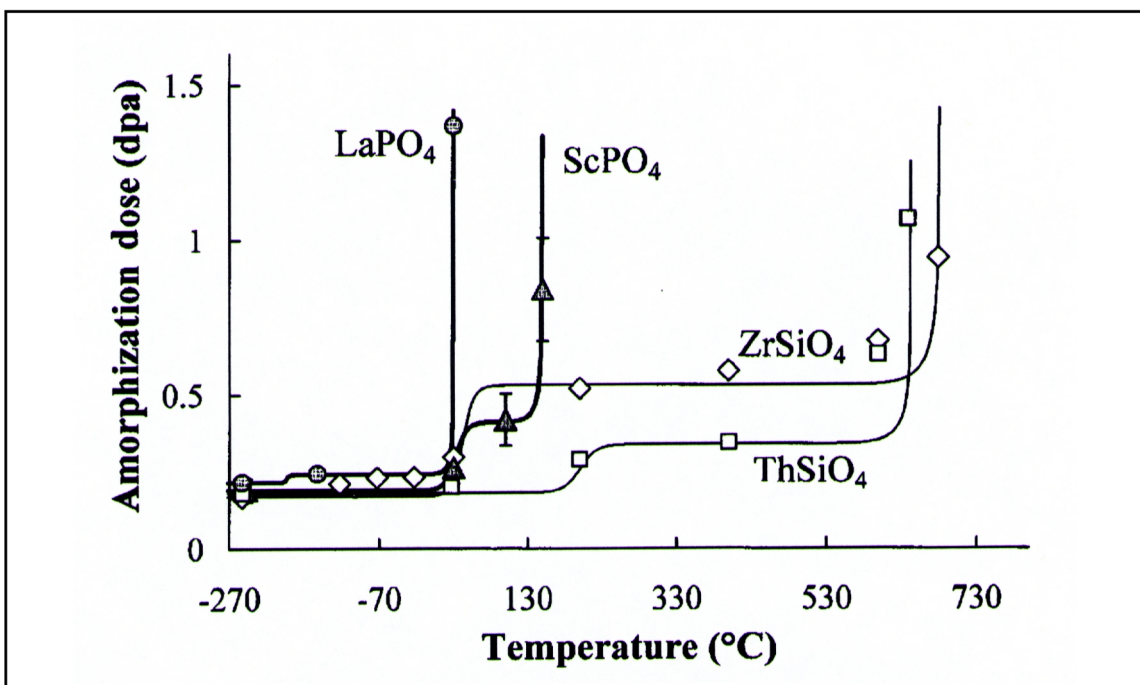


Figure 4: Amorphization dose as a function of temperature for LaPO_4 , ScPO_4 , ZrSiO_4 and monoclinic ThSiO_4 . After Meldrum et al. (2000)

because at room temperature amorphization dose is similar for the two minerals. The main difference is based on the critical temperature, which for monazite is in the range 100-200°C, but for zircon is above 700°C (figure 4). Therefore monazite is able to restore its structure at low temperature, although it is not specifically resistant to radiation damage.

Previous works on the annealing of monazite provided different results. Karioris et al. (1981) in a XRD study, and Meldrum et al. (1998) in a TEM study, both using an ion-beam-amorphised monazite, observed recrystallization at 300 and 450°C respectively. In contrast, in a XRD study Smith and Giletti (1997) completely healed a natural crystalline monazite between 800°C and 1100°C. In this study, the healing of radiation damages in a natural crystalline monazite has been experimentally investigated using XRD, TEM, Raman microprobe and Cathodoluminescence analyses. The starting material was a chemically homogeneous monazite from a Brazilian pegmatite with a concordant age of 474 ± 1 Ma showing nm-scale defects induced by radioactive decay.

III- Resetting of U-Pb isotopic geochronological system

U-Pb concordance means that, during geological events, the monazite U-Pb system is either completely reset, i.e. monazite has lost all its radiogenic Pb, or remains totally unaffected. Discordant U-Pb ages means that monazite has lost some radiogenic Pb since its crystallization or since the last event, that completely reset it. These discordances may result from U-Pb analyses which are performed on monazite fractions of mixed grain populations crystallised at different times within a particular rock. One case of discordance attributed to diffusive Pb loss has been reported by Suzuki et al. (1994). Mostly, discordances result from mixtures of newly grown rims with inherited cores (figure 5). However, the controlling mechanisms that induce resetting during a geological event, i.e. loss of Pb by volume diffusion or dissolution via a coexisting fluid and precipitation of a newly formed lead-free monazite, are only poorly understood.

With respect to resetting by diffusive Pb-loss, there are several attempts to interpret discordant ages of natural monazite grains in terms of the closure temperature's concept (Dodson, 1973). This model is defined for a geochronological or a geochemical system. It assumes that volume diffusion controls the loss of the daughter nuclide (here Pb) and at the closure temperature the daughter nuclide begins to accumulate in the crystal. The closure temperature will also depend on the size of the crystal, its shape, the cooling rate during the

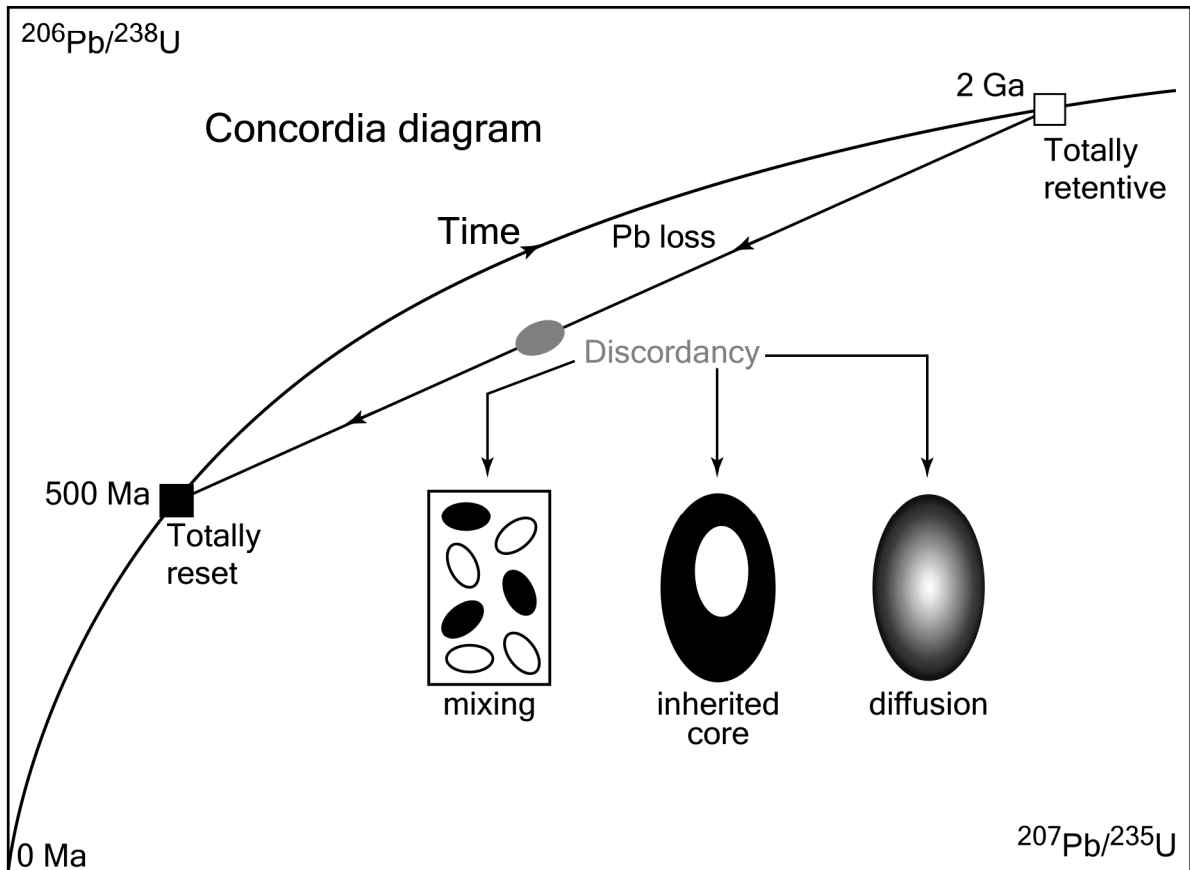


Figure 5: Schematic drawing showing concordancy and discordancy in the U-Pb concordia diagram and the different causes for discordancies, i.e. mixing of different population of grains, presence of inherited cores or presence of diffusion profile.

geological event, and the diffusion coefficient of the daughter elements. However, two important facts limit the use of this concept. First, it ignores quantification of the main driving force for any diffusion process, i.e. the chemical potential gradient of the Pb-bearing component between monazite and the adjacent phase. Second, it implies a resetting by diffusion, which is not very realistic, considering results from experiments on Pb-self-diffusion in monazite by Smith and Giletti (1997), which showed that diffusion is very slow, even at high temperatures. Furthermore, it has been shown by De Wolf et al. (1993), Kalt et al. (2000), Montel et al. (2000) that monazite inclusions, which are shielded by host minerals such as quartz and garnet, were not subject to resetting, despite the fact that they were exposed to granulite-facies temperatures of more than 800°C over long time scales.

Dissolution/precipitation in the presence of a fluid phase is another possible mechanism for resetting of the monazite isotope system. If so, one would expect that the fluid composition had a major effect on the process. Previously, Teufel and Heinrich (1997) showed that significant dissolution and precipitation along with Pb-loss into pure water was only observed for very fine powdered monazite as starting material. Hydrothermal treatment of natural monazite grains larger than 40 µm at 750°C/3 kbar and in pure water did not affect their U-Pb system.

In the third part, we propose to evaluate which of the two mechanisms - dissolution/precipitation or volume diffusion- controls the resetting of the U-Th-Pb isotope system in monazite, and to see the influence of fluid composition and temperature on the extent of this process.

CHAPTER I

Th partitioning between monazite and xenotime

“Laboratoire. Même quand on ne trouve rien, on renifle l’odeur de la vérité qui se cache.”

Jean Rostand - *Carnet d’un biologiste*

An experimental determination of the Th partitioning between monazite and xenotime using Analytical Electron Microscopy (AEM)

Abstract:

The Thorium distribution between monazite and xenotime has been determined experimentally using the coupled substitution $\text{Th} + \text{Si} \leftrightarrow \text{REE} + \text{P}$. Experiments have been conducted in standard cold seal hydrothermal and internally heated pressure vessels at 200 MPa in the range of 600-1100°C. Starting mixtures were prepared from gels composed of equal amounts of CePO_4 and YPO_4 with addition of 10, 20 and 50 mol% ThSiO_4 . The grain sizes of the run products were in the range of a few microns. Analytical electron microscopy (AEM) methods were applied to obtain reliable chemical compositions of the reaction products. Lattice parameters of run products were determined using Rietveld analysis. For runs with 10 and 20 mol% ThSiO_4 component in the bulk the ThSiO_4 component distributes almost exclusively into monazite at all temperatures. The amount of the YPO_4 component in monazite increases relative to the Th-free system if significant amounts of ThSiO_4 are present within the structure. ThSiO_4 favours incorporation of YPO_4 resulting in a shift of the monazite limb and the shrinkage of the monazite-xenotime miscibility gap. Thermobarometric calculations based on monazite-xenotime equilibria must be corrected for this effect. For runs with 50 mol% ThSiO_4 in the bulk, thorite formed as an additional phase at 600 to 900°C but was absent at higher temperatures. At high $X_{\text{ThSiO}_4}^{\text{bulk}}$ and low T, the system is three-phase. The three-phase stability field strongly shrinks with increasing temperature. A tentative phase diagram of the ternary system CePO_4 - YPO_4 - ThSiO_4 is proposed and discussed in the light of monazite-xenotime-thorite-bearing assemblages in natural rocks.

Key words Monazite • Xenotime • Thorium • XRD • AEM

1 – Introduction

The REE-orthophosphate minerals monazite and xenotime occur together in many metamorphic (Franz *et al.*, 1996; Heinrich *et al.*, 1997; Andrehs & Heinrich, 1998; Harlov & Förster, 2001) and magmatic rocks (Bea, 1996; Förster, 1998a,b; Viskupic & Hodges, 2001). Monazite is commonly used for U-Th-Pb age determination because of its high U and Th contents (Parrish, 1990). Minor emphasis has been given to xenotime, which also incorporates relatively high amounts of U and, to a somewhat minor extent, also Th. Monazite preferentially incorporates the light rare earth elements (LREE), and xenotime the heavy rare earth elements (HREE) and Y (Franz *et al.*, 1996; Heinrich *et al.*, 1997). Monazite is monoclinic, with the space group $P2_1/n$, and isostructural to huttonite, the high P – high T modification of ThSiO_4 . Xenotime is tetragonal, with the space group $I4_1/amd$, and isostructural to thorite, which is the low P – low T polymorph of ThSiO_4 (Pabst & Hutton, 1951; Berzelius, 1829). Both atomic arrangements are based on chains along [001] of intervening phosphate tetrahedra and REE polyhedra, where the REE ions are 8-fold coordinated in xenotime and 9-fold in monazite (Ni *et al.*, 1995). It is known from natural assemblages (Franz *et al.*, 1996; Van Emden *et al.*, 1997; Förster, 1998a,b) that Th and U are incorporated by two exchange mechanisms in monazite and xenotime: the brabantite exchange $[\text{REE}_2\text{Ca}_1(\text{U}, \text{Th})_1]$ and the huttonite/thorite exchange $[\text{P}_1\text{REE}_1\text{Si}_1(\text{U}, \text{Th})_1]$. In natural rocks, coexisting monazite-xenotime pairs suggest that Th is preferentially incorporated into monazite as brabantite and U into xenotime as thorite component, however, quantitative relationships are unknown.

Complete U-Th-Pb dating of monazite single crystals have shown that U-Pb and Th-Pb age determinations can result in different ages (Barth *et al.*, 1994; Parrish & Carr, 1994). Different processes might explain this behaviour. One possibility is that crystals are compositionally zoned. Zonation may be induced during slow metamorphic growth over several Ma. Within a single crystal, different domains can be dated assuming a sufficient precision of the spatial resolution and the resolution of the time scale of the age determination method (Harrison *et al.*, 1995; Montel *et al.*, 1996; Cocherie *et al.*, 1998; Crowley & Ghent, 1999; Grove & Harrison, 1999; Paquette *et al.*, 1999; Poitrasson *et al.*, 2000). Using such radiometric age determinations together with geothermometry, growth temperatures can be directly correlated with time (Viskupic & Hodges, 2001).

Prograde zoning of metamorphic monazite seems to be very common (Heinrich *et al.*, 1997) and it has been shown that the partitioning of each REE between monazite and xenotime is a function of temperature and pressure. This allows the use of the REE partitioning between monazite and xenotime as a geothermobarometer (Gratz & Heinrich, 1997; Heinrich *et al.*, 1997; Andrehs & Heinrich, 1998; Gratz & Heinrich, 1998). It would therefore appear that the U-Th partitioning between coexisting monazite and xenotime were also temperature and pressure dependent and that crystals might be zoned in respect to their U/Th ratios.

The present study reports the experimental determination of the Th distribution between monazite and xenotime and provides information on how the presence of Th in the system affects the CePO_4 - YPO_4 geothermobarometer. Here, only the incorporation of Th as ThSiO_4 component into both phases will be considered. The ternary system CePO_4 - YPO_4 - ThSiO_4 was chosen as a model system. From the three binaries that define the ternary system, only the CePO_4 - YPO_4 binary is experimentally well-constrained (Gratz & Heinrich, 1997). In a closely related system complete miscibility exists along the two binaries LaPO_4 - $\text{Ca}_{0.5}\text{Th}_{0.5}\text{PO}_4$ and LaPO_4 - $\text{Ca}_{0.5}\text{U}_{0.5}\text{PO}_4$ at 200 MPa and 780°C (Podor & Cuney, 1995; 1997). However, there is no information about the CePO_4 - ThSiO_4 and YPO_4 - ThSiO_4 binaries and we only know that at 200 MPa and 600 to 1100°C thorite is probably the stable ThSiO_4 polymorph (Seydoux & Montel, 1997).

Synthesis of REE-phosphates in presence of the ThSiO_4 component produces extremely fine grained crystals. Analytical electron microscopy (AEM) and X-ray diffraction (XRD) were therefore applied. We will show that at low ThSiO_4 concentrations in the bulk it is mainly partitioned into monazite and that it shifts the position of the monazite limb within the miscibility gap of the CePO_4 - YPO_4 binary. This allows interpreting discrepancies in temperature estimations that use the monazite-xenotime thermobarometer. We further show that for high ThSiO_4 concentrations in the bulk and low temperatures, thorite is stable and tentatively present phase relations within the CePO_4 - YPO_4 - ThSiO_4 ternary at different temperatures.

2 - Experimental and analytical techniques

2-1 - Starting materials

For all experiments gels were used as starting materials. This allowed the preparation of stoichiometric mixtures of the starting materials and always resulted in homogeneous crystals. The disadvantage of the gel method is that the run products were very small ($\leq 2\mu\text{m}$) and that at temperatures below 800°C the products were poorly crystallized. This is particularly true at high amounts of ThSiO_4 in the bulk. At these conditions, the products could not be analyzed adequately by AEM and XRD, respectively.

Pure $\text{ThN}_4\text{O}_{12}$, 5 H_2O (Merck); YN_3O_9 , 6 H_2O (Riedel de Haën) and CeN_3O_9 , 6 H_2O (Merck, ultrapure) were dissolved in water. Tetra-ethyl-ortho-silicate (TEOS) together with the same amount of ethanol, and $\text{HPO}_4\text{N}_2\text{O}_8$, dissolved in water, were added. Nitrates and water were removed from the precipitate by drying and firing resulting in a gel, which consisted of CePO_4 , ThSiO_4 , and YPO_4 . Three different gel bulk compositions were prepared and consisted of equal amounts of CePO_4 and YPO_4 with additional 10, 20 and 50 mol% of ThSiO_4 . About 50 mg of gel together with SiO_2 in excess were filled in Pt capsules (20 mm long, 3 mm in diameter) and welded. The capsules were checked for leaks by heating them at 110°C for 24 hours.

Oxide mixtures with excess H_3PO_4 as used by Gratz & Heinrich (1997; 1998) resulted in somewhat larger crystals. However, excess of H_3PO_4 resulted in formation of thorium phosphate with an unknown structure. On the other hand, it is impossible adding a stoichiometric amount of solid H_3PO_4 during loading of the capsules because it is extremely hygroscopic. Therefore, experiments that used oxide mixtures were discarded.

2-2 - Experimental procedure

Experiments at 100 and 200 MPa up to 900°C (Table 1) were carried out in standard cold seal hydrothermal vessels with water as pressure medium. The temperature was recorded using Ni-CrNi thermocouples inside the vessel close to the sample. The total temperature uncertainties are estimated at about $\pm 3^\circ\text{C}$. Pressure was measured using a transducer calibrated against a Heise gauge manometer. The indicated pressure is accurate within ± 50 bars. Run durations were between 240 and 816 hours. The capsules were quenched with compressed air to room temperature within 3 minutes.

Table 1 - Experimental conditions and bulk compositions.

Run No.	P (MPa)	T (°C)	Duration (Hours)	Bulk composition (molar fraction)		
				CePO ₄	ThSiO ₄	YPO ₄
MXTh99-31	200	800	456	0,45	0,10	0,45
MXTh99-35	100	900	240	0,45	0,10	0,45
MXTh99-38	100	900	240	0,40	0,20	0,40
MXTh99-44	200	800	408	0,25	0,50	0,25
MXTh99-45	200	600	816	0,25	0,50	0,25
MXTh99-47	100	900	312	0,25	0,50	0,25
MXTh99-54	200	1000	236	0,45	0,10	0,45
MXTh99-55	200	1000	236	0,40	0,20	0,40
MXTh99-56	200	1000	236	0,25	0,50	0,25
MXTh0-5	200	1100	548	0,45	0,10	0,45
MXTh0-6	200	1100	548	0,40	0,20	0,40
MXTh0-7	200	1100	548	0,25	0,50	0,25

All bulk products consist of gel + SiO₂ in excess
Runs at 1000 and 1100°C were performed in IHPV

Experiments at 200 MPa for 1000 and 1100°C were performed in internally heated pressure vessels (IHPV) with Ar as pressure medium (Table 1). The temperatures were recorded using three Pt₈₇Rh₁₃-Pt thermocouples. The total temperature uncertainties are estimated to be about ± 10°C. Run durations were 236 hours at 1000°C and 548 hours at 1100°C. The capsules were quenched to room temperature within a few minutes. After quenching the capsules were checked for leaks. The run products were investigated by optical microscopy, scanning electron microscopy, analytical electron microscopy and X-ray powder diffraction.

2-3 - Analytical electron microscopy (AEM)

Because of the small size of the products, EMP analyses were not performed. The chemical composition of coexisting phases was therefore determined by AEM. AEM investigations were carried out with a Philips CM200 electron microscope. The electron microscope is equipped with an EDAX X-ray analyzer with ultrathin window. The acceleration voltage was 200kV, and the electron source was a LaB₆ filament. Analyses were carried out in transmission mode with a spot size of 40 nm and a beam current of 0.2 nA. The specimen was tilted 20° towards the detector and acquisition time was 200 seconds. The spectra were corrected for absorption and fluorescence applying the EDAX software package for thin films. The foil thickness, necessary for absorption correction was determined by electron energy-loss spectroscopy (EELS) using the total intensity of the electrons reaching the EEL spectrometer and the intensity of the zero loss peak (Egerton, 1996). EDX analyses were quantified by applying the ratio technique of Cliff & Lorimer (1975) for thin foils. The factors k_{Ce_L/Si_K} , k_{Y_K/Si_K} , k_{Th_L/Si_K} and k_{P_K/Si_K} were determined using synthetic CePO₄, YPO₄, (Ce,Y)PO₄ solid solutions (Gratz & Heinrich, 1997), and natural monazite. The chemical compositions of the standards were determined by electron microprobe analysis (Table 2 and 3). The TEM foil was prepared from the same section of the standard, which has been measured by EMP. The precision of the analyses depends on the counting statistic, the errors of k -value determination and the error measurement of the different intensities of the elements (Joy *et al.*, 1989). The relative statistical error of the analysis is calculated by applying the equation: $rel.error = \frac{t_{99}^{n-1} * s}{\sqrt{n} * \bar{x}} * 100\%$ (t_{99}^{n-1} = Student t value, s = standard deviation, n = number of measurements, \bar{x} = mean value). The total statistical relative error for the different oxides is given in Table 4.

Table 2 - AEM analyses of synthetic monazites of the $\text{CePO}_4\text{-YPO}_4$ binary from Gratz and Heinrich (1997) compared with compositions obtained from lattice parameters (see their Table 1)

Run No.	P7	P14	P13
Number of analyses	14	11	10
Wt%			
P_2O_5	31.49	30.34	30.50
Ce_2O_3	64.44	63.63	61.61
Y_2O_3	4.09	6.05	7.90
Σ	100.02	100.02	100.01
Cations			
P	1.02	0.98	0.98
Ce	0.90	0.90	0.86
Y	0.08	0.12	0.16
Σ	2.00	2.00	2.00
X_Y (AEM)	0.08 (2)	0.12(4)	0.16(3)
X_Y (XRD)	0.07 (1)	0.10 (1)	0.15 (1)

X_Y : Y concentration (mole fraction) in monazite

Table 3 - Comparison between EMP and AEM analyses from a natural ThSiO_4 -bearing monazite from Brazil (Seydoux-Guillaume et al., submitted)

Wt %	EMP	AEM**
SiO_2	1.47 (15)	2.55 (54)
P_2O_5	28.64 (29)	29.79 (96)
CaO	0.45 (9)	0.90 (24)
La_2O_3	14.95 (15)	14.01 (39)
Ce_2O_3	31.50 (32)	29.91 (68)
Pr_2O_3	3.24 (32)	3.15 (25)
Nd_2O_3	10.51 (11)	10.45 (48)
Sm_2O_3	2.11 (21)	1.83 (48)
ThO_2	7.13 (71)	7.42 (60)
Σ^*	100	99,99

Σ^* has been set to 100%

** average of 11 analyses

Errors in brackets (2σ)

Table 4 - Relative amounts of phases in the run products and their lattice parameters

Run No.	T (°C)	X _{ThSiO₄} Bulk	Rel. amounts of products (weight fraction)				Lattice parameters of monoclinic monazite					Lattice parameters of tetragonal phases					
			Mz	Xe	Qz	Th	<i>a</i> (Å)	<i>b</i> (Å)	<i>c</i> (Å)	<i>β</i> (°)	<i>V</i> (Å ³)	Xenotime			Thorite		
												<i>a = b</i> (Å)	<i>c</i> (Å)	<i>V</i> (Å ³)	<i>a = b</i> (Å)	<i>c</i> (Å)	<i>V</i> (Å ³)
MXTh99-31	800	0.10	0.64	0.26	0.10		6.768(1)	6.991(1)	6.461(1)	103.52(1)	297.26(9)	6.891(1)	6.029(1)	286.29(9)			
MXTh99-35	900	0.10	0.69	0.22	0.10		6.763(1)	6.984(1)	6.458(1)	103.55(1)	296.56(5)	6.889(1)	6.028(1)	286.07(9)			
MXTh99-54	1000	0.10	0.72	0.21	0.07		6.753(1)	6.975(1)	6.452(1)	103.57(1)	295.50(5)	6.890(1)	6.027(1)	286.14(5)			
MXTh0-5	1100	0.10	0.75	0.18	0.07		6.738(1)	6.960(1)	6.439(1)	103.60(1)	293.55(4)	6.888(1)	6.024(1)	285.79(8)			
MXTh99-38	900	0.20	0.74	0.14	0.12		6.753(1)	6.970(1)	6.457(1)	103.65(1)	295.38(5)	6.894(1)	6.035(1)	286.85(9)			
MXTh99-55	1000	0.20	0.77	0.13	0.10		6.745(1)	6.964(1)	6.454(1)	103.66(1)	294.62(5)	6.897(1)	6.036(2)	287.13(16)			
MXTh0-6	1100	0.20	0.81	0.10	0.09		6.733(1)	6.950(1)	6.442(1)	103.69(1)	292.89(4)	6.892(2)	6.033(2)	286.63(12)			
MXTh99-45	600	0.50	0.39	0.03	0.02	0.56	6.776(4)	6.985(4)	6.475(3)	103.90(5)	297.52(28)	6.925(12)	6.058(17)	290.50(96)	7.093(3)	6.270(3)	315.44(28)
MXTh99-44*	800	0.50	0.51	0.01		0.47	6.767(2)	6.972(2)	6.473(2)	104.12(2)	296.21(14)	6.925(10)	6.066(14)	290.89(80)	7.078(2)	6.263(2)	313.85(16)
MXTh99-47	900	0.50	0.69	0.02		0.29	6.757(1)	6.961(1)	6.471(1)	104.26(1)	295.04(12)	6.930**	6.097**	292.81**	7.070(2)	6.253(2)	312.60 (18)
MXTh99-56	1000	0.50	0.83	0.10	0.07		6.748(1)	6.952(1)	6.468(1)	104.35(1)	294.00(4)	6.944(3)	6.090(3)	293.71(36)			
MXTh0-7	1100	0.50	0.89	0.09	0.02		6.738(1)	6.941(1)	6.458(1)	104.31(1)	292.67(4)	6.894(6)	6.086(9)	293.42(52)			
CePO ₄ synthetic (Gratz and Heinrich, 1997)							6.800	7.027	6.474	103.46	300.84						
YPO ₄ synthetic (Gratz and Heinrich, 1997)												6.883	6.021	285.28			
Huttonite (Taylor and Ewing, 1978)							6.784	6.974	6.500	104.92	297.15						
Thorite (Taylor and Ewing, 1978)												7.133	6.319	321.51			

Mz: monazite, Xe: xenotime, Th: thorite, Qz: quartz

*contains traces of thorianite ThO₂

**not refined

It is clear that compositional data acquired by AEM have distinctly larger uncertainties than those obtained by standard EMP analysis. Matrix effects are difficult to correct and it is therefore necessary to use standards that have very similar compositions to the investigated minerals. The k_{AB} -factor for a certain element varies with composition. For example, in synthetic CePO_4 the $k_{\text{Ce,P}}$ factor is 2.99, whereas in natural monazite with substantial amounts of LREE, Th, and U it is 2.01. In synthetic YPO_4 $k_{\text{Y,P}}$ is 2.72 and in synthetic $\text{Ce}_{0.98}\text{Y}_{0.02}\text{PO}_4$, it is 3.18. The major problem was to find suitable standards to determine the k_{AB} -factors used for quantification based on the thin film approximation and the ratio technique described by Cliff & Lorimer (1975). It is shown below that analyses of synthetic monazites with high amounts of ThSiO_4 component (> 20 mol%) are of somewhat poorer quality. We believe that this is because a monazite standard with high amounts of ThSiO_4 was not available. Another problem is that the Si_K and Y_{L_i} -lines and the Y_L and P_K -lines in the X-Ray spectra overlap. Therefore, the Y_K -line was used for quantifying instead of the Y_L -line, thus improving the results of the Y measurements. However, overlapping of the Y_{L_i} and Si_K -lines has a significant influence on the xenotime analyses, because YPO_4 is the major constituent of xenotime. Raw xenotime analyses always showed too large SiO_2 concentrations and all analyses needed to be corrected for that. Th in xenotime is incorporated by a coupled substitution $\text{Th}^{4+} + \text{Si}^{4+} \Leftrightarrow (\text{Ce,Y})^{3+} + \text{P}^{5+}$. Based on this substitution, the molar amount of Si must not exceed that of Th. Therefore, all components given in Tables 5 and 6, and Figure 1 are calculated using the normalisation on Ce+Y+Th and not the normalisation on P+Si.

2-4 - X-Ray diffraction (XRD)

All run products were investigated with a focusing STOE X-ray powder-diffractometer (Stadi P) using $\text{CuK}_{\alpha 1}$ radiation and a position-sensitive detector using resolution of 0.02° . The diffractometer was calibrated externally using the NBS SRM-640b silicon standard. The unit-cell refinements were performed using the Rietveld-refinement program of the GSAS software package (Larson & Von Dreele, 1988).

3 – Results

The relative amounts of phases in the run products are given in Table 4. At $X_{\text{ThSiO}_4}^{\text{bulk}}$ of 0.1 and 0.2, respectively, the products were exclusively composed of monazite and xenotime

Table 5 - Compositions of produced monazites obtained by AEM

Run No.	MXTh99-31	MXTh99-35	MXTh99-38	MXTh99-54	MXTh99-55	MXTh0-5	MXTh0-6
T (°C)	800	900	900	1000	1000	1100	1100
P (MPa)	200	100	100	200	200	200	200
X _{ThSiO₄} (bulk)	0,1	0,1	0,2	0,1	0,2	0,1	0,2
Number of analyses	14	16	18	14	12	15	15
Weight %							
SiO ₂	1.92 ± 0.40	1.81 ± 0.29	3.96 ± 0.44	1.86 ± 0.28	4.11 ± 0.39	2.13 ± 0.26	4.38 ± 0.48
P ₂ O ₅	28.23 ± 1.14	27.29 ± 1.04	25.81 ± 1.02	27.84 ± 0.86	25.25 ± 0.92	27.94 ± 0.83	25.95 ± 1.06
Ce ₂ O ₃	54.09 ± 5	52.29 ± 4.18	39.79 ± 3.22	48.61 ± 3.67	37.73 ± 3.12	45.77 ± 3.34	37.06 ± 3.62
ThO ₂	9.37 ± 0.97	10.44 ± 1.18	21.56 ± 1.68	10.85 ± 0.71	21.52 ± 1.52	10.38 ± 0.69	20.42 ± 1.80
Y ₂ O ₃	6.35 ± 1.16	8.16 ± 1.23	8.91 ± 1.34	10.82 ± 1.64	11.4 ± 1.63	13.77 ± 1.75	14.2 ± 2.00
Σ	99.96	99.99	100.03	99.98	100.01	99.99	102.01
Cations calculated on the basis of 4 Oxygens							
Si	0.075	0.071	0.156	0.072	0.162	0.082	0.167
P	0.932	0.912	0.863	0.916	0.844	0.908	0.840
Ce	0.772	0.755	0.575	0.692	0.546	0.643	0.519
Th	0.083	0.094	0.194	0.096	0.193	0.091	0.178
Y	0.132	0.171	0.187	0.224	0.240	0.281	0.289
Σ	1.993	2.004	1.975	2.000	1.985	2.004	1.992
P+Si	1.006	0.983	1.019	0.988	1.007	0.989	1.007
Ce+Th+Y	0.987	1.021	0.956	1.011	0.979	1.015	0.985
Mole fraction of components							
CePO ₄	0.78	0.74	0.60	0.68	0.56	0.63	0.53
ThSiO ₄	0.09	0.09	0.20	0.10	0.20	0.09	0.18
YPO ₄	0.13	0.17	0.20	0.22	0.24	0.28	0.29

Errors are the total relative error.

Table 6 - Compositions of produced xenotimes obtained by AEM

Run No.	MXTh99-31	MXTh99-35	MXTh99-38	MXTh99-54	MXTh99-55	MXTh99-56	MXTh0-5	MXTh0-6
T (°C)	800	900	900	1000	1000	1000	1100	1100
P (MPa)	200	100	100	200	200	200	200	200
X _{ThSiO₄} (bulk)	0.1	0.1	0.2	0.1	0.2	0.5	0.1	0.2
Number of analyses	7	8	8	10	8	1	2	3
Weight %								
SiO ₂	3.89 ± 0.90	4.00 ± 0.66	4.59 ± 0.76	3.76 ± 0.47	4.76 ± 0.89	7.70	3.95	4.47
P ₂ O ₅	38.57 ± 1.63	37.80 ± 1.78	36.09 ± 2.19	36.86 ± 1.64	35.16 ± 2.03	24.60	37.40	37.73
Ce ₂ O ₃	1.83 ± 1.07	1.31 ± 0.86	2.18 ± 1.82	1.94 ± 0.90	1.90 ± 1.34	2.30	1.70	2.90
ThO ₂	2.64 ± 0.48	1.71 ± 0.63	4.73 ± 1.35	1.31 ± 0.46	4.35 ± 1.07	15.40	1.05	3.97
Y ₂ O ₃	53.09 ± 7.17	55.18 ± 8.07	52.44 ± 8.69	56.11 ± 8.46	53.85 ± 8.79	50.10	55.85	50.90
Σ	100.02	100.00	100.03	99.98	100.02	100.10	99.95	99.97
Cations calculated on the basis of 4 Oxygens								
Si	0.116	0.120	0.140	0.114	0.147	0.266	0.119	0.135
P	0.975	0.958	0.935	0.946	0.916	0.720	0.952	0.962
Ce	0.020	0.014	0.024	0.022	0.021	0.029	0.019	0.032
Th	0.018	0.012	0.033	0.009	0.030	0.121	0.007	0.027
Y	0.843	0.880	0.854	0.905	0.882	0.922	0.894	0.816
Σ	1.972	1.984	1.986	1.995	1.997	2.058	1.990	1.971
P+Si	1.091	1.078	1.075	1.060	1.063	0.986	1.071	1.097
Ce+Th+Y	0.881	0.906	0.911	0.936	0.934	1.073	0.919	0.875
Mole fraction of components								
CePO ₄	0.02	0.02	0.03	0.02	0.02	0.03	0.02	0.04
ThSiO ₄	0.02	0.01	0.04	0.01	0.03	0.11	0.01	0.03
YPO ₄	0.96	0.97	0.94	0.97	0.95	0.86	0.97	0.93

Errors are the total relative error.

at all temperatures, plus some additional quartz which was added in excess to the starting mixture. Monazite is always the dominant phase. At $X_{ThSiO_4}^{bulk}$ of 0.5, thorite additionally formed in large amounts at 600°C, 800°C, and 900°C, but was absent at 1000°C and 1100°C. Where thorite is present, the amount of xenotime is very small (Table 4).

3-1 - Compositions of monazite and xenotime determined by AEM

Compositions of coexisting monazite and xenotime are presented in Tables 5 and 6 and in Figure 1. We have, unfortunately, no reliable chemical compositions of thorite, because suitable AEM standards for the $CePO_4$ and YPO_4 components in thorite were not available. At $X_{ThSiO_4}^{bulk}$ of 0.1 and 0.2, respectively, the $ThSiO_4$ component is partitioned almost exclusively in monazite at all temperatures (Figure 1). Xenotime is very poor in $CePO_4$ and $ThSiO_4$ components and has, given the relatively large analytical uncertainties, nearly the same composition at all temperatures. The compositions of monazite and xenotime synthesised from these bulk compositions are consistent with the boundaries of the miscibility gap of the $CePO_4$ - YPO_4 binary (Gratz & Heinrich, 1997). The temperature dependence of this gap is traced into the ternary (dotted lines in Figure 1). Monazite incorporates most of the $ThSiO_4$ component and the gap shrinks towards the YPO_4 apex as more YPO_4 component is incorporated with increasing temperature. Since the $ThSiO_4$ component is always taken up by monazite, $X_{ThSiO_4}^{mon}$ does not significantly vary with temperature at a given bulk composition. Therefore, $X_{ThSiO_4}^{mon}$ is ~ 0.09 at $X_{ThSiO_4}^{bulk} = 0.1$, and ~ 0.19 at $X_{ThSiO_4}^{bulk} = 0.2$ in the relevant temperature range (Figs. 1 and 2). $X_{YPO_4}^{mon}$ increases strongly with temperature, and the important point is that it increases also with increasing $X_{ThSiO_4}^{mon}$ at given temperature (Fig. 2). This implies that the monazite limb is systematically shifted towards higher YPO_4 concentrations if $ThSiO_4$ is present. It is clear that this has a significant effect on the monazite-xenotime thermobarometer (see discussion below).

At $X_{ThSiO_4}^{bulk}$ of 0.5, analytical problems did not allow for precise determination of $ThSiO_4$ in monazite and xenotime. The analytical scatter of monazite compositions produced in thorite-free experiments at 1000°C and 1100°C are represented by elliptical areas in Figure 1. With respect to their $CePO_4$ and YPO_4 concentrations, however, the compositional data agree with the broadly outlined shape of the miscibility gap in the ternary (Fig. 1). This is also

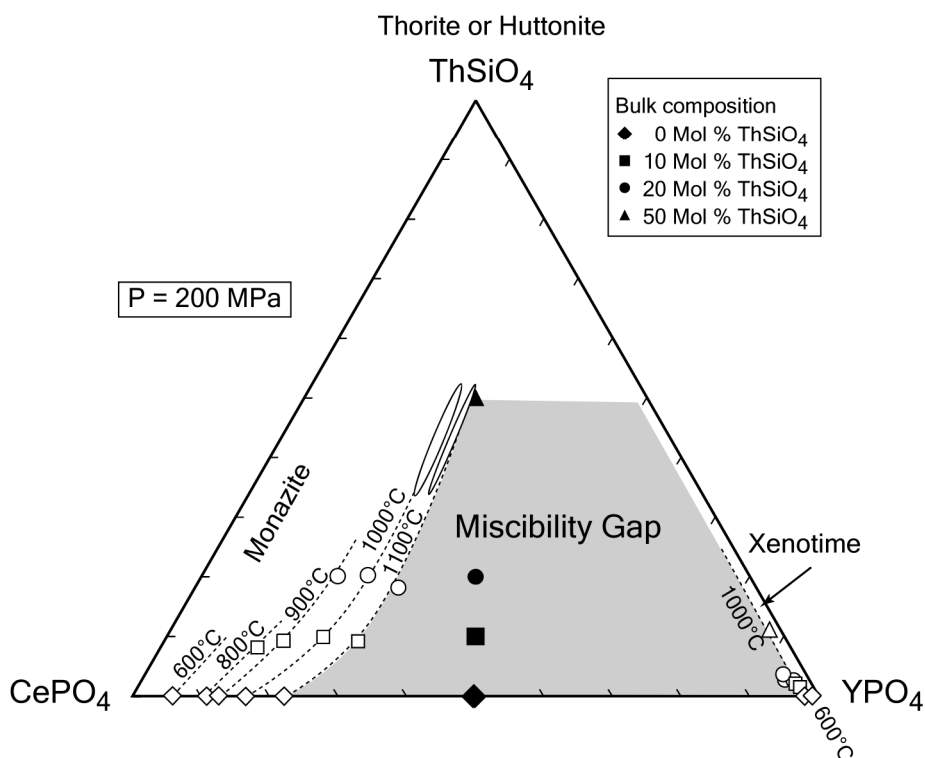


Figure 1: Compositions of monazite and xenotime plotted into the CePO_4 - ThSiO_4 - YPO_4 ternary diagram. Data are from Tables 5 and 6. Ellipses represent scattering of AEM analyses at high ThSiO_4 bulk compositions. Data for the ThSiO_4 -free binary system are from Gratz & Heinrich (1997). Dashed lines represent monazite compositions at the respective temperatures at 200 MPa. For analytical errors see Tables 5 and 6.

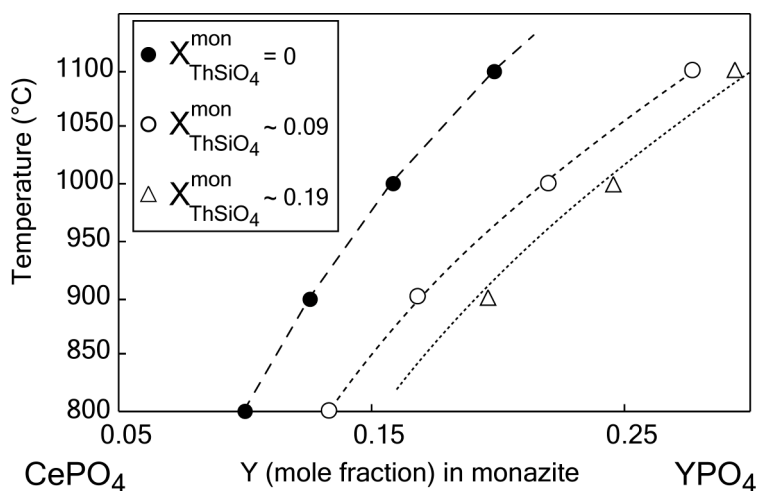


Figure 2: Plot of the concentration of YPO_4 in monazite versus temperature at concentrations of 0 (filled circles); ~ 0.09 (open circles), and ~ 0.19 (triangles). $X_{\text{ThSiO}_4}^{\text{mon}}$ in monazite is nearly independent of temperature for a given bulk composition because ThSiO_4 strongly fractionates into monazite at all temperatures. Data are from Table 5, those for the ThSiO_4 -free system from Gratz & Heinrich (1997). For analytical errors see Table 5.

seen in xenotime compositions indicating that at very high $X_{\text{ThSiO}_4}^{\text{bulk}}$, some ThSiO_4 is now incorporated into xenotime (open triangle in Fig. 1).

3-2 - Rietveld refinement results and composition-volume relationships

Relative amounts of the phases along with their refined lattice parameters are given in Table 4. Details of XRD-patterns from three selected runs at $X_{\text{ThSiO}_4}^{\text{bulk}} = 0.1$ and 1000°C ; $X_{\text{ThSiO}_4}^{\text{bulk}} = 0.5$ and 1000°C ; and at $X_{\text{ThSiO}_4}^{\text{bulk}} = 0.5$ and 900°C are shown in Figure 3.

At $X_{\text{ThSiO}_4}^{\text{bulk}}$ of 0.1 and 0.2 where thorite is absent, the amount of monazite increases with temperature from 0.64 at 800°C to 0.75 at 1100°C , and from 0.74 at 900°C to 0.81 at 1100°C , respectively. Simultaneously, the amount of xenotime decreases from 0.26 at 800°C to 0.18 at 1100°C , and from 0.14 at 900°C to 0.10 at 1100°C . This simply reflects the increasing incorporation of xenotime component into monazite at higher temperatures, in line with the fact that xenotime is always poor in the CePO_4 component.

There is also agreement between compositional data of the REE-phosphates obtained by AEM and their lattice parameters. The monoclinic monazite structure is considerably denser than the tetragonal xenotime structure. The cell volume of pure CePO_4 -monazite is 300.84 \AA^3 , that of pure YPO_4 -xenotime 285.28 \AA^3 . Pure thorite, i.e. ThSiO_4 with xenotime structure has 321.51 \AA^3 and pure huttonite, ThSiO_4 with monazite structure, 297.15 \AA^3 (Taylor & Ewing, 1978; Table 4). A hypothetical YPO_4 -phase with monazite structure had a cell volume of 271.19 \AA^3 and a hypothetical CePO_4 -phase with xenotime structure 321.35 \AA^3 (Gratz & Heinrich, 1997, 1998). In run products with $X_{\text{ThSiO}_4}^{\text{bulk}}$ of 0.1 and 0.2, the unit-cell volumes of xenotimes are in the range of 285.8 \AA^3 to 286.9 \AA^3 which is very similar to that of pure YPO_4 (see also Fig. 3a). Given the distinctly larger cell volumes of tetragonal CePO_4 and ThSiO_4 , this shows that xenotimes are in fact very poor in these components and have uniform compositions close to pure YPO_4 . In contrast, the cell volume of monazite is significantly reduced in all run products (Fig. 3a-c). At $X_{\text{ThSiO}_4}^{\text{bulk}}$ of 0.1, it decreases with increasing temperature from 297.26 \AA^3 at 800°C to 293.55 \AA^3 at 1100°C , and at $X_{\text{ThSiO}_4}^{\text{bulk}}$ of 0.2 from 295.38 \AA^3 at 900°C to 292.89 \AA^3 at 1100°C (Table 4). Since the difference between the unit-cell volumes of monoclinic YPO_4 and CePO_4 is large (29.65 \AA^3), and that of huttonite and CePO_4 small (3.69 \AA^3), the effect is mainly caused by the enhanced incorporation of the

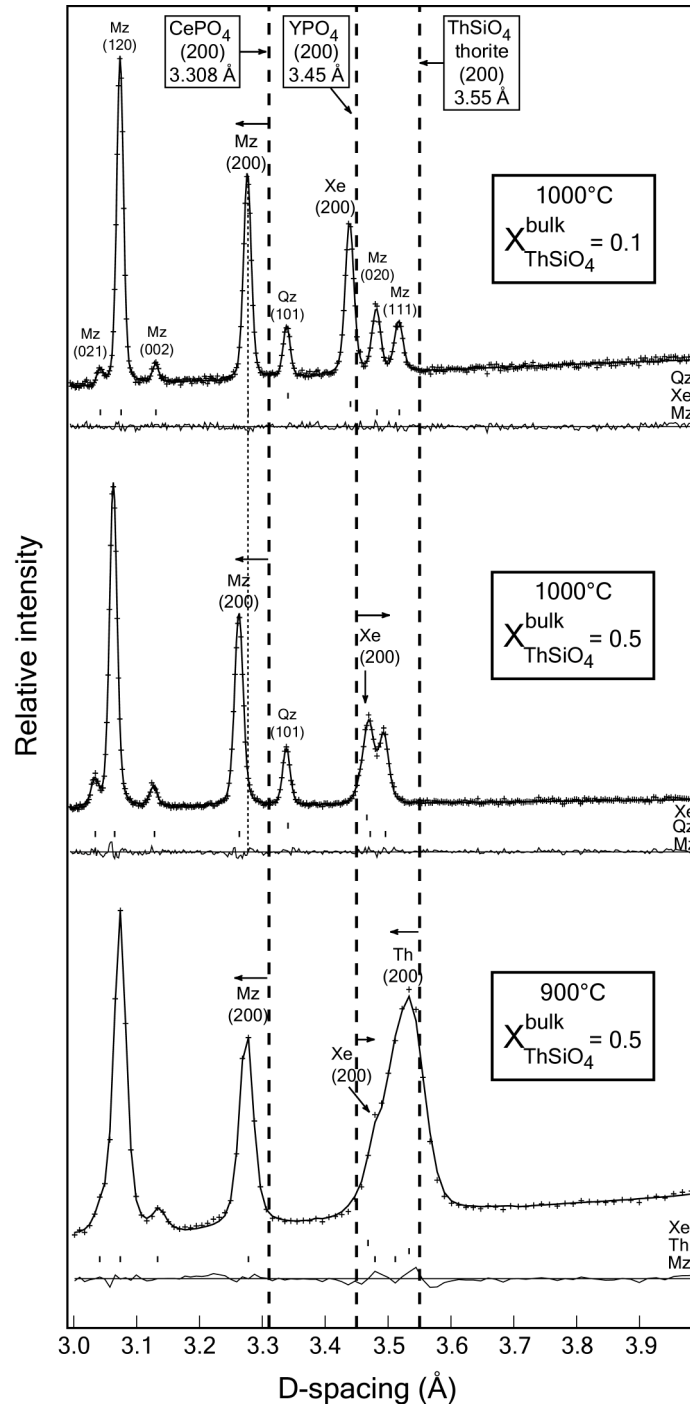


Figure 3: Details of the XRD patterns from MXTh99-54 (1000°C, $X_{ThSiO_4}^{bulk} = 0.1$), MXTh99-56 (1000°C, $X_{ThSiO_4}^{bulk} = 0.5$) and MXTh99-47 (900°C, $X_{ThSiO_4}^{bulk} = 0.5$). Arrows indicate shifts of some reflections relative to the pure endmembers due to incorporation of $ThSiO_4$, $CePO_4$ and YPO_4 . Reflections are broader at high $ThSiO_4$ concentrations and at lower temperature. At $X_{ThSiO_4}^{bulk} = 0.5$, thorite is present at 900°C and disappeared at 1000°C.

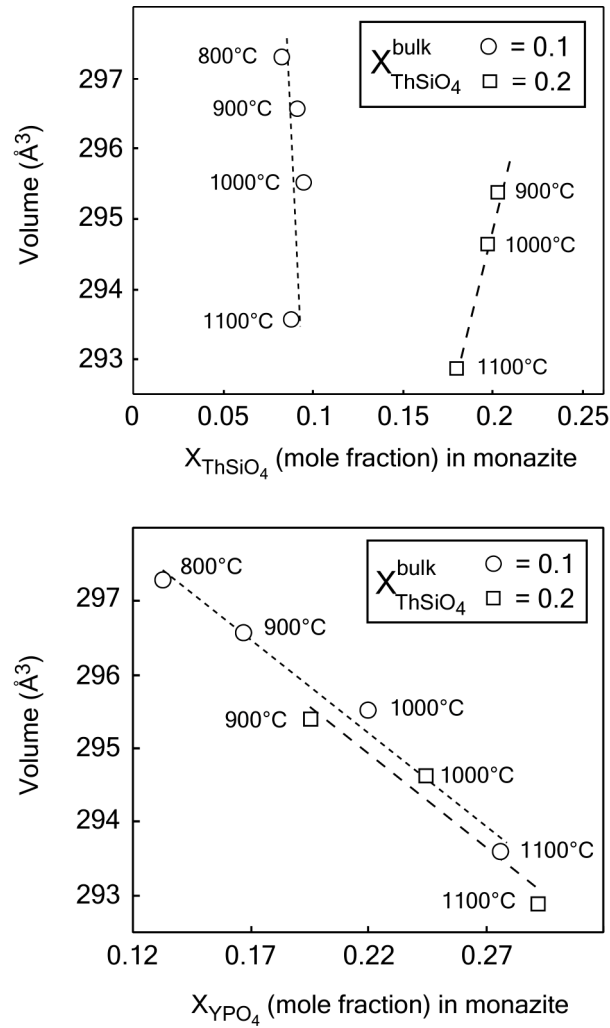


Figure 4: Unit cell volume of monazite at $X_{ThSiO_4}^{bulk} = 0.1$ (open circles) and 0.2 (open squares) versus a) $X_{ThSiO_4}^{mon}$ and b) $X_{YPO_4}^{mon}$. Data are from Tables 4 and 5. Since $X_{ThSiO_4}^{mon}$ is nearly independent of temperature at a given bulk composition (a, see also Fig. 2), the decreasing volume results mainly from increasing incorporation of YPO₄ with increasing temperature (b).

YPO₄- component. The influence of the ThSiO₄ component on the cell volume of monazite is minor. This is shown in Figure 4 where a linear volume reduction with increasing incorporation of ThSiO₄ (a) and YPO₄ (b) is obvious. At $X_{ThSiO_4}^{bulk}$ of 0.1, $X_{ThSiO_4}^{mon}$ is ~ 0.09 at all temperatures (see above) and the cell volume of monazite decreases by about 4 Å³ as $X_{YPO_4}^{mon}$ increases from 0.13 to 0.28. A similar range exists for $X_{ThSiO_4}^{mon}$ of ~ 0.19. If $X_{ThSiO_4}^{mon}$ increases from ~0.09 to ~0.19 at constant temperature, the cell volume is decreased by less than 0.5 Å³. In summary, the compositional results obtained by AEM are fully supported by determination of the lattice parameters via the Rietveld technique.

For experiments with 50 mol% ThSiO₄ in the bulk, thorite appeared as additional phase at low temperatures indicating ThSiO₄ saturation of both REE-phosphates. Rietveld analysis showed that the amount of thorite decreases strongly with increasing temperature from 0.56 (weight fraction) at 600°C to 0.47 at 800°C, and to 0.29 at 900°C, accompanied by an increasing amount of monazite which is 0.39 (weight fraction) at 600°C, 0.51 at 800°C, and 0.69 at 900°C (Table 4). At 1000°C and 1100°C, the amount of monazite further increased and thorite is absent (Fig. 3b,c). Obviously, the incorporation of the ThSiO₄-component into monazite depends strongly on temperature and the miscibility gap along the monazite-thorite-rich side of the ternary narrows rapidly as temperature increases (see below). Though precise compositional data at $X_{ThSiO_4}^{bulk} = 0.5$ are not available, the evolution of the system to higher temperatures is also seen in the lattice parameters of the phases. The unit-cell volume of monazite continuously decreases from 297.52 Å³ at 600°C to 292.67 Å³ at 1100°C, mainly reflecting the enhanced incorporation of the YPO₄ component. Again, the influence of the ThSiO₄ component on the cell volume of monazite is only minor (see above). The unit cell of xenotime at 800°C is 290.89 Å³, considerably larger than in runs at all temperatures with low ThSiO₄-contents in the bulk. Because thorite has a larger volume this indicates that at $X_{ThSiO_4}^{bulk} = 0.5$ significant amounts of ThSiO₄ are incorporated into xenotime, in line with AEM results (open triangle in Fig. 1). There is also a continuous increase of the xenotime cell volume with increasing temperature from 290.50 Å³ at 600°C to 293.42 Å³ at 1100°C. This is interpreted as enhanced ThSiO₄ incorporation with temperature. The effect cannot result from enhanced CePO₄ incorporation because this is not seen at low bulk ThSiO₄ contents. Finally, the unit cell volume of thorite is 315.44 Å³ at 600°C, 313.85 Å³ at 800°C, and 312.60 Å³ at 900°C, which is by far smaller than that of pure thorite (321.51 Å³; Table 4). The unit-cell

volumes of thorite and hypothetical CePO_4 in thorite structure are very similar (321.51 \AA^3 vs. 321.35 \AA^3), that of YPO_4 , however, much smaller (285.28 \AA^3). Thus, the smaller cell volume of thorite results from large amounts of YPO_4 in the structure, which is enhanced by increasing temperature.

4 – Discussion

4-1 - A tentative diagram of phase relations in the ternary system CePO_4 - YPO_4 - ThSiO_4

We have shown above that, despite the somewhat limited analytical database, bulk composition, phase compositions, and relative amounts of the phases agree within analytical errors indicating that equilibrium conditions have been achieved. This allows for establishing a tentative phase diagram of the CePO_4 - YPO_4 - ThSiO_4 ternary at the relevant P-T-conditions. Three isothermal sections at 200 MPa and 600°C, 900°C, and 1000°C are shown in Figure 5. At low ThSiO_4 concentrations in the bulk, where the system is two-phase, monazite and xenotime compositions are well constrained. Tie-lines indicate preferential incorporation of the ThSiO_4 component into monazite at all temperatures. At high $X_{\text{ThSiO}_4}^{\text{bulk}}$, the system is three-phase, however, the three-phase stability field strongly shrinks with increasing temperature. Monazite has the most flexible structure expanding its stability field with temperature by enhanced incorporation of both the ThSiO_4 and the YPO_4 components. Xenotime has a very small stability field, which is moderately expanded towards the ThSiO_4 apex as temperature increases. The shape of the thorite stability field is uncertain because appropriate analytical data are not available.

An important point is that the ThSiO_4 phase in our experiments is thorite, thus confirming earlier experiments by Seydoux & Montel (1997) on the thorite-huttonite phase transition which revealed that thorite is the stable polymorph at low P-high T, and huttonite at high P-low T conditions. This is further supported by phase assemblages in low to medium grade metapelites where monazite + xenotime + thorite parageneses have been described (*e.g.* Franz *et al.*, 1996). REE-, Y-, and Th-rich assemblages in a variety of granites showed that thorite coexisting with monazite and xenotime is always enriched in the HREE+Y- relative to the LREE components (Bea, 1996), in line with the shape of the thorite stability field derived from our experiments (Figure 5). In the rocks described by Bea (1996) "some P-rich ThSiO_4 varieties having high concentrations of LREE are probably intermediate monazite-

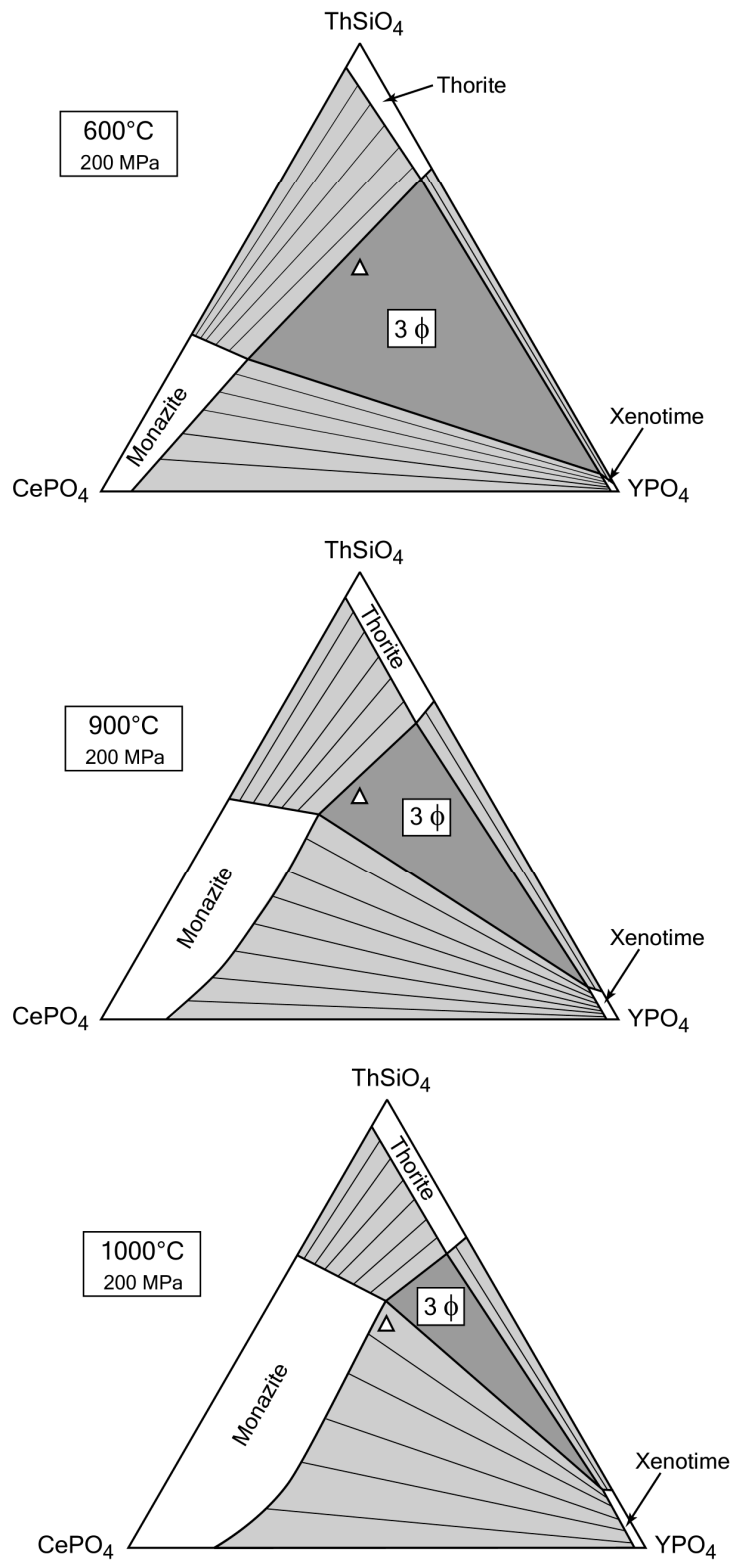


Figure 5: Tentative diagram of phase relations in the $CePO_4$ - $ThSiO_4$ - YPO_4 ternary system at 600°C, 900°C and 1000°C at 200 MPa. At $X_{ThSiO_4}^{bulk} = 0.5$ and equal amounts of $CePO_4$ and YPO_4 (open triangle) the system is three-phase at 900°C, and two-phase at 1000°C (Table 4). The diagram assumes tetragonal thorite as the stable $ThSiO_4$ polymorph along the complete temperature range (see text).

huttonite phases” which exactly correspond to our ThSiO₄-rich monazites coexisting at high temperatures. Noteworthy, monazites with $X_{ThSiO_4}^{mon}$ of about 0.5, such as formed in runs MXTh99-56 and MXTh0-7 and analysed in granites by Bea (1996) are termed huttonitic monazite (Bowie & Horne, 1953) though thorite is the coexisting ThSiO₄ polymorph at low pressure conditions.

4-2 - The monazite-xenotime thermobarometer in presence of ThSiO₄

The thermobarometric potential of monazite coexisting with xenotime lies in the fact that incorporation of the HREE and particularly of Y into monazite is strongly temperature and only slightly pressure-dependent. Experimental calibrations of the monazite geothermometer are restricted to the binary system CePO₄-YPO₄ (Gratz & Heinrich, 1997), the ternary system CePO₄-GdPO₄-YPO₄ (Gratz & Heinrich, 1998), and the (REE+Y)PO₄ multicomponent system where the relative amounts of REE corresponded to REE distributions typical for metapelitic rocks (Andrehs & Heinrich, 1998). An empirical calibration using monazite-xenotime pairs from a suite of metapelites that equilibrated over a large P-T range was presented by Heinrich *et al.* (1997). Based on these calibrations, monazite-xenotime equilibria have been successfully applied for thermobarometry and thermochronometry of a wide range of low to high grade felsic metamorphic rocks (*e.g.* Pyle *et al.*, 2001; Viskupic & Hodges, 2001). However, discrepancies do exist, suggesting that in some cases calculated temperatures exceed true temperatures by about 50 to 100°C. A reasonable explanation is that the influence of the ThSiO₄ component on the thermometer has been, so far, not considered.

Our experiments have shown that the amount of the YPO₄ component in monazite increases relative to the Th-free system if significant amounts of ThSiO₄ are present within the structure. ThSiO₄ favours incorporation of YPO₄ resulting in a shift of the monazite limb and the shrinkage of the miscibility gap. For a nearly constant $X_{ThSiO_4}^{mon}$ of 0.09, $X_{YPO_4}^{mon}$ increased from 0.13 at 800°C to 0.28 at 1100°C, whereas in the Th-free system it ranges from 0.09 to 0.20 along the same temperature range (Fig. 3). Values of $X_{ThSiO_4}^{mon} \sim 0.09$ correspond to monazites with about 10wt% ThO₂, which are typical upper values for monazites from felsic metamorphic rocks (Franz *et al.*, 1996; Pyle *et al.*, 2001; Viskupic & Hodges, 2001). Figure 6 shows an $X_{YPO_4}^{mon}$ versus temperature plot with the position of the two monazite limbs. The

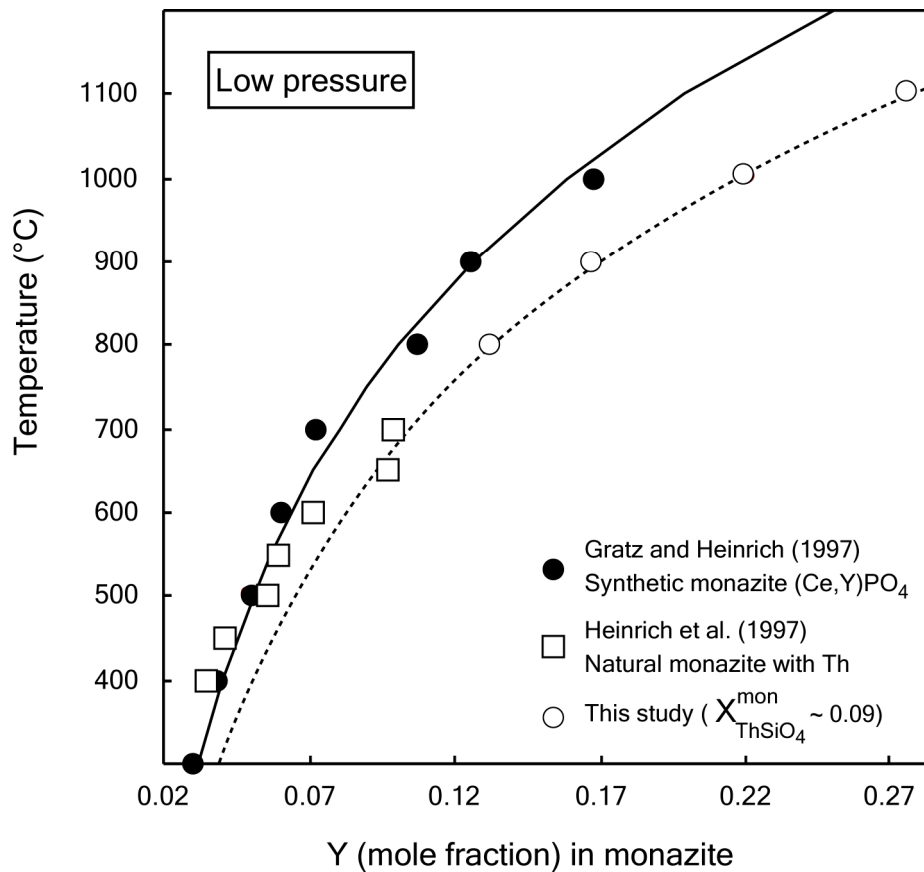


Figure 6: Temperature-dependent incorporation of YPO₄ into monazite coexisting with xenotime. Filled circles: Synthetic monazite from the CePO₄-YPO₄ binary (Gratz and Heinrich, 1997). Open squares: Natural monazites with varying Th concentrations equilibrated from greenschist to granulite facies conditions at 300 to 500 MPa (Heinrich et al., 1997). Open circles: this study; only monazite compositions with $X_{\text{ThSiO}_4}^{\text{mon}}$ of about 0.09 are shown, corresponding to $X_{\text{ThSiO}_4}^{\text{bulk}} = 0.1$.

ThSiO₄-free limb using experimental data from Gratz & Heinrich (1997) has been calculated with:

$$T (^{\circ}\text{C}) = 439.75 \ln(X_Y) + 1810.4 \quad (1)$$

For $X_{\text{ThSiO}_4}^{\text{mon}} \sim 0.09$ the values of this study have been extrapolated to lower temperatures using the empirical fit of

$$T (^{\circ}\text{C}) = 410.62 \ln(X_Y) + 1663.3 \quad (2).$$

It is obvious that for any given $X_{\text{YPO}_4}^{\text{mon}}$ in the relevant temperature range between 400°C and 750°C, calculated temperatures are too high by about 50 to 70°C, if the ThSiO₄ component in monazite is neglected. This gains further support from observations of Viskupic & Hodges (2001) on monazite-xenotime pairs in gneisses from the Nepalese Himalaya. There, populations of monazite with varying ThO₂ concentrations on a thin section scale exist. Calculations using the Gratz & Heinrich thermobarometer gave, for example, 640°C on Th-poor monazites, in good agreement with phase relations and phase compositions of coexisting silicates. With the same calibration, however, temperatures of up to 100°C higher resulted for Th-rich monazites within the same specimen. That the monazite-xenotime thermobarometer must be corrected for Th is also seen in the empirical calibration of Heinrich *et al.* (1997; squares in Fig. 6). Most $X_{\text{YPO}_4}^{\text{mon}}$ of monazite-xenotime pairs *versus* temperature estimated from silicate phase compositions plot towards higher values, implicitly indicating that ThO₂ is present in most monazites (see also analyses in Franz *et al.*, 1996).

5 - Concluding remark

Thorium incorporation into monazite via the coupled substitution $\text{Th} + \text{Si} \Leftrightarrow \text{REE} + \text{P}$ is not the only substitution mechanism. The brabantite substitution $\text{Th} + \text{Ca} \Leftrightarrow 2 \text{REE}$ is also important. Compositions of metamorphic monazite-xenotime pairs show that Th is also strongly fractionated into monazite if this mechanism is operating (*e.g.* Franz *et al.*, 1996; Pyle *et al.*, 2001; Viskupic & Hodges 2001). One may reasonably assume that enhanced brabantite incorporation would also favour increased incorporation of the xenotime component, with similar effects on the monazite-xenotime thermobarometer. Quantitative informations, however, must await further experimental results on the CaThPO₄-bearing system.

Acknowledgements

We thank I. Bauer for providing the XRD analyses and K. Paech for the preparation of the TEM samples. Thanks go also to R. Schulz for providing the experiments using IHPV. We thank M. Gottschalk for introduction to the Rietveld technique and its helpful discussions.

References

- Andrehs, G. & Heinrich, W. (1998): Experimental determination of REE distributions between monazite and xenotime: potential for temperature-calibrated geochronology. *Chem. Geol.*, **149**, 83-96.
- Barth, S., Oberli, F., Meier, M. (1994): Th-Pb versus U-Pb isotope systematics in allanite from co-genetic rhyolite and granodiorite: implications for geochronology. *Earth Planet. Sci. Lett.*, **124**, 149-159.
- Bea, F. (1996): Residence of REE, Y, Th and U in Granites and crustal protholiths; implications for the chemistry of crustal melts. *J. Petrol.*, **37**, 521-552.
- Berzelius, J.J. (1829): Undersokning at ett nytt mineral (Thorit). *Akad. Stockholm Handl.*, **1**, not seen, cited in Smitts, 1989.
- Bowie, S.H.U. & Horne, J.E.T. (1953): Cheralite, a new mineral of the monazite group. *Mineral. Mag.*, **30**, 93-99.
- Cliff, G. & Lorimer, G.W. (1975): The quantitative analysis of thin specimens. *J. Microsc.*, **103**, 203-207.
- Cocherie, A., Legendre, O., Peucat, J.J., Kouamelan, A.N. (1998): Geochronology of polygenetic monazites constrained by in situ electron microprobe Th-U-total lead determination: implications for lead behavior in monazite. *Geochim. Cosmochim. Acta*, **62**, 2475-2497.

- Crowley, J.L. & Ghent, E.D. (1999): An electron microprobe study of the U-Th-Pb systematics of metamorphosed monazite: the role of Pb diffusion versus overgrowth and recrystallization. *Chem. Geol.*, **157**, 285-302.
- Egerton, R.F. (1996): Electron energy-loss spectroscopy in the electron microscope. Plenum Press, New York, 301-306.
- Förster, H.J. (1998a): The chemical composition of REE-Y-Th-U-rich accessory minerals in peraluminous granites of the Erzgebirge-Fichtelgebirge region, Germany, Part I: The monazite-(Ce)-brabantite solid solution series. *Am. Mineral.*, **83**, 259-272.
- , — (1998b): The chemical composition of REE-Y-Th-U-rich accessory minerals in peraluminous granites of the Erzgebirge-Fichtelgebirge region, Germany, Part II: xenotime. *Am. Mineral.*, **83**, 1302-1315.
- Franz, G., Andrehs, G., Rhede, D. (1996): Crystal chemistry of monazite and xenotime from Saxothuringian-Moldanubian metapelites, NE Bavaria, Germany. *Eur. J. Mineral.*, **8**, 1097-1118.
- Gratz, R. & Heinrich, W. (1997): Monazite-xenotime thermobarometry: experimental calibration of the miscibility gap in the binary system CePO_4 - YPO_4 . *Am. Mineral.*, **82**, 772-780.
- Gratz, R. & Heinrich, W. (1998): Monazite-xenotime thermobarometry. III. Experimental calibration of the partitioning of Gd between monazite and xenotime. *Eur. J. Mineral.*, **10**, 579-588.
- Grove, M. & Harrison, T.M. (1999): Monazite Th-Pb age depth profiling. *Geology*, **27**, 487-490.
- Harlov, D. & Förster, H.J.: High grade fluid metasomatism on both a local and regional scale: the Seward Peninsula, Alaska and the Val Strona di Omega, Ivrea-Verbano Zone, Northern Italy. Part II: phosphate mineral chemistry. *In Press in J. Petrol.*

- Harrison, T.M., McKeegan, K.D., LeFort, P. (1995): Detection of inherited monazite in the Manaslu leucogranite by $^{208}\text{Pb}/^{232}\text{Th}$ ion microprobe dating: Crystallization age and tectonic implications. *Earth Planet. Sci. Lett.*, **133**, 271-282.
- Heinrich, W., Andrehs, G., Franz, G. (1997): Monazite-xenotime miscibility gap thermometry: I. An empirical calibration. *J. Metamorphic Geol.*, **15**, 3-17.
- Joy, D.C., Romig, A.D., Goldstein, J.I. (1989): Principles of analytical electron microscopy. *Plenum Press New-York and London*.
- Larson, A.C. & Von Dreele, R.B. (1988): GSAS-Generalized structure analysis system. *Los Alamos National Laboratory Report LAUR*, **86-758**, 1-150.
- Montel, J.M., Foret, S., Veschambre, M., Nicollet, C., Provost, A. (1996): Electron microprobe dating of monazite. *Chem. Geol.*, **131**, 37-53.
- Ni, Y., Hughes, J.M., Mariano, A.N. (1995): Crystal chemistry of the monazite and xenotime structures. *Am. Mineral.*, **80**, 21-26.
- Pabst, A. & Hutton, C.O. (1951): Huttonite a new monoclinic thorium silicate. *Am. Mineral.*, **36**, 60-69.
- Paquette, J.L., Montel, J.M., Chopin, C. (1999): U-Th-Pb dating of the Brossasco ultrahigh-pressure metagranite, Dora-Maira massif, western Alps. *Eur. J. Mineral.*, **11**, 69-77.
- Parrish, R.R. (1990): U-Pb dating of monazite and its application to geological problems. *Can J. Earth Sci.*, **27**, 1431-1450.
- Parrish, R.R. & Carr, S.R. (1994): U-Pb problematics of very high-U accessory minerals: examples from the Himalaya and Cordillera and implication for U-Pb geochronology. *Abstract ICOG 8, U.S.G.S. Circular*, **1107**, p. 128.

- Podor, R. & Cuney, M. (1995): Experimental study of the solid solution between monazite-(La) and $(\text{Ca}_{0.5}\text{U}_{0.5})\text{PO}_4$ at 780°C and 200 MPa. *Am. Mineral.*, **80**, 1261-1268.
- Podor, R. & Cuney, M. (1997): Experimental study of Th-bearing LaPO_4 (780°C, 200 MPa): implications for monazite and actinide orthophosphate stability. *Am. Mineral.*, **82**, 765-771.
- Poitrasson, F., Chenery, S., Shepherd, T.J. (2000): Electron microprobe and LA-ICP-MS study of monazite hydrothermal alteration: Implications for U-Th-Pb geochronology and nuclear ceramics. *Geochim. Cosmochim. Acta.*, **64**, 3283-3297.
- Pyle, J.M., Spear, F.S., Rudnick, R.L., McDonough, W.F. (2001): Monazite-xenotime-garnet equilibrium in metapelites and a new monazite-garnet-thermometer. *J. Petrol.*, **42**, 2083-2107.
- Seydoux, A.M. & Montel, J.M. (1997): Experimental determination of the Thorite-Huttonite phase transition. *EUG IX, Terra Nova 9, Abstract Supplement 1*, p.421.
- Seydoux-Guillaume, A.M., Paquette, J.L., Wiedenbeck, M., Montel, J.M., Heinrich, W.: Experimental resetting of the U-Th-Pb system in monazite. *Submitted to Chem. Geol.*
- Taylor, M. & Ewing, R.C. (1978): The crystal structures of ThSiO_4 polymorphs: huttonite and thorite. *Acta Crystallogr.*, **B34**, 1074-1079.
- Van Emden, B., Thornber, M.R., Graham, J., Lincoln, F.J. (1997): The incorporation of actinides in monazite and xenotime from placer deposits in western Australia. *Can. Mineral.*, **35**, 95-104.
- Viskupic, K. & Hodges, K.V. (2001): Monazite-xenotime thermochronometry: methodology and an example from the Nepalese Himalaya. *Contrib. Mineral. Petrol.*, **141**, 233-247.

CHAPTER II

Structure of a natural monazite: behaviour under heating

“La pensée n’est qu’un éclair au milieu de la nuit. Mais c’est cet éclair qui est tout.”

Henri Poincaré - *La Valeur de la science*

An XRD, TEM and Raman study of experimental annealing of natural monazite

Abstract

The healing of radiation damage in natural monazite has been experimentally studied using XRD, TEM, Raman microprobe and Cathodoluminescence analysis. The starting material was a chemically homogeneous monazite from a Brazilian pegmatite with a concordant age of 474 ± 1 Ma showing nm-scale defects induced by radioactive decay. The X-ray pattern of the unheated starting material revealed two distinct “phases” (A) and (B). These are interpreted as two monazites with slightly different lattice parameters. Monazite (A) shows sharp reflections of high amplitudes and slightly expanded lattice parameters compared to a standard monazite. The second “phase”(B) exhibits very broad reflections of low amplitudes. Two sets of experiments were performed. First, dry monazite powder was annealed at 500, 800 and 1000°C for 7 days. Each run product was analysed by X-Ray diffractometry. Second, monazite grains were hydrothermally annealed at temperatures from 500 to 1200°C for about 10 days. TEM observations showed that partial healing of the monazite lattice already occurred at 500°C and increased gradually with temperature, so that after 10 days at 900°C complete healing was achieved.

The observations are interpreted accordingly: unheated monazite has a mosaic structure consisting of two domains (A) and (B), which are basically two monazite crystals with different lattice parameters. Diffraction domains (A) show sharp reflections of high amplitudes and a well-crystallised lattice with only a small volume expansion (1%). Diffraction domains (B) exhibit very broad reflections of low amplitudes and represent a distorted lattice. We suggested that the (A) domains correspond to well-crystallised areas where He atoms are trapped. The He causes expansion of the (A) monazite lattice. Diffraction domains (B) are interpreted as a He-free distorted monazite crystal lattice, which can be referred to old alpha-recoil tracks. They are composed of “islands” with an expanded lattice, induced by the presence of interstitials, and “islands” of a compressed monazite lattice, induced by presence of vacancies. Both the “islands” will pose stress on the lattice in the vicinity of the islands. The broadening of the B-reflections is due to the expanded or compressed diffraction domains and due to the different amount of the distortion.

With increasing temperature He diffuses out of the lattice of monazite, thus inducing a relaxation of the lattice that results in a decrease of the unit-cell volume, i.e. the positions of the A-reflections shift to smaller d_{hkl} values. At the same time, the nm-sized defect domains (B) are healed. At 900-1000°C only one phase remains that is a monazite with well-crystallised lattice and minimum unit cell volume.

Keywords: Monazite • annealing • Helium • XRD • TEM

1 - Introduction

Monazite, the natural light rare earth orthophosphate, is widely used in U-Th-Pb geochronology (Parrish 1990) because of its high actinide content (up to 6 wt-% UO_2 and up to 20 wt-% ThO_2). In contrast to zircon, monazite is mostly concordant in a U-Pb concordia diagram (Schärer et al. 1986; Corfu 1988; Smith and Barreiro 1990; Landzirotti and Hanson 1995; Parrish 1995). This U-Pb concordance means that during most geological events the monazite U-Pb system is either completely reset or remains totally unaffected. To understand the significance of the U-Pb ages measured from monazite samples, one needs to understand the mechanism of U-Pb resetting.

Two processes are commonly considered to explain the resetting of an isotopic system: loss of Pb by volume diffusion out of the monazite grain or dissolution via a coexisting fluid and precipitation of a new-formed lead-free monazite. Dodson (1973) investigated the resetting by diffusion theoretically. In this model the resetting results from the outward diffusion of the daughter elements (here Pb) out of the crystal. This model introduces the concept of a closure temperature, which depends on the size of the crystal, its shape, the cooling rate during the geological event, and the diffusion coefficient of the daughter elements. For example, in a metamict crystal, Pb is able to diffuse relatively fast along the interfaces between amorphous and crystalline domains in comparison to the diffusion in the amorphous and in the crystalline domains themselves (Cherniak 1991, 1993; Murakami et al. 1991; Salje 2000; Weber et al. 1998). The resetting by a dissolution-precipitation mechanism is based on the dissolution of the crystal in a melt or in a fluid phase, followed by a re-precipitation of a newly formed crystal without re-incorporation of the daughter element. No detailed model for dissolution precipitation resetting is available, but we can predict that the kinetics of dissolution, the solubility of the crystal and the nature of the fluid phase to be important parameters.

However, for the U-Th-Pb systems, the radioactive decay produces also radiation damage that may partially or totally destroy the crystal lattice, thus producing a so-called metamict crystal. Whatever the mechanism of resetting is considered to be, it can be anticipated that the kinetics of resetting will be strongly influenced by the degree of metamictization of the crystal.

Previous studies on metamictization:

The monazite studied in the present work contains considerable amount of ^{232}Th , ^{238}U and ^{235}U (Table 1). Their radioactive decay produces 6, 8, and 7 α -particles, respectively, until ^{208}Pb , ^{206}Pb and ^{207}Pb are finally created. During an α -event a heavy atom nucleus liberates its energy by ejecting an α -particle (^4He -nuclei), which carries 98% of the initial energy. The α -particle, which has an energy between 3.9 to 8.4 MeV (Firestone and Shirley 1996), is ejected to about 10-40 μm (Owen 1988; Ewing et al. 2000; Nasdala et al. 2001b) from the point of disintegration. It dissipates most of its energy by ionisation along of its path with limited elastic collisions occurring at the end of its trajectory (Nasdala et al. 2001a) and produces isolated defects (~ 100 atomic displacements). These isolated defects or Frenkel pairs consist also of vacant and interstitial sites that may increase the unit-cell volume of the crystal. In contrast, the remaining nucleus is recoiled in an opposite direction to about 10-20 nm from the α -particle, according to the principle of momentum conservation, and causes collision cascades (~ 700 -1000 atomic displacements) (Gögen and Wagner 2000; Nasdala et al. 2001b). Most of the atomic displacements leading to amorphization of a crystal lattice are caused by alpha-recoil nuclei (Ewing et al. 1995; 2000; Nasdala et al. 1996; Weber et al. 1998).

In contrast to zircon (Speer 1982), metamict monazite is rarely found in nature (Ewing 1975). Even old, radioactive monazites are mostly crystalline, despite the intensive radiation doses they received. However, there is some evidence of radiation damage in natural monazite grains, which are limited to isolated domains within the crystal (Black et al. 1984; Meldrum et al. 1998). This suggests that, even at low temperature, the monazite lattice is healed easily (Boatner and Sales 1988).

Radiation damage in minerals can also be induced by using external heavy-ion irradiation. For most crystals it is possible to define an amorphization dose above which the crystal is totally metamict (amorphous state). The amorphization dose increases with increasing temperature and reaches a critical temperature above which amorphization can no longer be achieved, because the crystal lattice is faster thermally reconstructed than it is destroyed.

The results of intensive irradiation studies carried out on silicates and phosphates with monazite or zircon structure can be summarised as follows. At room temperature, the amorphization dose is similar for all the investigated structures. It shows that monazite is not specifically resistant to radiation damages. The main difference is based on the critical

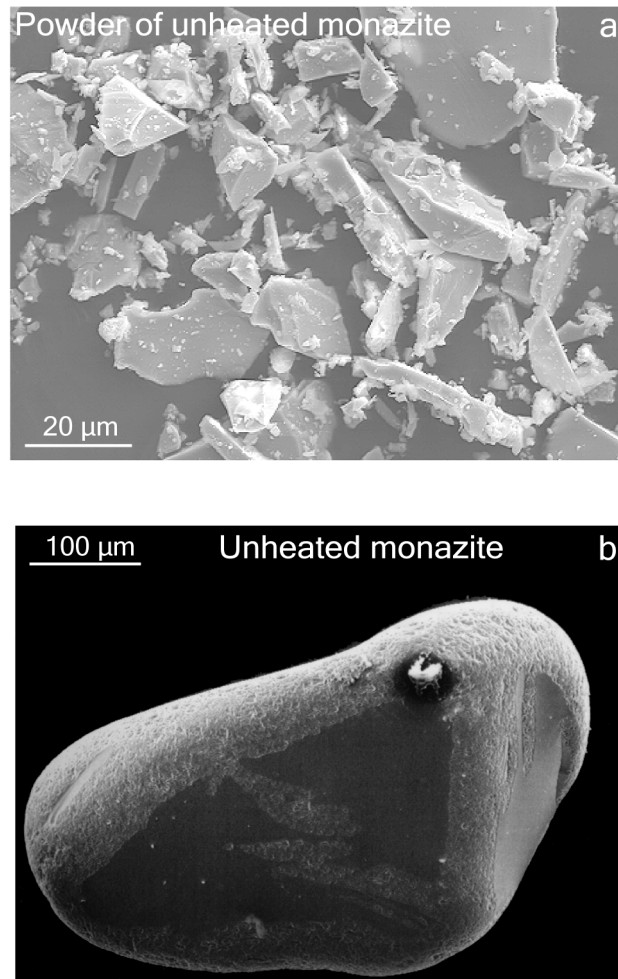


Figure 1: SEM micrographs illustrating textural characteristics observed in unheated monazite.

a) powder of monazite grains

b) an abraded monazite grain

temperature, which for monazite is in the range 100-200°C, but for zircon is above 1000°C (Meldrum et al. 1996; 1997; 1998; 2000). Therefore monazite is able to restore its structure at low temperature, although it is not specifically resistant to radiation damage.

Previous works on the annealing of monazite provided different results. Karioris et al. (1981) in a X-ray diffraction (XRD) study, and Meldrum et al. (1998) in a Transmission Electron Microscopy (TEM) study, both using an ion-beam-amorphised monazite, observed recrystallization at 300 and 450°C respectively. In contrast, in a XRD study Smith and Giletti (1997) completely healed a natural crystalline monazite between 800°C and 1100°C.

The present paper shows the results of annealing experiments using a natural crystalline monazite. Using XRD and TEM (High-Resolution Transmission Electron Microscopy (HRTEM) and Dark Field (DF)), the annealing of radiation damages was evaluated. The experimental work is completed by first attempts to document the structural recovery of heat-treated monazites by Raman spectroscopic and CL (cathodoluminescence) analyses. Implications of our results for U-Pb geochronology and nuclear waste storage are discussed.

2 - Experimental

2-1 - Starting material

A yellow-orange single crystal of monazite (3 × 2 cm in size) from a Brazilian pegmatite (Cruz et al. 1996) was used for this study. Scanning electron microscopy and optical microscopy observations showed that the crystal is almost free of solid or fluid inclusions. The chemical composition was determined using electron microprobe Cameca SX 50. The operating conditions were given in Förster (1998). The crystal is homogeneous on the micron scale. It contains about 1300 ppm of U, 69000 ppm of Th and 1600 ppm of Pb (Table 1).

The age of the crystal was determined by U-Pb dating. It is concordant in a U-Pb concordia diagram at 474 ± 1 Ma (Seydoux et al. 1999; Seydoux-Guillaume et al. submitted). From the Pb, U and Th content and the age, a time-integrated α -dose of about 2.43×10^{16} α /mg is calculated, which corresponds to about 2 dpa (displacements per atom).

Previous X-ray diffraction patterns obtained with Si as an internal standard showed that the starting material is well crystallised and following cell-parameters were derived: $a=6.815(1)$ Å, $b=7.021(1)$ Å, $c=6.496(1)$ Å, $\beta=103.91(1)^\circ$.

Table 1 - EMP analyses of unheated monazite (Moacir 0).

Oxides	Wt %	Cations
La ₂ O ₃	14.51	0.860
Ce ₂ O ₃	30.59	1.799
Pr ₂ O ₃	3.14	0.184
Nd ₂ O ₃	10.20	0.585
Sm ₂ O ₃	2.05	0.114
Gd ₂ O ₃	0.94	0.050
Dy ₂ O ₃	0.11	0.006
Er ₂ O ₃	0.05	0.002
SiO ₂	1.42	0.229
Y ₂ O ₃	0.71	0.061
P ₂ O ₅	27.81	3.782
CaO	0.44	0.076
ThO ₂	6.92	0.253
UO ₂	0.13	0.005
PbO	0.16	0.007
Total	99.19	8.011

The data represent an average of 30 analyses of a 400 µm in diameter single grain. Cations per formula unit are calculated on the basis of 16 Oxygens.

Table 2 - Experimental conditions of annealing experiments.

Run	Description	Temperature (°C)	Pressure (bar)	Duration (days)
VRM97-1	single grain	500	1000	12
VRM97-2	"	800	"	15
VRM98-1	"	900	7000	10
VRM97-10	"	1000	"	7
VRM97-6	"	1200	"	5
Mo500-24	powder	500	1	1
Mo500-48	"	"	"	2
Mo500-72	"	"	"	3
Mo500-96	"	"	"	4
Mo500120	"	"	"	5
Mo500-6d	"	"	"	6
Mo500-7d	"	"	"	7
Mo50014d	"	"	"	14
Mo50030d	"	"	"	30
Mo800-7d	powder	800	1	7
Mo80014d	"	"	"	14
Mo80021d	"	"	"	21
Mo80030d	"	"	"	30
Mo10007d	powder	1000	1	7

2-2 - Annealing experiments

Dry and wet annealing experiments were performed. Dry annealing was carried out by heating monazite powdered at different temperatures and run durations, in order to study the evolution of XRD patterns with temperature and time. The starting monazite was crushed in an agate mortar into a fine powder with a grain size in the range of $< 1 \mu\text{m}$ to $20 \mu\text{m}$ (Figure 1a). About 20 mg of this powder was heated for 7 days at 500, 800 and 1000°C in a platinum crucible using a chamber furnace Heraeus K1252 (Table 2). In order to investigate the kinetics of annealing, experiments at 500°C and 800°C were performed for different run durations (Table 2). Subsequently, run products were prepared for X-ray powder diffraction investigations.

Single grains of the starting monazite were heated hydrothermally, in order to study the evolution of the lattice healing with temperature. Monazite with a grain size of $200\text{-}400\mu\text{m}$ was used as a starting material. The grains were abraded by compressed air (1.15 bars, 20 hours) and grains free of inclusion, free of impurities, and well-rounded (Figure 1b) were selected carefully for the experiments (Seydoux-Guillaume et al. submitted). 10 grains were placed in a platinum capsule together with $20\mu\text{l}$ of ultrapure water. The capsules ($15\times 3\times 0.2\text{mm}$) were sealed by welding and checked for leaks by heating them at 110°C for 24 hours. Experiments were carried out in standard cold seal hydrothermal pressure vessels at 2 kbar and 500 and 800°C and in an internally heated pressure vessel at 7 kbar and 900, 1000, and 1200°C (Table 2). Run durations were about 10 days. Maximum error in the temperature measurements was $\pm 10^\circ\text{C}$. At the end of each run, the vessels were quenched to room temperature within a few minutes. Run products were washed with ultrapure water and prepared for TEM.

2-3 - Analytical methods

- XRD

1 mg of each powder of monazite was measured in transmission mode using a fully automated STOE STADI P diffractometer ($\text{Cu-K}_{\alpha 1}$ radiation) equipped with a primary monochromator and a 7° -position sensitive detector (PSD). The spectra were recorded in the range of $5\text{-}125 (2\theta)$ using a step interval of 0.1° . The resolution of the PSD was set to 0.02° . Counting time was set to 135 s per detector step. Peak positions were calibrated externally using the NBS SRM-640b silicon standard. The unit-cell refinements were performed using the Rietveld-refinement program of the GSAS software package (Larson and Von Dreele

1988). XRD patterns were also recorded for all samples in the range of 26-28° (2 θ), which corresponds to the position of the reflection (200) of the monazite. Counting time was set to 1000 s per detector step. XRD patterns in the range of 26-28° (2 θ) were fitted by a Gauss + Lorentz Area function, in order to measure the full width at half maximum (FWHM), amplitudes, areas and diffraction maximum positions of the (200) reflection.

- TEM

The single crystals were cut in random orientation and TEM foils were prepared by hand polishing and ion milling at 5 kV. TEM studies were carried out using a Philips CM 200 TEM operated at 200 kV using a LaB₆ electron source. HRTEM images were acquired as energy filtered images applying a 10 eV window to the zero-loss peak using a Gatan GIFTM system.

- Raman analysis

Raman spectra were obtained using a Renishaw RM 1000, which is a notch filter-based Raman spectrometer equipped with Leica DMLM optical microscope and Peltier-cooled CCD (charge-coupled device) detector. He-Ne 632.8 nm (3 mW) excitation was used. Measurements were done with a Leica 50 \times objective (numerical aperture 0.75). A grating with 1200 grooves per mm was used, resulting in an effective spectral resolution (apparatus function) of 3 cm⁻¹. For more experimental details see Nasdala and Massonne (2000). Previous Raman measurements had shown that the FWHM of the $\nu_1(\text{PO}_4)$ Raman band, which is used to monitor the degree of short-range order, does not show any significant orientational dependence (Nasdala et al. 1999). Therefore, the polished monazite samples (prepared in microprobe mounts with random crystallographic orientation) were oriented under the Raman microscope to get a high $\nu_1(\text{PO}_4)$ Raman band signal.

- Cathodoluminescence

CL images of monazites were taken using a JEOL JXA 8900 RL electron microprobe. The voltage was set to 20 kV with a beam current of 50 nA. As the absolute CL signal intensity emitted from a sample is most strongly affected by the experimental conditions, samples to be compared were brought simultaneously in the vacuum chamber and were analysed with exactly the same experimental conditions (identical size of scanned area, constant signal amplification, constant exposure time). Although conclusions from the

absolute intensities of the CL emission are widely limited, relative comparison of intensities is possible between images taken of the same analysis run.

3 - Results

3-1 - X-ray diffraction analysis

- Unheated monazite:

The diffraction pattern of unheated monazite (Figure 2a) shows sharp reflections of relatively high amplitudes. For some reflections a broadening at the reflection bases was observed. This broadening seems to be more pronounced along the a-direction, e. g. (200) reflection between $26-28^\circ$ (2θ). A typical diffraction pattern in the range of $26-28^\circ(2\theta)$ of the unheated monazite is given in figure 2b. It shows one characteristic reflection (A) of high amplitude, which is very sharp ($\text{FWHM} = 0.091^\circ$) and additionally a broad ($\text{FWHM} = 0.425^\circ$) shoulder (B) of low amplitude (Table 3). The B-reflection maximum is located at a larger 2θ value of 27.04° (3.295\AA) than the A-reflection maximum, which is located at 26.88° (3.314\AA) (Table 3). The area percentage of A and B reflections are 47.01% and 52.99% respectively (Table 3). Careful examination of the whole diffraction pattern shows that this is a general feature of all reflections.

Rietveld-refinement of the unheated monazite, assuming only a single-phase (A) with a monazite structure, failed. However, introducing a second phase (B) also with monazite structure resulted in a successful Rietveld refinement. Consequently the patterns were interpreted as two monazite phases with different lattice parameters (Table 3). Monazite (A) shows larger lattice parameters (1% in volume) than the reference crystal from Ni et al. (1995). The lattice parameters of monazite (B) are about the same as that of the reference.

- Evolution with temperature:

In order to evaluate the annealing effect on the lattice of monazite, the (200) reflections between 26 and 28° (2θ) of the unheated monazite were compared with those of the monazite heated of 500°C , 800°C and 1000°C (Figure 3). A different evolution of the sharp reflection (A) and the broad reflection (B) was observed. With increasing temperature the A-diffraction maximum shifts from 26.88 (3.314\AA) to 27.00° (3.300\AA) and maximum number of counts increases from 7533 to 11226. Annealing causes a reduction of the lattice

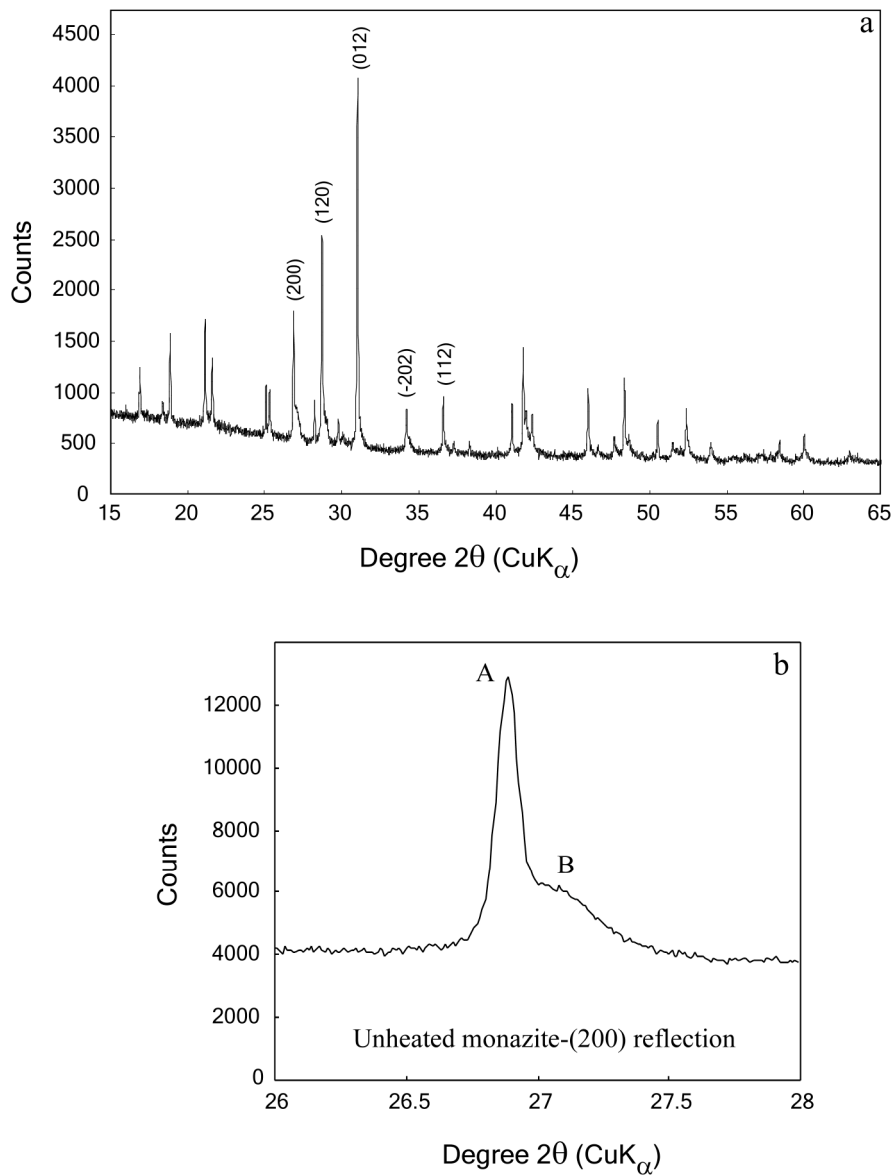


Figure 2:

a: X-ray diffraction pattern of the unheated monazite

Note the broadening of the reflections, indicating a distortion of the monazite lattice.

b: X-ray powder diffraction pattern of the unheated monazite in the range of 26-28° (2θ).

We distinguish two "phases" (A) and (B)

(A) shows a sharp reflection ($\text{FWHM}_{200} = 0.09$) with high amplitude.

(B) exhibits very broad reflection ($\text{FWHM}_{200} = 0.41$) with low amplitude.

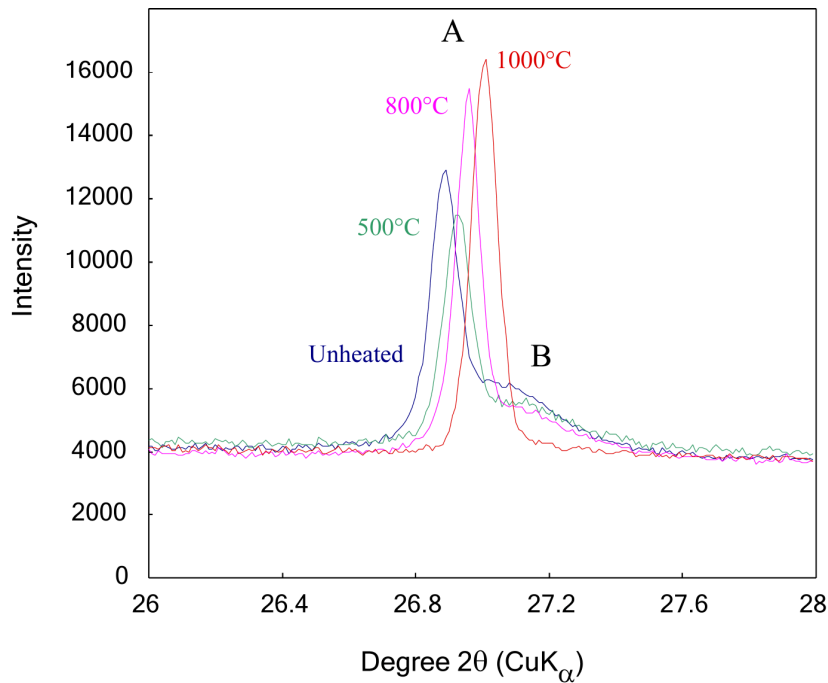


Figure 3:

X-ray powder diffraction patterns in the range of 26-28° (2θ) at different annealing conditions. We observe that the "phase" (B) disappears with increasing temperature and the (A) reflections shift to higher scattering angles.

At 1000°C, X-ray diffractometry shows only one phase.

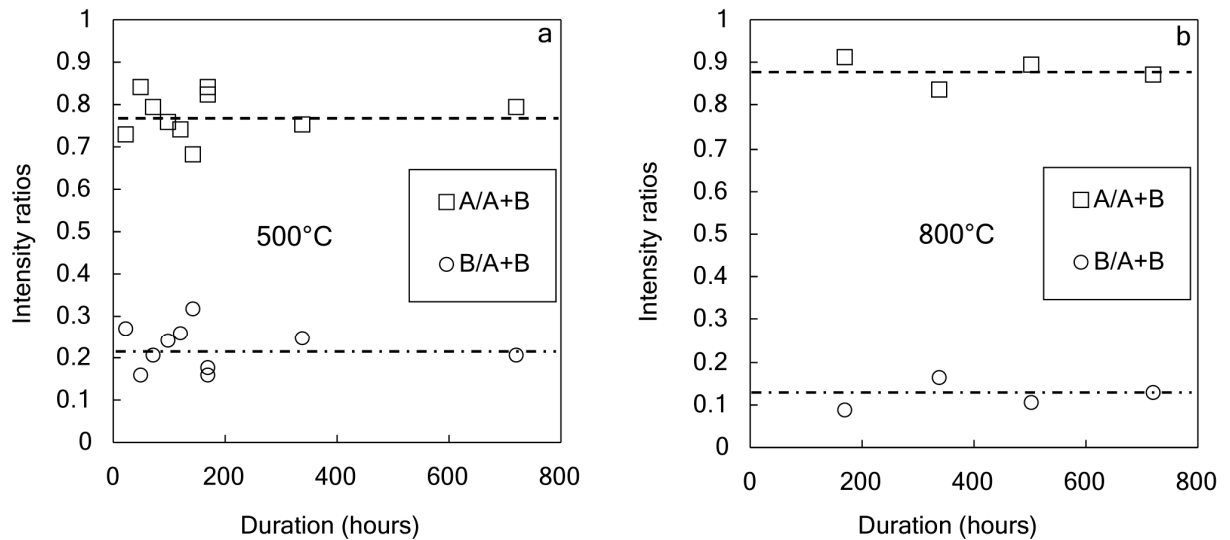


Figure 4:

Evolution of the amplitude ratios of the two phases (A) and (B) as a function of time.

a: at 500°C

b: at 800°C

(A) correspond to the sharp reflections and (B) to the broad reflections.

Table 3 - Unit-cell parameters (Å), FWHM ($^{\circ}2\theta$), amplitude (counts), centre of the maximum diffraction angle (2θ) and % area for the (200) diffraction maximum (phases A and B) for the unheated monazite and for different annealing conditions.

Sample N $^{\circ}$	Moacir 0	Mo500-7d	Mo800-7d	Mo10007d	Moacir 0	Mo500-7d	Mo800-7d
	A				B		
<i>a</i>	6.823(1)	6.813(1)	6.801(1)	6.786(1)	6.783(5)	6.788(7)	6.773(6)
<i>b</i>	7.026(1)	7.019(1)	7.012(1)	7.007(1)	7.014(6)	7.001(7)	6.995(7)
<i>c</i>	6.499(1)	6.484(1)	6.468(1)	6.464(1)	6.489(5)	6.471(6)	6.443(6)
β	103.79(1)	103.73(1)	103.65(1)	103.57(1)	103.69(9)	103.67(10)	103.77(10)
<i>V</i>	302.60(9)	301.22(9)	299.78(6)	298.77(3)	299.98(36)	298.83(42)	296.48(38)
FWHM	0.091(1)	0.093(1)	0.083(1)	0.092(1)	0.425(6)	0.420(14)	0.296(18)
Amplitude	7533	3436	11153	11226	2026	736	1088
Centre	26.88	26.92	26.95	27	27.04(1)	27.08(1)	27.16(1)
% Area	47.01	51.01	75.11	~100	52.99	48.99	24.89

Run duration for all experiments is 7 days. Numbers in brackets correspond to 2σ errors. Moacir 0 corresponds to the unheated monazite.

Table 4 - Amplitude ratios of the (200) reflections of the two phases A and B at 500°C and 800°C as a function of time.

Durations (hours)	500°C		800°C	
	A/A+B	B/A+B	A/A+B	B/A+B
24	0.73	0.27	-	-
48	0.84	0.16	-	-
72	0.80	0.20	-	-
96	0.76	0.24	-	-
120	0.74	0.26	-	-
144	0.68	0.32	-	-
168	0.82	0.18	0.91	0.09
336	0.75	0.25	0.84	0.16
504	-	-	0.90	0.10
720	0.79	0.21	0.87	0.13

Table 5 - Spectral parameters of the $\nu_1(\text{PO}_4)$ Raman band

Sample	Annealing temperature	Annealing pressure	Band position (cm^{-1})	Measured FWHM $^{-1}$	Corrected FWHM* $^{-1}$
untreated	-	-	972.2	15.6 ± 1.0	15.0 ± 1.0
VRM97-1	500	1	972.5	13.3 ± 1.0	12.6 ± 1.0
VRM97-2	800	2	974.3	7.2 ± 0.7	5.8 ± 0.7
VRM97-4	900	1	974.4	7.1 ± 0.7	5.7 ± 0.7
VRM98-1	900	7	974.3	7.4 ± 0.7	6.1 ± 0.7
VRM97-10	1000	7	974.4	7.3 ± 0.7	5.9 ± 0.7
VRM97-8	1100	7	974.4	7.3 ± 0.7	5.9 ± 0.7
VRM97-6	1200	7	974.4	7.3 ± 0.7	5.9 ± 0.7

* Measured FWHMs were corrected for the apparatus function (here 3 cm^{-1}) and real FWHMs were calculated according to Irmer (1985).

parameters of monazite (A) (Table 3). However the FWHM of (A) remains small and constant ($\approx 0.09^\circ$). At 1000°C , the A-lattice parameters approach those of the reference from Ni et al. (1995).

With increasing temperature the B diffraction maximum decreases in amplitude and disappears completely at 1000°C .

- Evolution with time:

Figure 4 shows the evolution of the amplitude ratios of A and B reflections at 500°C and at 800°C as a function of time (ratios are given in Table 4). Significant variations of the $A/(A+B)$ and $B/(A+B)$ amplitude ratios were not observed, neither at 500°C nor at 800°C as a function of time. At 500°C the $A/(A+B)$ ratio is about 0.8 and the $B/(A+B)$ ratio is 0.2 whereas at 800°C the $A/(A+B)$ ratio is about 0.9 and the $B/(A+B)$ ratio is 0.1 (Figure 4). The ratio $B/(A+B)$ decreases with increasing temperature but remains constant during 30 days.

3-2 - Selected Area Diffraction and HRTEM observations

SAD patterns of the unheated monazite (Figure 5a) always show sharp reflections. No differences between these SAD patterns and the SAD patterns of the sample heated at 900°C were observed. However, HRTEM image of the unheated monazite revealed isolated areas (5 nm) where the lattice fringes were blurred or absent (Figure 5a). The distorted areas pose strain on the lattice in the vicinity, which causes inhomogeneous contrast distribution close to the distorted areas (Figure 5a). These distorted domains completely disappeared at 900°C : HRTEM images of this monazite showed undistorted lattice fringes and homogeneous contrast (Figure 5b).

3-3 - Dark Field images

Dark field (DF) images of the unheated monazite (Figure 6a) show mottled diffraction contrast as a result of a mosaic structure of the crystal. The slightly different oriented domains, which represent coherent scattering volumes with slightly varying orientations, are quite homogeneously distributed in the monazite. The bright areas, e. g. figure 6a, represent small coherent scattering volumes, which have no or only a small deviation from the exact Bragg position. At 500°C these domains were still observed. However, the coherent scattering volumes became larger (Figure 6b). At 800°C , only small amounts of the distorted domains remained (Figure 6c) and they are no longer observed at 900°C (Figure 6d).

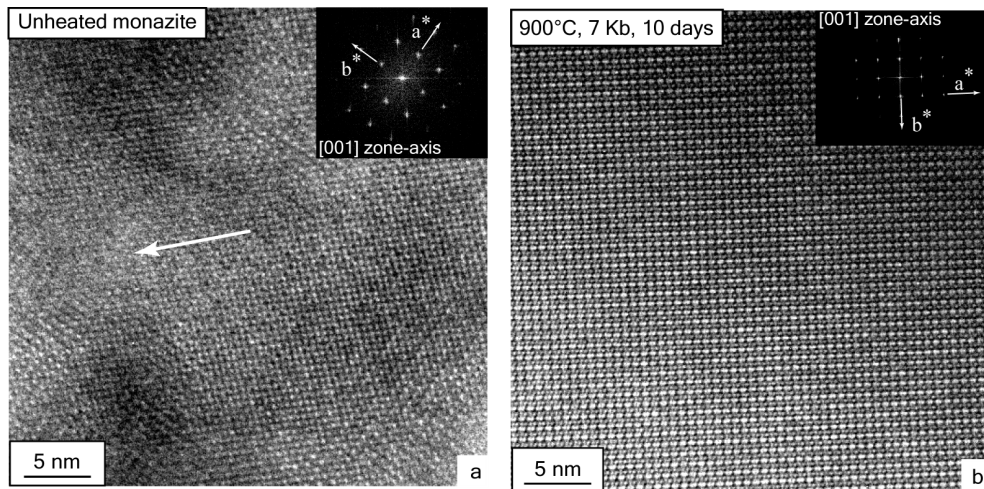


Figure 5:

- a)** Energy filtered HRTEM image and corresponding diffraction pattern (Fast Fourier Transform) of the unheated monazite. Note the presence of distorted domains (arrow).
- b)** Energy filtered HRTEM image and corresponding diffraction pattern (FFT) of the monazite heated at 900°C, 7 Kb, 10 days (VRM98-1). The lattice fringes are not distorted.

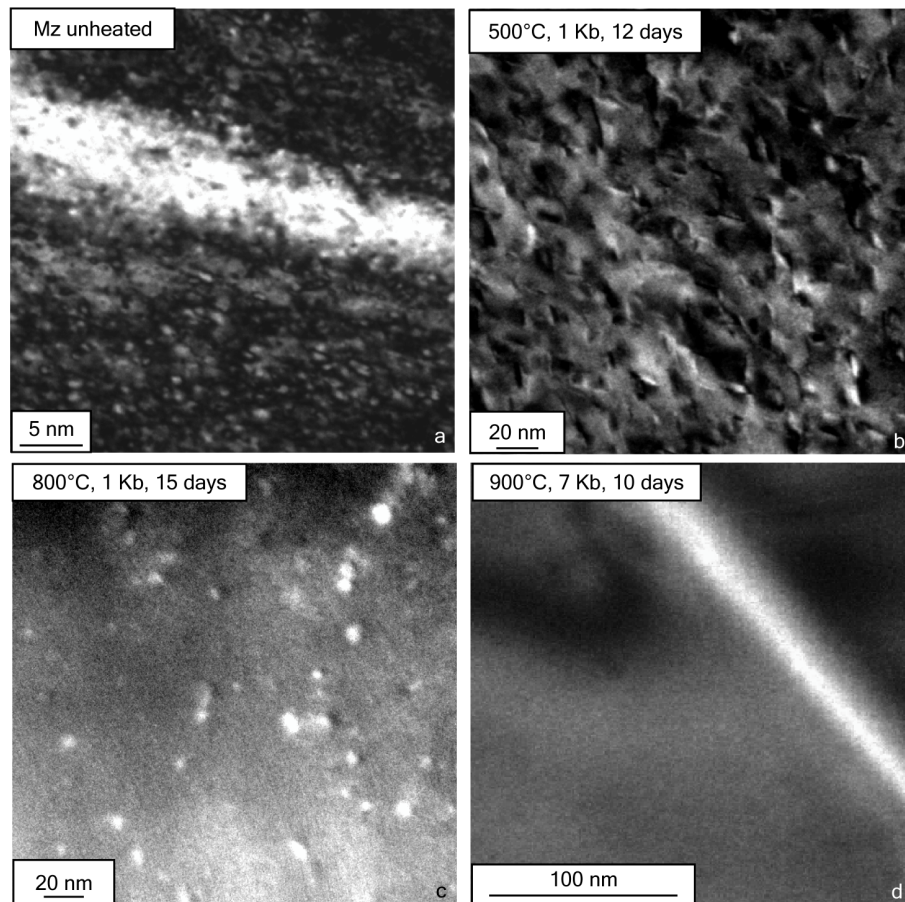


Figure 6: TEM dark field images (DF)

- a)** Unheated monazite. Mottled diffraction contrast is due to the presence of distorted areas. Their distribution is quite homogeneous in the grain.
- b)** Monazite heated at 500°C, 1 Kb, 12 days (VRM97-1). Mottled diffraction contrasts are still present. However the coherent scattering volumes became larger.
- c)** Monazite heated at 800°C, 1 Kb, 15 days (VRM97-2). Only a small amount of the distorted domains remained.
- d)** Monazite heated at 900°C, 7 Kb, 10 days (VRM98-1). No more distorted areas are visible.

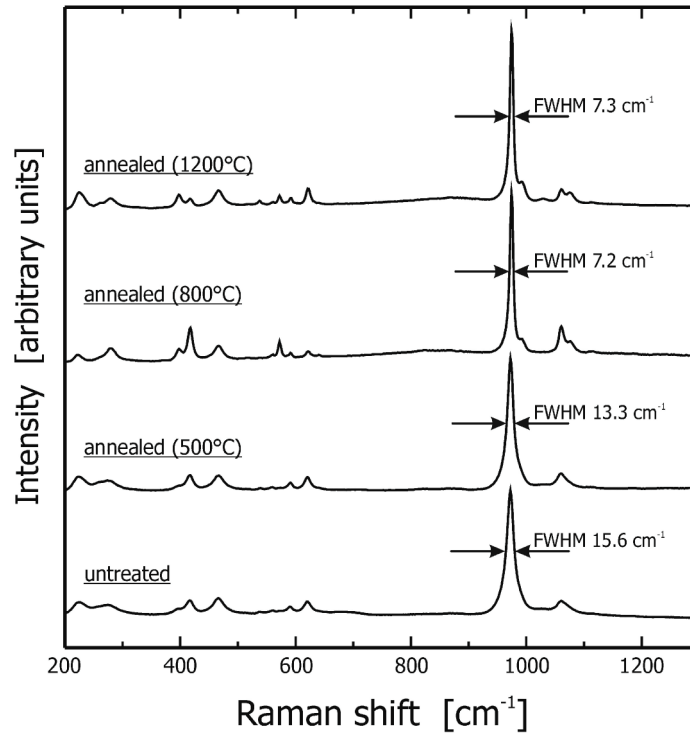


Figure 7: Raman spectra of the untreated monazite in comparison with spectra of annealed samples. Note the decreasing width of the $\nu_1(\text{PO}_4)$ band (the intense peak at $\sim 972\text{-}974 \text{ cm}^{-1}$). Measured FWHMs are given.

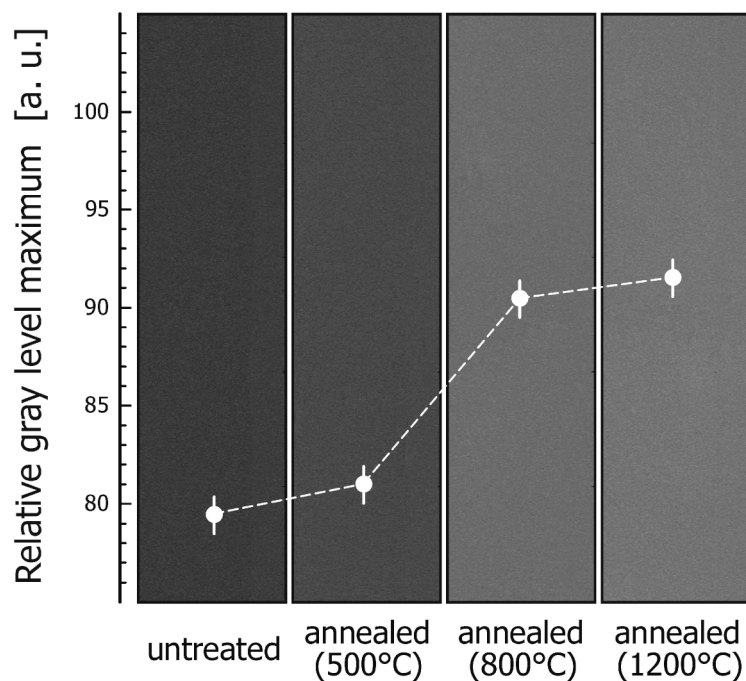


Figure 8: CL images of the same four samples as in figure 7. The relative intensity of the area-integrated CL signal was measured on a random greyscale (0 = black; 256 = white). The values at the ordinate axis represent the maximums of the respective grayscale distribution patterns.

Line scan of a certain volume of monazite did not show any detectable change in chemical composition.

3-4 - Raman measurements

The Raman spectra of monazites annealed at high temperature (Figure 7) show clearly narrower bands than the spectrum of untreated monazite, which shows however only moderate band broadening. Monazite annealed at 500 °C shows only moderately decreased Raman band broadening. Raman spectral parameters obtained from samples annealed between 800 and 1200 °C are identical within their errors (Table 5). At 800 °C, the recovery of the short-range order was almost as complete as after annealing at 1200 °C.

3-5 - Cathodoluminescence

The CL results are only briefly documented here and will be described in more detail elsewhere. CL images of monazites were taken from areas 30 × 120 μm in size. Four sample images are presented in figure 8. We did not observe notable inhomogeneities, which confirms the statement above that the studied monazite is chemically homogeneous at a micro-scale. Series of images were obtained in order to check potential changes of the relative CL signal intensity with annealing. In figure 8 it can be seen that annealed monazites emit more intense CL than the untreated sample. Corresponding with the other analytical results, most changes are observed between 500 and 800°C whereas above 800°C intensity variations are insignificant.

4 - Discussion

4-1 - Interpretation of the results

X-Ray diffraction patterns of the unheated monazite show the coexistence of two diffraction domains (A) and (B), which can be interpreted as two monazite phases with slightly different lattice parameters and different crystallinity (Table 3). The first one (A) shows sharp reflections of high amplitudes (Figure 2b). This means that (A) corresponds to a well-ordered, well-crystallised monazite with larger unit-cell volume (302.60 Å³). The second diffraction domains (B) show broad reflections of low amplitudes, 3.5 times lower than (A) (Table 3). Diffraction domain (B) is interpreted as a distorted monazite crystal lattice composed of “islands” with an expanded lattice, induced by presence of interstitials, and

“islands” of a compressed monazite lattice, induced by presence of vacancies. These vacancies and interstitials (Frenkel pairs) have resulted from α -recoil damage. The recoiled heavy nucleus knocks atoms from its lattice position into an interstitial position. The interstitials induce an expansion of the unit-cell volume of adjacent crystalline areas. The removed atoms create vacancies causing slight relaxations of the lattice (Figure 9b). Both the “islands” of expanded and contracted lattice will pose stress on the lattice vicinity, which is visible in the HRTEM images (Figure 5a) and accounts for the decreased short-range order causing Raman band broadening. The broadening (XRD) of the B-reflection, with its centre at the position of the reference reflection from Ni et al. (1995), is due to the expanded or compressed diffraction domains and additional small particle size. Furthermore, expansion of the A-domains will exert stress on the (B) domains too. The similar area percentages of the two domains show that the volume fraction of (A) in monazite seems to be the same as for (B). The expansion of the A-monazite lattice is discussed below, because it could be due to several mechanisms like differences in chemical composition compared with the B-monazite, disordering of atoms in the lattice, i.e. presence of defects in the A-monazite, or incorporation of He in the lattice.

TEM images (HRTEM and DF) support also the idea of the presence of two domains: nm-sized domains with blurred lattice fringes and well-crystallised domains (Figure 5a). According to the XRD results, we refer the (A) phase to these crystallised domains and the (B) phase to the distorted nm-sized domains. Consequently, the unheated monazite is a mosaic crystal composed of well-crystallised domains (A) and nm-sized distorted regions (B).

With increasing annealing temperature XRD-patterns exhibited a lower amplitude of the broad reflections (B) (Figure 3 and Table 3). This is also supported by TEM images (DF) with a gradual coarsening of the mosaic structure (Figures 6b and c). We interpret this as a progressive healing of defects in distorted domains (B) with increasing temperature. On the contrary, the FWHM of (A) reflections remain constant and narrow with increasing temperature, suggesting that (A)-domains in the unheated monazite were already well crystallised (Table 3). The complete absence of the broad reflections in the XRD pattern at 1000°C, correlates with the absence of the distorted domains in the HRTEM image (Figure 5b) and a homogeneous diffraction contrast on the DF image (Figure 6d). At 900°C the presence of a well-crystallised monazite lattice indicates complete healing of the structural radiation damage.

Raman spectroscopy was introduced by Nasdala et al. (1995) as a method to estimate the degree of metamictisation. These authors found that the gradually decreasing short-range order in metamict zircons causes increasingly broadening of Raman bands, accompanied by frequency shifts towards lower wavenumbers due to the general widening of bond lengths. In the case of monazites, however, decreased short-range order and, with that, Raman band broadening as well as shifted peak positions, can be due to both structural (radiation damage) and chemical causes (e.g., local lattice distortion due to uneven cation occupation). For instance, Podor (1995) has demonstrated that Raman spectra of synthetic REE phosphates show systematic band broadening and peak shifts with increasing actinide content. Correspondingly, Nasdala et al. (1999) obtained significantly broadened Raman spectra from natural monazites that were, in spite of Th contents exceeding 10 wt-% and self-irradiation doses exceeding 5×10^{16} α /mg, well crystalline. Therefore, quantitative estimation of the degree of radiation damage from the Raman spectra alone is limited. It is, however, possible to analyse the spectra obtained from our chemically identical samples in view of potentially different contributions of their different degrees of radiation damage to the Raman spectral parameters. Observations in figure 7 suggest that a major portion of the initial Raman band broadening is caused by radiation damage. The greatly enhanced short-range order of the heat-treated samples points clearly to the structural recovery through annealing. This is also consistent with the observed moderate band shifts towards higher wavenumbers (Table 5; c. p. discussion on zircon by Nasdala et al. 1995). Furthermore, the observations suggest that most of the healing of the initially metamict structure must have occurred between 500 and 800°C. This is in agreement with the results given by the other methods.

Although quantitative conclusions are widely limited at the present stage, the comparison of the obtained spectra (Figure 7) with the Raman band broadening of other radiation-damaged minerals such as zircon (Nasdala et al. 1995) and biotite (Nasdala et al. 2001a) suggests that the untreated monazite sample represents only intermediate metamictization. This is consistent with the TEM observations above. Considering that minerals are fully amorphised after accumulating about 0.3 – 0.5 dpa (e.g., Weber et al. 1991), it is clear that the studied monazite (self-irradiation dose ≈ 2 displacements per atom (dpa)) cannot have accumulated the complete radiation damage since the time of its growth 474 Ma ago. In contrast, only a small portion of the damage is stored whereas most of the radiation damage must have been annealed. The major annealing of the radiation damage has, however, not affected the concordant U-Th-Pb isotope system of the monazite. The common

radiation damage annealing without significant Pb loss has been documented by Nasdala et al (2001b) for zircons from Sri Lanka and other localities.

The results using the CL confirm first, that monazites are poor CL emitters, when compared with zircon. The recorded CL intensity was generally low and high signal amplification was needed to produce greyscale images. Thus, CL emission of natural minerals is not only determined by their chemical composition but is also affected by structural parameters, in our case the degree of radiation damage.

In the following the small A-lattice parameters, the shift of reflection (A) towards larger scattering angles and the decrease in amplitude of the B-reflection with increasing annealing temperature is discussed.

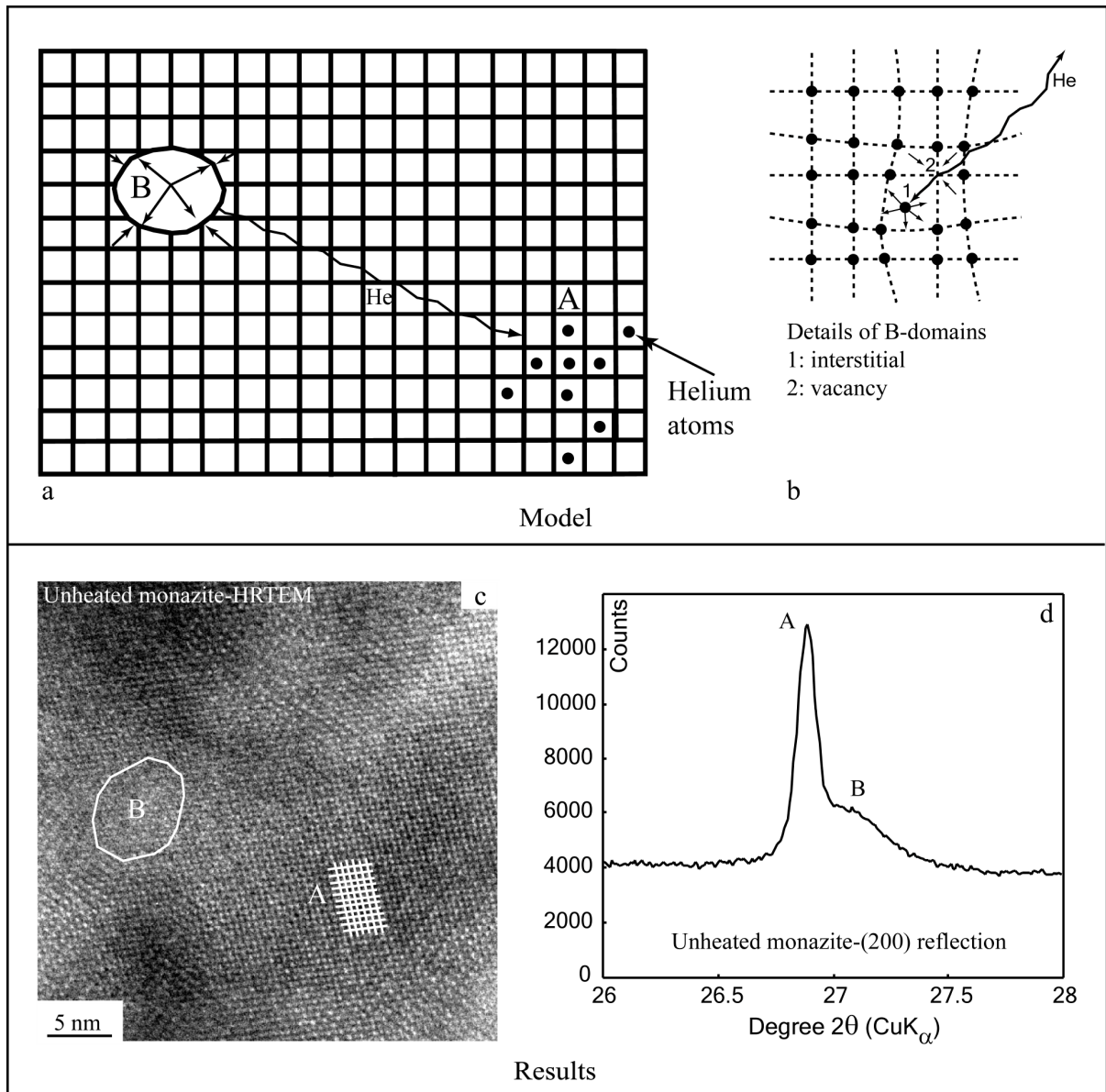
Chemical heterogeneities

The unit cell of monazite depends on its composition. Monazite is a complex solid solution, and the unit-cell volume of the major end member are 296.23 \AA^3 (huttonite), 289.47 \AA^3 (brabantite), 292.95 \AA^3 (Nd), 305.69 \AA^3 (La), 299.49 \AA^3 (Ce), but can be as low as 279.08 \AA^3 (Gd) (Devidal and Montel 1999). Consequently, two coexisting monazites with different chemical compositions would have different unit-cell parameters. If a different chemical composition would be the origin of the peak shift, we should expect a progressive homogenisation of the crystal with increasing temperature.

A volume increase of the A-monazite due to different chemical compositions is rejected, because monazite is very homogeneous on a nm-scale. If there is any chemical heterogeneity in the crystal, it must be beyond the detection and resolution limit of TEM, which is unlikely. Another argument against this hypothesis is that such a lattice expansion was recently also reported for monazite (Smith and Giletti 1997), for zircon (Holland and Gottfried 1955; Murakami et al. 1991) and for pyrochlore (Lumpkin and Ewing 1988). The lattice expansion might be a more general problem related to the amorphization/annealing process.

Presence of Frenkel defects

We interpret the distorted (B) domains as old alpha-recoil tracks. These isolated "islands" are expanded or can be compressed, and consequently compress or expand the adjacent crystalline regions of the sample (Lumpkin and Ewing 1988; Salje et al. 1999).

**Figure 9:**

Model describing the (A) and (B) domains (a and b). The results from HRTEM and XRD from the unheated monazite are given in c and d. During an α -event a heavy atom nucleus liberates its energy in ejecting an α -particle. The remaining nucleus recoils in an opposite direction from the α -particle. This recoil creates Frenkel pairs, i.e. interstitial atom (1) and vacancy (2), which exert stress on the lattice in the vicinity (see b). These distorted domains correspond to the domains (B). They are interpreted as a He-free distorted monazite crystal lattice, which can be referred to old α -recoil tracks, and is composed of "islands" with an expanded lattice, induced by presence of interstitials (1), and "islands" of a compressed monazite lattice, induced by presence of vacancies (2). Both the "islands" will pose stress on the lattice in the vicinity (see b). The broadening of the (B)-reflection is due to the expanded or compressed diffraction domains and due to the different amount of the distortion (see d). He accumulates in the crystalline regions (A) (see a and c) and induces an expansion of the unit-cell volume (see d). During the heating, domains (B) are healed, then progressively disappear. He diffuses out of the monazite lattice, inducing a relaxation of the lattice of the regions (A). At 900 C, healing of the lattice is completed.

Expansion of (A) results in a compressive stress on (B). However, the scattering volumes referred to the A-reflections (Table 3) show a well-crystallised lattice with a volume increase of 1% compared with monazite, which was annealed at 1000°C. The expansion has been explained previously with the presence of Frenkel defects (Murakami et al. 1986; 1991; Weber et al. 1998). Such point defects cannot be resolved by HRTEM and XRD, which is also demonstrated in a recent study by Nasdala et al. (2001a).

With increasing temperature Frenkel defects are healed, i.e. interstitial cations diffuse into the vacant sites, resulting in a relaxation of the lattice and a shift of the A-reflections to smaller d_{hkl} values. Alpha-recoil-tracks are healed and consequently the B-domains disappear.

However, with increasing temperature the FWHM of (A) remains constant. Healing of point defects should have resulted in a reduction of the FWHM, which is not observed. This suggests that either the effect of the interstitial atoms ordering in the lattice is not significant enough so that we observe a decrease of the A-FWHM with increasing temperature, or that this hypothesis is not correct. Furthermore, interstitials in the (A)-lattice will induce an expansion of the lattice, which can be compensated by vacancies. This would be in contradiction to the observed increase of the lattice parameters.

Presence of He (Figure 9)

We calculated that the studied monazite has experienced about 2.43×10^{16} alpha decay-events per mg since its growth 474 Ma ago. Ultimately those particles will become He atoms. We have calculated that each gram of the monazite produced 0.17 mg of He. Direct measurements of the He content in this monazite are in agreement with this calculation, and lead to U/Th-He age of 430 Ma (Pik, Personal Communication). This means that since 474 Ma nearly all the He has been stored in the monazite lattice. The accumulation of such a large amount of He in the monazite lattice should expand the monazite lattice (Weber et al. 1998).

It seems to be unlikely that He is accumulated in the distorted lattice domains, corresponding to the broad (B) reflections. He cannot accumulate in those areas because the crystal lattice is distorted, unable to trap atoms. Furthermore, during an alpha-decay event He is ejected far away (10-30 μm) in the opposite direction as the alpha-recoil-atom (10-20 nm), i.e. far from the old alpha-recoil-tracks-(B) domains.

The sharp reflections (A) correspond to the well-crystallised areas where He atoms are homogeneously distributed, thus inducing an expansion of the monazite lattice. Homogeneously distributed He in these domains will not modify the periodicity of the unit-

cell, i.e. not modify the FWHM of monazite ($=0.09^\circ(2\theta)$), which is in agreement with our results.

During heating, the alpha-recoil-tracks are healed, then disappear progressively. Simultaneously to the healing of the alpha recoil tracks with annealing, He diffuses out of the monazite lattice, inducing a relaxation of the lattice. This results in a decrease of the unit-cell volume, i.e. A-reflections shift to higher 2θ values (smaller d_{hkl} values) but the FWHM of (A) remains constant. Erichsen (1951) has demonstrated that at 600°C , 6 days, only about 50% of the total He of the monazite is lost. This is in agreement with our results, which still showed an expansion of domains (A) at 500°C .

A rough estimate of the accumulated He in monazite can be done using a very simple solid sphere model: 2.5×10^{16} He /mg is about 0.01 mole He in 1 mole of monazite. The volume occupied by atoms in 1 mole of monazite, calculated from the composition given in Table 1, is 30.71 cm^3 . The volume of 0.01 mole of He atoms (atomic radius 1.28 \AA) is then 0.053 cm^3 . The increase in volume of atom due to the presence of He is about 0.2%. The observed relative variation in volume change of the unit cell during the annealing process is 1%, which is 5 times more than calculated. The discrepancy is not large considering two arguments. First, in this model, all the He atoms are assumed to be accumulated only in the volume fraction represented by the sharp-reflections (A). Consequently, the amount of He in the undistorted lattice volume is larger. Second, the method we used to estimate the effect of He on the monazite structure is very crude because it takes in account only volumes, and not geometry. Therefore we conclude that as far as volume is concerned, the He accumulation may explain the order of magnitude of expansion observed in undistorted regions (A).

Concerning the kinetic of the annealing process, we conclude that after 24 hours and even at 800°C it is too slow to show significant change of the A/B amplitude ratios (Figure 4 and Table 4) within experimental conditions (here 1 month). This is in agreement with the slow rate of cation diffusion in monazite (Smith and Giletti 1997; Suzuki et al. 1994; Montel and Seydoux 1998). However, Erichsen (1951) demonstrates that the He is leaving the monazite within the first 10-20 hours; then, they observed a “steady state”. We suggest that, during the 10-20 first hours He diffuses faster out of the crystal due to the radiation damage in domains (B). In the same time there is a rearrangement of the atoms by diffusion in these domains. This diffusion will be relatively fast if the vacancies and the interstitials are not so far from each other. However, there is a moment where the atoms are too far away and where

the diffusion will be too slow (after 20 hours). This might explain why the A/A+B or B/A+B ratios are quite constant (Figure 4). Thus, He diffusion becomes too slow and He is trapped in the monazite lattice.

4-2 - Comparison with previous studies

In the introduction, we mentioned some contradictions in the literature concerning the annealing temperature of monazite. Two different temperature ranges are proposed: between 300 (Karioris et al. 1981) and 450°C (Meldrum et al. 1998) and between 1100°C (Smith and Giletti 1997) and 900°C (this study). The first difference, between 300 and 450°C, is attributed to the different methods used to characterise the process of annealing. Karioris et al. 1981 only used XRD, whereas Meldrum et al. (1998) used HRTEM. However, using only XRD it is more difficult to exactly determine if a structure is completely healed or if it still contains some defects (cf. this study). The difference between our study and that of Smith and Giletti (1997) is explained by the same argument.

Considering the difference between 450°C (Meldrum et al. 1998) and 900°C (this study) we would argue that the starting material was different for these studies. A completely metamict monazite, amorphised by 800 KeV Kr⁺ ions, was used by Meldrum et al. (1998), and a crystalline monazite with a small amount of defects in the study presented here. The differences in temperature may be due to the type of healing process: epitaxial recrystallization vs. diffusion. Epitaxial recrystallization starts immediately after the beginning of nucleation (not observed in our study). We observed that the diffusion rate is very slow and healing of defects by diffusion needs higher temperature to be more efficient. Metamict monazite begins to recrystallise at about 450°C. The lattice defects of crystalline monazite, which contains isolated distorted domains due to irradiation damage, are healed at about 900°C. This observation seems to concur very well with recent results of Nasdala et al. (2001b) who found that isolated Frenkel pairs are a comparably stable type of radiation damage whereas more radiation-damaged clusters are more easily annealed.

Furthermore, it is important to note that these studies treat annealing without considering the competing amorphization process. In nature there is always competition between these two processes. Many studies illustrate that monazite already healed at 200°C (Meldrum et al. 1996; 1997; 1998; 2000...).

4-3 - Differences between monazite and zircon

The reflection broadening in XRD-patterns mentioned above was already observed in the Harriman monazite by Smith and Giletti (1997) (Figure 6 page 1052). However the resolution of their diffractometer was not sufficient to clearly separate the two reflections and therefore, the authors did not interpret the diffraction pattern. Nevertheless, it is obvious that the raw monazite (200) reflection is composed of two reflections: a sharp one on the left and a broad one on the right. The broad reflection decreases with increasing temperature and totally disappears at the annealing at 1100°C, just like in our study.

Murakami et al. (1991) investigated irradiation damage in zircon. They presented results of a study of a suite of natural zircon samples from Sri Lanka that span a range of doses over which the transition from the crystalline to amorphous metamict state occurred. They defined three different stages of damage accumulation (Figure 17 page 1527 in article). We did not observe the complete range of these stages in our study. Our starting monazite is equivalent to Murakami's Ib stage, which corresponds to a crystalline monazite with nm-sized distorted domains. Murakami et al. (1986) and (1991) described their XRD (200) pattern in stage Ib as an asymmetric reflection resulting from a combination of a Bragg diffraction maximum and a diffuse scattering component (Figure 2 page 749 in Murakami et al. 1986). We supposed that this asymmetry is visible, only because they used a low-resolution diffractometer. The Bragg diffraction component may correspond to the reflection (A) in our study and the diffuse scattering component may be referred to the reflection (B). The authors report that the symmetric Bragg diffraction maximum shifts to smaller values of 2θ with increasing dose (increasing unit-cell volume), which is in agreement with our observations. The diffuse scattering component in the diffraction pattern is assigned to interstitial defects. This explanation seems not to be appropriate, because the presence of defects should increase the lattice volume, i.e. a diffuse scattering component should be located at smaller scattering angles. We suggest to explain the diffuse scattering component in terms of the reflection (B) observed in our study.

4-4 - Applications for geochronology

Presently, two processes are proposed to explain the resetting of an isotopic system in monazite: loss of Pb by volume diffusion out of the monazite grain or dissolution by a coexisting fluid and precipitation of a newly formed monazite.

Pb diffusion in monazite is known to be very slow (Suzuki et al. 1994; Smith and Giletti 1997). However radiation damages can increase the rate of diffusion, because these defects

provide channels for the diffusion. Resetting of monazite depends on the behaviour of its crystal lattice with temperature. If the monazite lattice is destroyed by irradiation, Pb can be lost by diffusion through these channels, i.e. interface between crystalline and amorphous domains. If the monazite lattice is pristine, Pb diffusion will be not an efficient mechanism for resetting, because of the slow rate of Pb diffusion in monazite; resetting occurs by a dissolution-precipitation process.

It is generally observed in nature that monazite is very often well crystalline, because irradiation damage is rapidly healed at low temperature. This means that, in geologic samples, Pb diffusion occurs predominantly within a pristine, organised crystal structure. To conclude, discordant U-Pb ages obtained for monazite mainly result from resetting by dissolution-precipitation.

Cherniak (1993) studied the Pb diffusion in titanite. She demonstrated that metamict titanite is much less retentive for Pb and that Pb isotope ratios should rarely be preserved in this structure. The author calculated the closure temperatures, i.e. the temperature at which the daughter nuclide begins to accumulate in the structure, for metamict and crystalline titanite. A titanite crystal (0.005 cm-diameter) will still retain Pb isotope information when heated at 600°C for several million years. In contrast, a metamict titanite of the same size will retain Pb only when heated at a temperature < 200°C, for several million years. All these results show that closure temperature for minerals should be used carefully. We cannot explain an age discordance by simply using the closure temperature of a mineral, because it depends much on the lattice of the mineral, metamict or crystalline. This might explain the reported differences in closure temperature of monazite between 720-750°C (Copeland et al. 1988) and $530 \pm 25^\circ\text{C}$ (Black et al. 1984).

4-5 - Implications for nuclear waste

Monazite is studied in order to check its ability to incorporate large amount of actinides and to investigate its resistance to dissolution and irradiation damage. The aim is to find crystalline ceramics with a monazite-like structure as a container for high-level nuclear waste (Boatner et al. 1980; 1981; Boatner and Sales 1988).

Our study shows that although old (474 Ma), radioactive (1300 ppm of U and 69000 ppm of Th) and containing small amounts of nanometer scale irradiation damages, our monazite is not metamict, because of its ability to repair damage domains at relatively low temperature. Irradiation experiments show that monazite cannot be amorphised at temperatures exceeding 200°C (Meldrum et al. 1997; 1998). That means that radiation

damages cannot accumulate in monazite because during annealing the defects are healed faster than the lattice is damaged. Therefore it can be speculated that nuclear waste in a monazite-like matrix will remain in crystalline state during all the storage time.

5 - Conclusions

It is concluded that the investigated Brazilian monazite is like a mosaic crystal. The mosaic consists of two domains (A) and (B), which are basically two monazite crystals with slightly different lattice parameters. Diffraction domains (A) show sharp reflections with high amplitude. They are assigned to a well-crystallised lattice with small volume expansion (1%). Diffraction domains (B) exhibit very broad reflections with low amplitude and represent a distorted lattice, which can be referred to old alpha-recoil tracks. We calculated that about 2.5×10^{16} α /mg have been accumulated in this monazite since 474 Ma. It is suggested that the (A) domains correspond to well-crystallised areas where He atoms are trapped. The trapped He causes an expansion of the monazite lattice (A). Consequently the A-reflections are shifted to smaller scattering angles 2θ . Diffraction domains (B) are interpreted as a distorted monazite crystal lattice composed of “islands” with an expanded lattice (interstitials), and “islands” of a compressed monazite lattice, (vacancies). Both the “islands” will pose stress (compression and/or dilatation) on the lattice in the vicinity. The broadening of the B-reflections is due to the expanded/compressed diffraction domains and due to the different amount of the distortion. Therefore, in the (B) domains, He cannot accumulate because the crystal net is very poor, unable to trap atoms.

During annealing, the alpha-recoil-tracks are healed, and the diffraction domains (B) progressively disappear. At the same time, He diffuses out of the monazite lattice, inducing a relaxation of the lattice (volume decrease). The (A) reflections are shifted to larger scattering angles (smaller d_{hkl} -values). At 900°C only one phase remains that is a monazite with well-crystallised lattice and minimum unit cell volume.

Why is monazite never metamict? Although it is obvious that monazite is able to heal its structure at low temperature (100-200°C), it is not sure that this low temperature annealing is the only effect. It is surprising that during annealing nearly all the He remains accumulated in the monazite lattice. It is also possible to consider an ionisation-annealing induced by He-ion irradiation, a phenomenon observed in apatite (Ouchani et al. 1997). This is in agreement with the assumption that the well-crystallised domains correspond to the He-rich domains.

Acknowledgements:

We would like to thank very much Moacyr Marinho who kindly provide us the monazite sample. We thanks I. Bauer for providing the XRD analyses and E.M. Schemmert and K. Paech for the preparation of the TEM samples. We are grateful to A. Kronz (Göttingen) for taking the CL images. A. Beran and E. Libowitzky (Wien) kindly made a Raman system available for analysis. Thanks to R. Pik (CRPG-Nancy, France) for its personal communication concerning the U/Th-He age of our monazite.

References

- Black LP, Fitzgerald JD, Harley SL (1984) Pb isotopic composition, colour, and microstructure of monazites from a polymetamorphic rock in Antarctica. *Contrib Mineral Petrol* 85: 141-148
- Boatner LA, Beall GW, Abraham MM, Finch CB, Huray PG, Rappaz M (1980) Monazite and other lanthanide orthophosphates as alternative actinide waste forms. In: *Scientific Basis for Nuclear Waste Management*, Northrup Jr CJM (ed) 2: 289-296 Plenum Press New York
- Boatner LA, Abraham MM, Rappaz M (1981) The characterization of nuclear waste forms by EPR spectroscopy. In: *Scientific Basis for Nuclear Waste Management*, Moore JG (ed) 3: 181-188 Plenum Press New York
- Boatner LA, Sales BC (1988) Monazite. In: *Radioactive Waste Forms for the Future*. Lutze W, Ewing RC (ed) 495-564 Elsevier
- Cherniak DJ, Lanford WA, Ryerson FJ (1991) Lead diffusion in apatite and zircon using ion implantation and Rutherford back-scattering techniques. *Geochim Cosmochim Acta* 55: 1663-1673
- Cherniak DJ (1993) Lead diffusion in titanite and preliminary results on the effect of radiation damage on Pb transport. *Chem Geol* 110: 177-194

- Copeland P, Parrish RR (1988) Identification of inherited radiogenic Pb in monazite and its implications for U-Pb systematics. *Nature* 333: 760-763
- Corfu F (1988) Differential response of U-Pb systems in coexisting accessory minerals, Winnipeg River Subprovince, Canadian Shield: implications for Archean crustal growth and stabilization. *Contrib Mineral Petrol* 98: 312-325
- Cruz MJ, Cunha JC, Merlet C, Sabaté P (1996) Datação pontual das monazitas da região de Itambé, Bahia, através da microsonda eletrônica. XXXIX Congresso Brasileiro de Geologia
- Devidal JL, Montel JM (1999) Crystal chemistry of the brabantite-monazite group. *EUG 10 J Conf Abstract*, 4, 524.
- Dodson MH (1973) Closure temperature in cooling geochronological and petrological systems. *Contrib Mineral Petrol* 40: 257-259
- Ericksen LV (1951) Über die Heliumabgabe von Monazit in abhängigkeit von Gasphase, Druck und Temperatur. *N Jahrbuch F Mineralogie. Monatshefte*: 25-33
- Ewing RC (1975) The crystal chemistry of complex niobium and tantalum oxides IV The metamict state: Discussion. *Am Mineral* 60: 728-733
- Ewing RC, Chakoumakos BC, Lumpkin GR, Murakami T, Gregor RB, Lytle FW (1988) Metamict minerals: natural analogues for radiation damage effects in ceramic nuclear waste forms. *Nucl Instr Meth B32*: 487-497
- Ewing RC, Weber WJ, Clinard FW Jr (1995) Radiation effects in nuclear waste forms. *Progress Nucl Energy* 29: 63-127
- Ewing RC, Meldrum A, Wang LM, Wang SX (2000) Radiation-Induced Amorphization. In: *Reviews in Mineralogy and Geochemistry*, Ribbe PH (ed) 39: 319-361 Mineralogical Society of America, Washington DC

- Firestone RB, Shirley VS (1996) Table of isotopes 2. John Wiley & Sons Inc, C5-C6
- Förster HJ (1998) The chemical composition of REE-Y-Th-U-rich accessory minerals in peraluminous granites of the Erzgebirge-Fichtelgebirge region, Germany, Part I: The monazite-(Ce)-brabantite solid solution series. *Am Mineral* 83: 259-272
- Gögen K, Wagner GA (2000) Alpha-recoil track dating of Quaternary volcanics. *Chem Geol* 166: 127-137
- Holland HD, Gottfried D (1955) The effect of nuclear radiation on the structure of zircon. *Acta Crystallogr* 8: 291-300
- Irmer G (1985) Zum Einfluß der Apparatefunktion auf die Bestimmung von Streuquerschnitten und Lebensdauern aus optischen Phononenspektren. *Exper Techn Phys* 33: 501-506
- Karioris FG, Appaji Gowda K, Cartz L (1981) Heavy ion bombardment of monoclinic ThSiO₄, ThO₂ and monazite. *Rad Eff Lett* 58: 1-3
- Landzirotti A, Hanson GN (1995) U-Pb dating of major and accessory minerals formed during metamorphism and deformation of metapelites. *Geochim Cosmochim Acta* 59: 2513-2526
- Larson AC, Von Dreele RB (1988) GSAS-Generalized structure analysis system. Los Alamos National Laboratory Report LAUR, 86-758, 1-150
- Lumpkin GL, Ewing RC (1988) Alpha-decay damage in minerals of the pyrochlore groups. *Phys Chem Mineral* 16: 2-20
- Meldrum A, Wang LM, Ewing RC (1996) Ion-beam-induced amorphization of monazite. *Nucl Instr Meth Phys Res B* 116: 220-224

- Meldrum A, Boatner LA, Ewing RC (1997) Electron-irradiation-induced nucleation and growth in amorphous LaPO_4 , ScPO_4 , and zircon. *J Matter Res* 12: 1816-1827
- Meldrum A, Boatner LA, Weber WJ, Ewing RC (1998) Radiation damage in zircon and monazite. *Geochim Cosmochim Acta* 62: 2509-2520
- Meldrum A, Boatner LA, Zinkle SJ, Wang SX, Wang LM, Ewing RC (1999) Effects of dose rate and temperature on the crystalline-to-metamict transformation in the ABO_4 orthosilicates. *Can Mineral* 37: 207-221
- Meldrum A, Boatner LA, Ewing RC (2000) A comparison of radiation effects in crystalline ABO_4 -type phosphates and silicates. *Mineral Mag* 64: 183-192
- Montel JM, Seydoux AM (1998) Sm-Nd interdiffusion in monazite. *EMPG VII, Terra abst Supl 1 to Terra Nova* 10: 42
- Murakami T, Chakoumakos BC, Ewing RC (1986) X-Ray Powder Diffraction Analysis of Alpha-Event Radiation Damage in Zircon (ZrSiO_4). In: *Advances in ceramics: Nuclear waste management II*, Clark DE, White WB and Machiels J (ed) 20: 745-753 American Ceramic Society, Columbus, Ohio
- Murakami T, Chakoumakos BC, Ewing RC, Lumpkin GR, Weber WJ (1991) Alpha-decay event damage in zircon. *Am Mineral* 76: 1510-1532
- Nasdala L, Massonne H-J (2000) Microdiamonds from the Saxonian Erzgebirge, Germany: in situ micro-Raman characterisation. *Eur J Mineral* 12: 495-498
- Nasdala L, Wolf D, Irmer G (1995) The degree of metamictization in zircon: a Raman spectroscopic study. *Eur J Mineral* 7: 471-478
- Nasdala L, Pidgeon RT, Wolf D (1996) Heterogeneous metamictization of zircon on a microscale. *Geochim Cosmochim Acta* 60: 1091-1097

- Nasdala L, Finger F, Kinny P (1999) Can monazite become metamict? *Eur J Mineral* 11, Beiheft 1: 164
- Nasdala L, Wenzel M, Andrut M, Wirth R, Blaum P (2001a) The nature of radiohaloes in biotite. *Am Mineral* 86: 498-512
- Nasdala L, Wenzel M, Vavra G, Irmer G, Wenzel T, Kober B (2001b) Metamictisation of natural zircon: Accumulation versus thermal annealing of radioactivity-induced damage. *Contrib Mineral Petrol* 141:125-144
- Ni Y, Hughes JM, Mariano AN (1995) Crystal chemistry of the monazite and xenotime structures. *Am Mineral* 80: 21-26
- Ouchani S, Dran JC, Chaumont J (1997) Evidence of ionization annealing upon helium-ion irradiation of pre-damaged fluorapatite. *Nucl Instr Meth Phys Res B* 132: 447-451
- Owen MR (1988) Radiation-damage halos in quartz. *Geology* 16: 529-532
- Parrish RR (1990) U-Pb dating of monazite and its application to geological problems. *Canadian J Earth Sci* 27: 1431-1450
- Parrish RR (1995) Thermal evolution of the southeastern Canadian Cordillera. *Can J Earth Sci* 32: 1618-1642
- Podor R (1995) Raman spectra of the actinide-bearing monazites. *Eur J Mineral* 7: 1353-1360
- Salje EKH, Chrosch J, Ewing RC (1999) Is "metamictization" of zircon a phase transition? *Am Mineral* 84: 1107-1116
- Salje EKH (2000) Structural transformations in minerals The role of temperature and radiation damage. *Berichte der Deutschen Mineralogischen Gesellschaft, Beihefte zum Eur J Miner* 12: 175

- Schärer U, Xu RH, Allègre CJ (1986) U-(Th)-Pb systematics and ages of Himalayan leucogranites, South Tibet. *Earth Plan Sci Lett* 77: 35-48
- Seydoux AM, Montel JM, Paquette JL, Marinho M (1999). Experimental study of the resetting of the U-Th-Pb geochronological system of monazite. *EUG X, Terra Nova* 10, Abstract Supplement 1: 800
- Seydoux-Guillaume AM, Paquette JL, Wiedenbeck M, Montel JM, Heinrich W. Experimental resetting of the U-Th-Pb system in monazite. Submitted in *Chem Geol*
- Smith HA, Barreiro B (1990) Monazite U-Pb dating of staurolite grade metamorphism in pelitic schists. *Contrib Mineral Petrol* 105: 602-615
- Smith HA, Giletti BJ (1997) Lead diffusion in monazite. *Geochim Cosmochim Acta* 61: 1047-1055
- Speer JA (1982) Zircon. In: *Reviews in Mineralogy* Ribbe PH (ed) 5: 67-112 Mineralogical Society of America, Washington DC
- Suzuki K, Adachi M, Kajizuka I (1994) Electron microprobe observations of Pb diffusion in metamorphosed detrital monazites. *Earth Plan Sci Lett* 128: 391-405
- Weber WJ, Ewing RC, Wang LM (1994) The radiation-induced crystalline-to-amorphous transition in zircon. *J Mater Res* 9: 688-698
- Weber WJ, Ewing RC, Catlow CRA, Diaz de la Rubia T, Hobbs LW, Kinoshita C, Matzke HJ, Motta AT, Nastasi M, Salje EHK, Vance ER, Zinkle SJ (1998) Radiation effects in crystalline ceramics for the immobilization of high-level nuclear waste and plutonium. *J Mater Res* 13: 1434-1484

CHAPTER III

Resetting of U-Pb isotopic geochronological system

“C’est en un sens à force d’étudier l’homme que nous nous sommes mis hors d’état de le connaître.”
Jean-Jacques Rousseau - *Discours sur l’origine de l’inégalité parmi les hommes*

Experimental resetting of the U-Th-Pb system in monazite

Abstract

Abraded fragments (200 to 400 μm) of a large and chemically homogeneous Brazilian monazite crystal, characterised by a concordant U-Pb ages of $474 \pm 1 \text{ Ma}$ ($^{208}\text{Pb}/^{206}\text{Pb}=19.5$), were hydrothermally treated at varying temperatures with solutions of different compositions.

Experiments with pure water over a temperature range of 800 to 1200°C, at 700 MPa and durations ranging from 5 to 60 days showed that even at 1200°C any dissolution and recrystallization of new monazite is confined to the outermost surface of the grain. Neither Pb-diffusion at the EMP scale, nor significant discordancy was observed. Additionally, we were performed experiments at 800°C and 1000°C for different durations using different fluid compositions at quartz saturation: a 10 wt % CaCl_2 fluid, a 10 wt % SrCl_2 fluid, a 10 wt % NaCl fluid and a fluid containing NBS 982 Pb standard ($^{208}\text{Pb}/^{206}\text{Pb}=1$). Product monazites from each run were analysed with SEM, EMP, SIMS and ID-TIMS.

For all runs, EMP traverses revealed no Pb-diffusion profiles. Significant overgrowths of newly formed monazite are documented by SEM analyses. They occurred only in the 1000°C experiments when either CaCl_2 or Pb-bearing fluids were present. In the CaCl_2 experiment two zones could be distinguished within the crystal: a core possessing the initial monazite composition and a rim consisting of newly formed monazite produced by dissolution/precipitation which was enriched in Ca and Pb-free. ID-TIMS dating of single grains treated with SrCl_2 and CaCl_2 solutions at 1000°C are significantly discordant. Experiments employing the NBS Pb-standard produced sub-concordant monazite, for which the $^{207}\text{Pb}/^{206}\text{Pb}$ apparent age has become older than prior to the experiment (544 Ma at 800°C and 495 Ma at 1000°C). The newly grown monazite rim had obviously incorporated Pb from the fluid.

None of our reaction products contained a detectable diffusion profile. Except for the Pb-experiment at 800°C, the only resetting mechanism we detected involved dissolution/precipitation. It is clear that the extent of the dissolution/precipitation process depends on fluid composition. Based on these results, we conclude that dissolution/precipitation rather than diffusion controls the resetting of monazite in natural rocks.

Keywords: Monazite • U-Pb isotopes • SIMS • resetting • fluid • dissolution/precipitation

1 - Introduction

The light rare earth element (LREE)-phosphate monazite is widely used as a U-Th-Pb geochronometer to determine the timing of both magmatic and metamorphic events (Parrish, 1990). In most cases, $^{206}\text{Pb}/^{238}\text{U}$ and $^{207}\text{Pb}/^{235}\text{U}$ ages in monazites are concordant (e. g. Schärer et al., 1986; Corfu, 1988; Smith and Barreiro, 1990; Landzirotti and Hanson, 1995; Parrish, 1995; Simpson et al., 2000...); nevertheless, discordant U-Pb ages have also been reported. Such discordant data may reflect mixing of different grain populations that crystallised at different times within a particular rock (Black et al., 1984; Bertrand et al., 1993; Childe et al., 1993); or a mixture of newly grown rims with inherited cores (Montel et al., 1996; Braun et al., 1998; Cocherie et al., 1998; Crowley and Ghent, 1999; Williams et al., 1999; Zhu and O’Nions, 1999; Poitrasson et al., 2000; Rubatto et al., 2001; Townsend et al., 2001...); or else a diffusive Pb loss (Suzuki and Adachi, 1994; Suzuki et al., 1994). Clearly the correct interpretation of measured isotope ratios, then of the ages, requires a detailed understanding of the resetting process that affects the isotope system of monazite.

Despite the fact that major analytical progress on the U-Th-Pb isotope system in natural monazite has recently been achieved by SIMS (Harrison, 1995; Grove and Harrison, 1999; Zhu et al., 1997, Rubatto et al., 2001...), LA-ICP-MS (Poitrasson, 1996; 2000) and EMP methods (Montel et al., 1996; Cocherie et al., 1998; Crowley and Ghent, 1999), the controlling mechanisms that induce its partial or complete resetting during a geological event are only poorly understood. There is overall agreement that, in nature, the U-Th-Pb system in monazite may be reset by loss of Pb by interacting with coexisting fluids, implying a dissolution/precipitation process. The partitioning of elements between fluid and growing monazite would thus define the U-Th-Pb budget of any newly formed rims.

With respect to resetting by diffusive Pb-loss, there have been several attempts to interpret discordant ages of natural monazite grains in terms of Dodson’s (1973)-closure temperature. Estimations for closure temperatures range from $530 \pm 25^\circ\text{C}$ (Black et al., 1984) to $725 \pm 25^\circ\text{C}$ (Copeland et al., 1988). A major drawback of the closure temperature concept is that it ignores all quantification of the main driving force for any diffusion process; in this case the chemical potential gradient of the Pb between monazite and the adjacent phase, be it silicate, fluid or melt. If this gradient is small or zero, significant Pb-loss via volume diffusion is unlikely. Additionally, experiments on Pb-self-diffusion in monazite by Smith and Giletti (1997) showed that such self-diffusion is very slow, even at high temperatures. Furthermore, it has been shown that monazite inclusions shielded by host minerals such as quartz or garnet

are not subject to resetting, despite the fact that they were exposed to granulite-facies temperatures of more than 800°C over long time scales (De Wolf et al., 1993; Kalt et al., 2000; Montel et al., 2000). It thus appears that volume diffusion is not a key mechanism for the resetting of the U-Pb system of monazite.

Dissolution/precipitation in the presence of a fluid phase is a second possible mechanism for a partial or even a complete resetting of the monazite isotope system. If so, one would expect that fluid composition has a major effect on the process. In a previous study, Teufel and Heinrich (1997) demonstrated that the hydrothermal treatment of natural monazite grains larger than 40µm at 750°C/0.3 GPa using pure water did not affect their U-Pb system. Significant dissolution and precipitation along with Pb-loss into pure water was only observed when very fine powdered monazite was used as starting material. Obviously these experiments with pure water did not demonstrate definitely whether dissolution-precipitation is an important process for resetting large natural monazites.

In this study we present an experimental study of the resetting of a natural monazite under hydrothermal conditions. The effects of pure water at high temperature (>800°C), NaCl, CaCl₂ and SrCl₂-bearing fluids on the dissolution-precipitation process and the concomitant redistributions of elements and isotopes are evaluated. NaCl was used as an analogue for relevant crustal fluid. Sr- and Ca-bearing fluids were used to test for an exchange between Ca²⁺ (1.18 Å) or Sr²⁺ (1.31 Å) with Pb²⁺ (1.35 Å) (radii from Shannon, 1976) and because both of these elements are abundant in monazite hosting minerals such as garnet and plagioclases. Further, we investigated the effect on the Pb-isotopic compositions of monazite if treated with a NBS 982 Pb solution. This Pb-spike is very depleted in ²⁰⁸Pb compared to monazite so that any modification to the Pb system should be readily visible. Furthermore, because crustal fluids are generally SiO₂ saturated, we buffered most experiments with SiO₂, except for those experiments involving pure water. Our data constrain which mechanisms dominate the resetting of the U-Th-Pb isotope system in monazite and we establish what influence the composition of the fluid phase and temperature have on this process.

Table 1 - EMP analyses for the untreated monazite (Untreated Mz) and some representative analyses for a monazite grain from the VRM0-1 experiment (1000°C, 1GPa, 21 days) at different distances from the crystal rim (see figure 3).

Distance along E-F (μm) in VRM0-1 (1000°C, CaCl_2 -bearing fluid)							
	Untreated Mz	24	80	100	102	104	110
Weight %							
P ₂ O ₅	27.81	27.46	28.07	27.14	27.03	27.33	27.51
SiO ₂	1.42	1.77	1.42	1.51	1.83	1.66	1.43
ThO ₂	6.92	7.27	6.92	7.55	9.37	8.64	7.24
UO ₂	0.13	0.21	0.08	0.05	0.06	0.15	0.12
Y ₂ O ₃	0.71	0.70	0.63	0.41	0.27	0.63	0.69
La ₂ O ₃	14.51	13.83	14.17	14.05	13.90	13.43	13.93
Ce ₂ O ₃	30.59	29.99	29.92	29.87	29.23	29.56	30.05
Pr ₂ O ₃	3.14	3.22	3.13	2.96	3.10	3.17	3.02
Nd ₂ O ₃	10.2	10.53	10.03	10.47	10.86	10.34	10.28
Sm ₂ O ₃	2.05	2.22	2.13	2.19	2.03	2.13	2.04
Gd ₂ O ₃	0.94	1.06	0.92	1.00	0.88	0.97	0.92
Tb ₂ O ₃	–	0.12	0.07	0.11	0.14	0.02	0.07
Dy ₂ O ₃	0.11	0.15	0.16	0.07	0.01	0.09	0.12
Ho ₂ O ₃	–	0.00	0.04	0.00	0.00	0.00	0.00
Er ₂ O ₃	0.05	0.08	0.11	0.00	0.10	0.01	0.02
Yb ₂ O ₃	–	0.02	0.03	0.01	0.00	0.00	0.06
Lu ₂ O ₃	–	0.04	0.00	0.00	0.00	0.00	0.00
PbO	0.16	0.00	0.00	0.00	0.00	0.13	0.18
CaO	0.44	0.53	0.61	0.57	0.56	0.45	0.39
Σ	99.18	99.19	98.43	97.94	99.35	98.71	98.06
Cations (pfu) on the basis of 16 Oxygens							
P	3.782	3.734	3.812	3.75	3.704	3.747	3.784
Si	0.229	0.284	0.228	0.247	0.296	0.269	0.232
Th	0.253	0.266	0.253	0.28	0.345	0.318	0.268
U	0.005	0.007	0.003	0.002	0.002	0.005	0.004
Y	0.061	0.06	0.054	0.035	0.023	0.054	0.06
La	0.86	0.819	0.838	0.846	0.83	0.802	0.835
Ce	1.799	1.764	1.757	1.785	1.732	1.753	1.788
Pr	0.184	0.188	0.183	0.176	0.183	0.187	0.179
Nd	0.585	0.604	0.575	0.61	0.628	0.598	0.596
Sm	0.114	0.123	0.118	0.123	0.113	0.119	0.114
Gd	0.05	0.056	0.049	0.054	0.047	0.052	0.049
Tb	–	0.006	0.004	0.006	0.007	0.001	0.004
Dy	0.006	0.008	0.008	0.003	0	0.005	0.006
Ho	–	0	0.002	0	0	0	0
Er	0.002	0.004	0.005	0	0.005	0.001	0.001
Yb	–	0.001	0.001	0	0	0	0.003
Lu	–	0.002	0	0	0	0	0
Pb	0.007	0	0	0	0	0.006	0.008
Ca	0.076	0.092	0.105	0.100	0.097	0.078	0.067
Σ	8.013	8.018	7.995	8.017	8.012	7.995	7.998
End members							
LREEPO ₄	0.898	0.889	0.880	0.899	0.883	0.878	0.890
YHREEPO ₄	0.017	0.020	0.019	0.011	0.009	0.015	0.019
CaThU(PO ₄) ₂	0.038	0.025	0.053	0.028	0.034	0.039	0.034
PbThU(PO ₄) ₂	0.004	0.000	0.000	0.000	0.000	0.003	0.004
ThSiO ₄	0.043	0.054	0.037	0.056	0.069	0.059	0.049
USiO ₄	0.001	0.001	0.000	0.000	0.000	0.001	0.001
Σ	1.001	0.989	0.989	0.994	0.996	0.995	0.996

Table 2 - U-Pb isotope data for monazite reactants and products (single grain analysis)

Analysed sample	Weight (µg)	U	Pb rad	$\frac{^{206}\text{Pb}}{^{204}\text{Pb}}$	$\frac{^{208}\text{Pb}}{^{206}\text{Pb}}$	$\frac{^{206}\text{Pb}}{^{238}\text{U}}$	$\frac{^{207}\text{Pb}}{^{235}\text{U}}$	$\frac{^{207}\text{Pb}}{^{206}\text{Pb}}$	$\frac{^{206}\text{Pb}}{^{238}\text{U}}$	$\frac{^{207}\text{Pb}}{^{235}\text{U}}$	$\frac{^{207}\text{Pb}}{^{206}\text{Pb}}$	Discordancy (%)
		concentrations (ppm)		atomic ratios					apparent ages (Ma)			
Untreated monazite 1	40	1216	1670	3692	19.5718	0.07631 ± 5	0.5950 ± 5	0.05655 ± 2	474	474	474	0
Untreated monazite 2	58	1310	1788	4651	19.4575	0.07629 ± 5	0.5951 ± 4	0.05657 ± 2	474	474	475	0
Untreated monazite 3	41	868	1189	3773	19.4590	0.07650 ± 27	0.5973 ± 22	0.05662 ± 6	475	476	477	0
Untreated monazite 4	38	1286	1758	3693	19.4553	0.07634 ± 36	0.5956 ± 29	0.05659 ± 4	474	474	475	0
Untreated monazite 5	37	1005	1399	1350	19.6078	0.07646 ± 64	0.5965 ± 52	0.05658 ± 15	475	475	475	0
VRM97-10 (1000°C, H ₂ O)	87	1248	1650	2290	19.2005	0.07457 ± 37	0.5814 ± 40	0.05657 ± 26	464	465	474	3.2
VRM97-8 (1100°C, H ₂ O)	123	1087	1471	1757	19.3870	0.07554 ± 53	0.5892 ± 60	0.05657 ± 40	469	470	475	1.3
VRM97-8 (2) (1100°C, H ₂ O)	116	1051	1412	1758	19.2604	0.07542 ± 115	0.5878 ± 99	0.05652 ± 41	469	469	473	1.2
VRM97-6 (1200°C, H ₂ O)	107	1224	1623	2141	18.9959	0.07555 ± 33	0.5887 ± 42	0.05652 ± 30	470	470	473	0
VRM99-2 (1100°C, H ₂ O-SiO ₂)	26	1076	1484	416	19.0767	0.07579 ± 216	0.5915 ± 299	0.05660 ± 226	471	472	476	1.2
VRM0-7 (800°C, Pb-spike)	116	852	1254	253	16.9981	0.08699 ± 44	0.7000 ± 37	0.05836 ± 87	538	539	543	-
VRM0-18 (1000°C, Pb-spike)	78	1024	1392	530	18.1686	0.07851 ± 70	0.6181 ± 57	0.05710 ± 12	487	489	495	-
VRM0-4 (800°C, CaCl ₂)	102	576	780	706	18.8929	0.07640 ± 147	0.5959 ± 178	0.05657 ± 124	475	475	475	0
VRM0-1 (1000°C, CaCl ₂)	204	507	226	3253	19.7006	0.02464 ± 43	0.1921 ± 35	0.05655 ± 23	157	178	474	67.8
VRM0-3 (800°C, SrCl ₂)	90	645	878	3630	19.3986	0.07626 ± 75	0.5945 ± 60	0.05654 ± 14	474	474	476	0
VRM0-2 (1000°C, SrCl ₂)	126	669	767	4555	19.4326	0.06416 ± 105	0.5001 ± 82	0.05653 ± 9	401	412	473	16.0
VRM0-17 (800°C, NaCl)	83	677	918	2838	19.5046	0.07546 ± 36	0.5873 ± 35	0.05645 ± 20	469	469	470	0

For untreated monazites, a 4 pg blank correction was applied corresponding to a corrected $^{206}\text{Pb}/^{204}\text{Pb}$ ratio of around 6500. For the treated monazites, it was necessary to add an experimental blank in the calculations. Nevertheless, it is not possible to precisely define an experimental blank.

Consequently, an individual experimental blank was determined for each experiment in order to obtain a corrected $^{206}\text{Pb}/^{204}\text{Pb}$ ratio of 6500.

2 - Sample selection and description, and experimental procedure

A monazite single crystal, 3×2-cm in size, from the Itambe pegmatite district (Brazil, Cruz et al., 1996) was used for this study. The yellow-orange crystal is nearly free of fluid and solid inclusions, and is homogeneous at the micrometer scale. EMP-analyses show a composition typical for natural monazites (Table 1, first column) and it contains 7.25 wt.% ThO₂, 0.13 wt.% UO₂ and 0.16 wt.% PbO. In terms of end-members, the LREE_{La-Gd}PO₄ component makes up 89.8 mol% and the Y+HREE_{Tb-Lu}PO₄ component 1.7 mol%. Th is incorporated through about equal amounts of brabantite CaTh(PO₄)₂ (~3.8 mol%) and huttonite ThSiO₄ (4.3 mol%) components. Detailed study using TEM, XRD, and raman methods showed that this monazite is non-metamict (Seydoux-Guillaume et al., submitted). Multiple ID-TIMS dating yielded concordant U-Pb ages of 474 ± 1 Ma (Table 2).

A fragment of the crystal was broken and sieved into different grain size fractions. For our experiments the 200-400 µm fraction was used. The angular grains obtained after crushing were mechanically air-abraded (Krogh, 1982) in order to obtain a rounded morphology (Figure 1a). This was done to avoid the preferential dissolution of the angular edges during hydrothermal experiments (Teufel and Heinrich, 1997). Abraded fragments were washed in 0.1N HNO₃. Only well rounded grains devoid of micro-inclusions were selected for our experiments.

A long duration experiment using pure water was performed at 800°C/0.2 GPa for 60 days. Shorter duration runs were performed at 1000°C, 1100°C and 1200°C/0.7 GPa for 7, 12 and 5 days, respectively (Table 3). About 10 grains of abraded fragments were placed into a platinum capsule (0.2 mm wall thickness) filled with ~20 mg of distilled H₂O. The capsules, 15 mm in length and 3 mm in diameter, were welded and checked for leaks by heating at 110°C for 24 hours. A standard cold seal pressure vessel was used for the 800°C/0.2 GPa experiment. For experiments at higher temperatures an internally heated pressure vessel (IHPV), using N₂ as the pressure medium, was employed. Temperature error is within ± 2°C for the 800°C, and ± 25°C for the 1200°C. Details about the apparatus and calibration procedure can be found in Vielzeuf and Montel (1994). At the end of the runs, vessels were quenched to room temperature within a few minutes. After quenching each capsule was checked for leakage by weighing.

Table 3 - Experimental conditions of all runs

Sample #	Weight of monazite (mg)	Weight of fluid (mg)	Composition of fluid	Temperature (°C)	Pressure (Gpa)	Duration (days)
VRM97-3	0.97	20	H ₂ O	800	0.2	60
VRM97-10	0.62	20	H ₂ O	1000	0.7	7
VRM97-8	1.14	20	H ₂ O	1100	0.7	12
VRM97-6	0.72	20	H ₂ O	1200	0.7	5
VRM99-2	0.55	10	H ₂ O + SiO ₂	1100	0.2	27
VRM0-7	2.33	11.44	NBS 982 Pb + SiO ₂	800	0.2	26
VRM0-18	1.03	11.52	NBS 982 Pb + SiO ₂	1000	1	14
VRM0-4	1.96	11.71	10 wt% CaCl ₂ + SiO ₂	800	0.2	39
VRM0-1	2.27	11.84	10 wt% CaCl ₂ + SiO ₂	1000	1	21
VRM0-3	1.92	12.05	10 wt% SrCl ₂ + SiO ₂	800	0.2	39
VRM0-2	2.05	11.42	10 wt% SrCl ₂ + SiO ₂	1000	1	21
VRM0-17	0.97	11.85	10 wt% NaCl + SiO ₂	800	0.2	18

One experiment was performed at 1100°C/0.2 GPa in silica saturated water. For that about 30 monazite grains plus 1 mg SiO₂ powder were placed into a Pt-capsule along with 10 µl distilled H₂O. This experiment was also run in an IHPV.

In another series of experiments, monazites were treated with fluids of different compositions: H₂O-NaCl, H₂O-CaCl₂ or H₂O-SrCl₂. Salt concentrations were 10 wt% in all runs. Additionally, an HNO₃-bearing solution containing 950 µg/g NBS 982 Pb standard (²⁰⁸Pb/²⁰⁶Pb=1.000, ²⁰⁷Pb/²⁰⁶Pb=0.467 and ²⁰⁶Pb/²⁰⁴Pb=36.765) was used in two runs. At 800°C/0.2 GPa, experiments were again performed in standard cold seal hydrothermal pressure vessels, and at 1000°C/1 GPa in a piston-cylinder apparatus with a 22 mm diameter pressure chamber and CaF₂ as pressure medium. In the latter, Pt-PtRh thermocouples were used for temperature control. The temperature difference along the 13 mm long capsules was ± 13°C at 1000°C, and the variation of temperature during the run was ± 2°C. Piston cylinder experiments were quenched in a few seconds. Experimental conditions of all runs are summarised in Table 3.

Subsequent to each run the samples were hand-picked and split up for optical microscopy, SEM, EMP and SIMS analyses. A single grain of each run was selected for ID-TIMS analysis.

3 - Analytical methods

Grain surface morphology was investigated using a SEM. BSE and SE images were made on grains for each using a Zeiss DSM962 scanning electron microscope. Acceleration voltage was typically 15 kV.

Additionally, EMP analyses of polished single monazite grains mounted in epoxy resin were obtained using a CAMECA SX-50 electron microprobe equipped with a wavelength dispersive system. The operating conditions are given in Förster et al. (1998a). Core-rim relationships of at least one monazite grain from each run were evaluated by measuring compositional profiles in 2 µm steps across the grain. Furthermore, X-ray imaging was conducted on a monazite grain from run VRM0-1 (1000°C, 1 GPa, CaCl₂-bearing solution) using a Cameca SX 100 microprobe. Element mapping for Th-M_α, Pb-M_β and U-M_β was made in wave-length-dispersive mode, and for Ca-K_α, Ce-L_α and P-K_α in energy dispersive

mode with the following conditions: accelerating potential 20 kV, beam current 30 nA and scan of 256×256 pixels with 600 ms/pixel.

The Cameca ims 6f ion probe in Potsdam was used to acquire digital images of the relative concentration distributions of selected elements within our monazite sample VRM0-1 (1000°C, CaCl₂ fluid). In addition to images acquisition, profiles across the margins of grains produced in VRM0-7 (800°C, 0.2 GPa, Pb-spike solution) and VRM0-18 (1000°C, 1 GPa, Pb-spike solution) were also performed. This technique provides more precise information of one-dimensional variations of the target elements, but at the cost of reduced spatial resolution (see appendix for details).

Individual thermal ionisation U-Pb isotope analyses were performed in Clermont-Ferrand on five abraded monazite fragments from our starting material plus on one product grain from each experiment. The handpicked selected grain was washed before in a 0.1N HNO₃ heated solution in order to clean grains from experiment derived in common Pb contamination. The selected monazite grain was dissolved using 8N HCl in a PFA Teflon modified version of Parrish-type microcapsules (Parrish, 1987) at 210°C, during 16-20 hours. Chemical separation and mass spectrometry were performed according to Pin and Paquette (1997).

4 - Results

Optical microscope revealed a complete decolorisation of the monazite grains after all runs. Teufel and Heinrich (1997) have already reported this effect. The colour changed from yellowish orange to whitish grey.

4-1 - Grain-surface morphology:

SEM images for experiments with H₂O+SiO₂, NaCl, SrCl₂, CaCl₂ at 800°C and Pb-spike at 800°C showed no textural modifications of the monazite grains after the run (Figures 1 d, e and f). Quartz crystals related to the SiO₂ in excess in the capsule were present in all runs. For the experiment with SrCl₂ fluid at 800°C few small SrCl₂ crystals were found in the

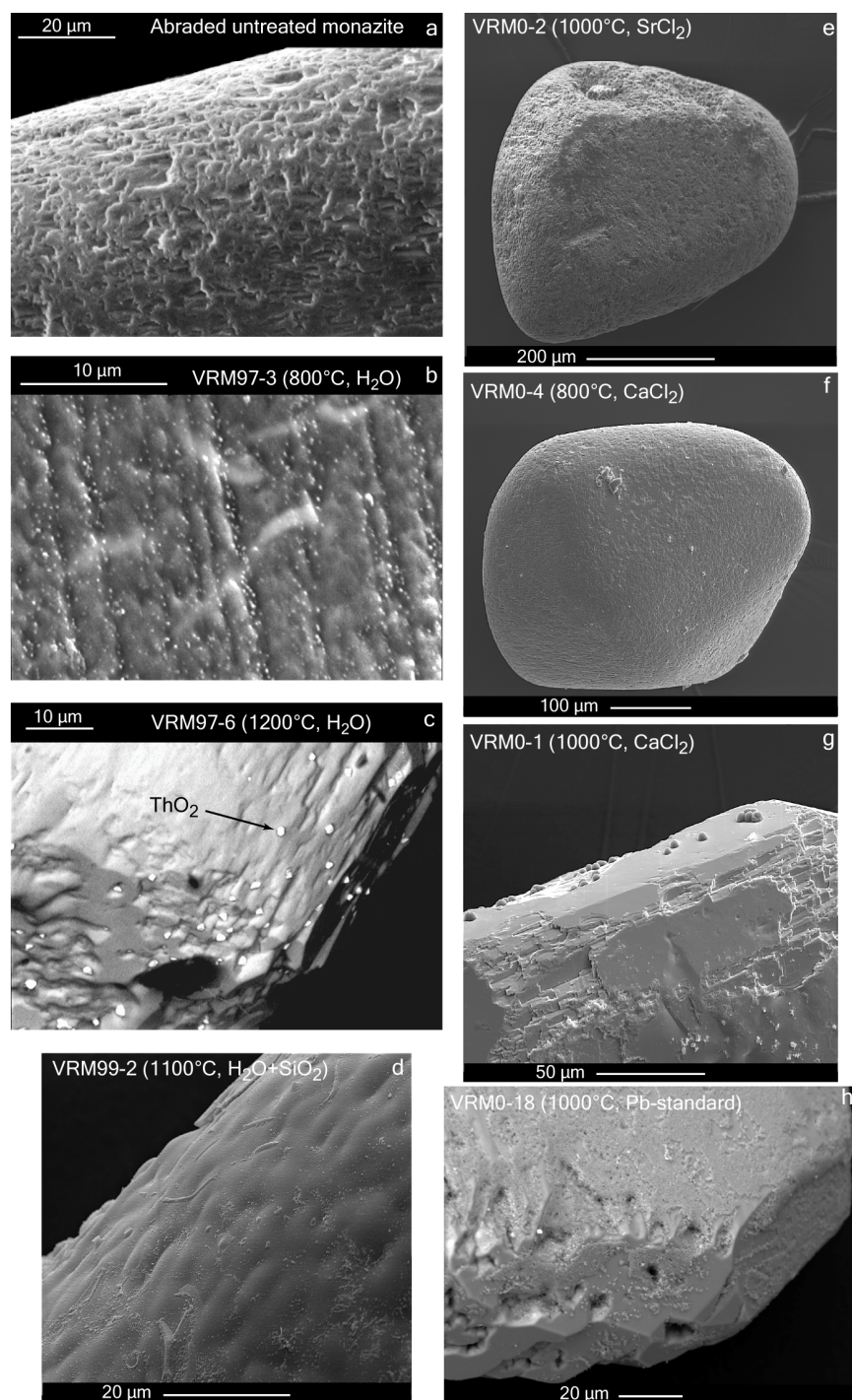


Figure 1: SEM micrographs illustrating textural characteristics observed in both untreated and treated monazite.

- a)** Surface details of an abraded but otherwise untreated monazite fragment
- b)** Surface details of a monazite grain from the experiment VRM97-3 (H_2O , 800°C). Many small (200 nm) "bright" crystals of thorianite (ThO_2) were observed on the surface of the grain.
- c)** Surface details of a monazite grain from the experiment VRM97-6 (H_2O , 1200°C). The grain appears totally recrystallised with very large, newly formed faces and ThO_2 crystals were observed.
- d)** Experiment VRM99-2 ($\text{H}_2\text{O} + \text{SiO}_2$, 1100°C). Presence of Si in the system seems to avoid formation of ThO_2 crystals.
- e)** Experiment VRM0-2 (SrCl_2 , 1000°C). No overgrowth was observed.
- f)** Experiment VRM0-4 (CaCl_2 , 800°C). No overgrowth was observed.
- g)** Experiment VRM0-1 (CaCl_2 , 1000°C). Significant overgrowths were observed. Monazite shows newly formed faces.
- h)** Experiment VRM0-18 (Pb -standard, 1000°C). Significant overgrowths were observed. Monazite shows newly formed faces.

run products. For the experiment with CaCl_2 fluid at 800°C , precipitation of some brabantite crystals $(\text{Ca, Th}) (\text{PO}_4)_2$ occurred.

For experiments with pure H_2O SEM observations showed little modifications at the surface of the grains. At 800°C , there is no apparent modification of monazite grains excepted the precipitation of numerous 200 nm “bright” (in fact appearing bright in BSE mode in SEM) crystals on the grain surfaces (Figure 1b). However, at temperatures higher than 1000°C the development of new, $\sim 5\ \mu\text{m}$ long crystal faces on the grain surface as well as “bright” crystals, 1-2 μm large, were observed. At 1100°C these faces are longer, reaching 12 μm in length. Finally, by 1200°C the grain surface was totally recrystallised completely replacing the original abraded morphology. Large newly formed faces ($>40\ \mu\text{m}$) and larger “bright” crystals with visible morphology are visible (Figure 1c). EDS analysis demonstrated that the faces are newly formed, Th-free monazite and that the “bright” crystals are ThO_2 (thorianite), which is consistent with their cubic morphology.

Because Th can be incorporated in monazite via the $[\text{P}_{-1}\text{REE}_{-1}\text{Si}_1\text{Th}_1]$ thorium-silicate component, the presence of silica might have affected the monazite solution interactions. In contrast to the SiO_2 -free experiment VRM97-8, SEM observations of monazite grain from our experiment VRM99-2 (water + SiO_2), figure 1d shows no growth of newly formed monazite and no ThO_2 on the surface. We conclude that an excess of SiO_2 in the system prevented the formation of new ThO_2 crystals. This is a first indication of the effect of fluid composition on monazite behaviour in fluids.

Finally, two experiments showed significant overgrowths. The first with CaCl_2 fluid at 1000°C (Figure 1g) and the second with Pb fluid at 1000°C (Figure 1h). In both experiments the monazite grains seems to have fully recrystallised.

4-2 - Modifications of chemical compositions:

EMP imaging (BSE and X-ray) and concentration profiles from the rims to the centres of monazite grains showed no variation of the chemical composition; particularly important is that we detected no Pb-diffusion profiles for experiments with H_2O , $\text{H}_2\text{O}+\text{SiO}_2$, NaCl , SrCl_2 , CaCl_2 at 800°C and Pb fluids.

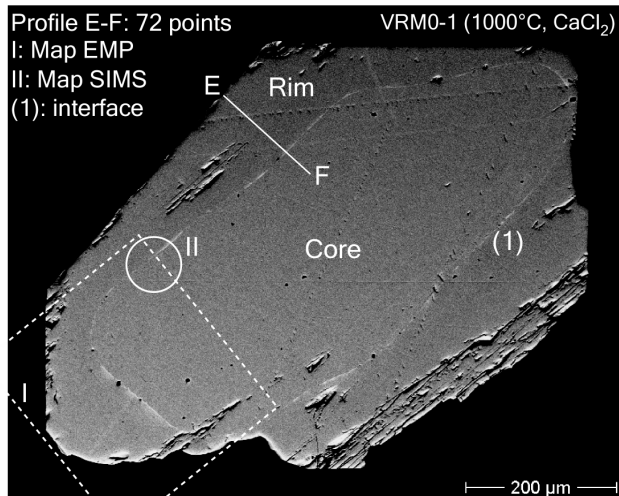


Figure 2: BSE image of a polished monazite grain from VRM0-1 (1000°C, CaCl₂) in epoxy showing the location of EMP profile (E-F) from the figure 3, EMP-X-Ray imaging (map I) from the figure 4 and SIMS-imaging (map II) from the figure 5. The interface (1) between the rim and the core of this grain is clearly visible.

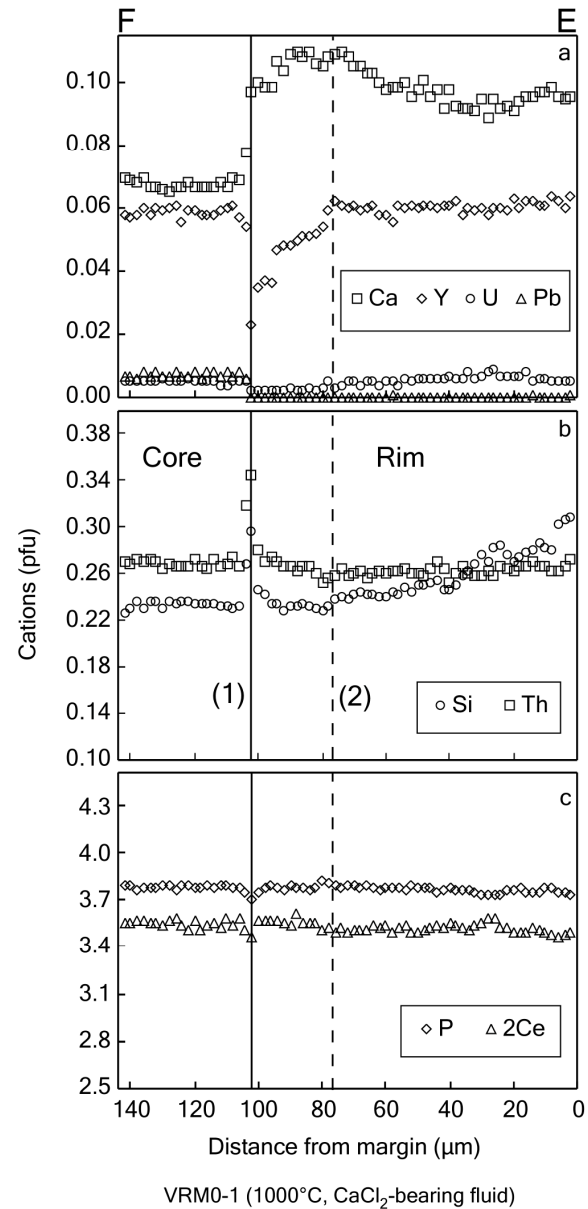


Figure 3: EMP-traverse E-F across rim-core interface (figure 2). Ca, Y, U, Pb, Th, Si, P and Ce content in cations are reported and some analyses are in table 2. The line at 102 μm corresponds to the "bright" interface (1) observed on figure 2. The boundary (2) corresponds to the diffuse interface visible on figures 4 and 5.

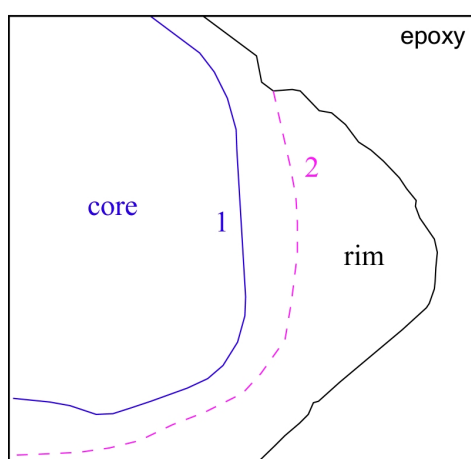
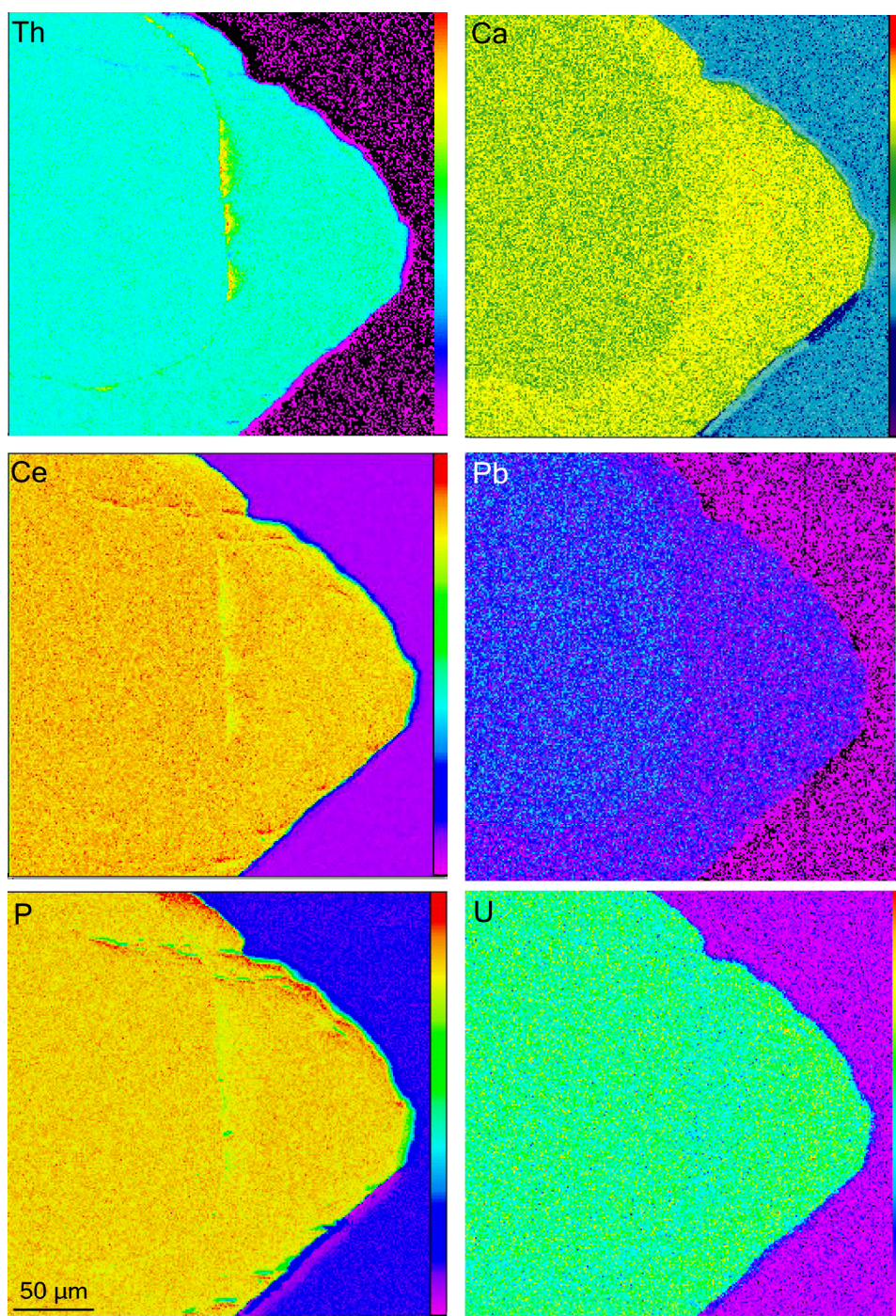
VRM0-1 (1000°C, CaCl₂)

Figure 4: X-Ray imaging (map I) from the grain shown in figure 2 (experiment VRM0-1 with CaCl₂ at 1000°C).

Th, Pb and U were analysed with WDS and Ca, Ce and P with EDS using a Cameca SX-100 EMP.

Analytical conditions:

30 nA, 20 kV, 256 × 256 µm, 600 ms/µm.

The drawing under the images shows the distinguished zones: the sharp interface (1) between the rim and the core and a diffuse interface (2). Between (1) and (2) U is depleted and Ca enriched.

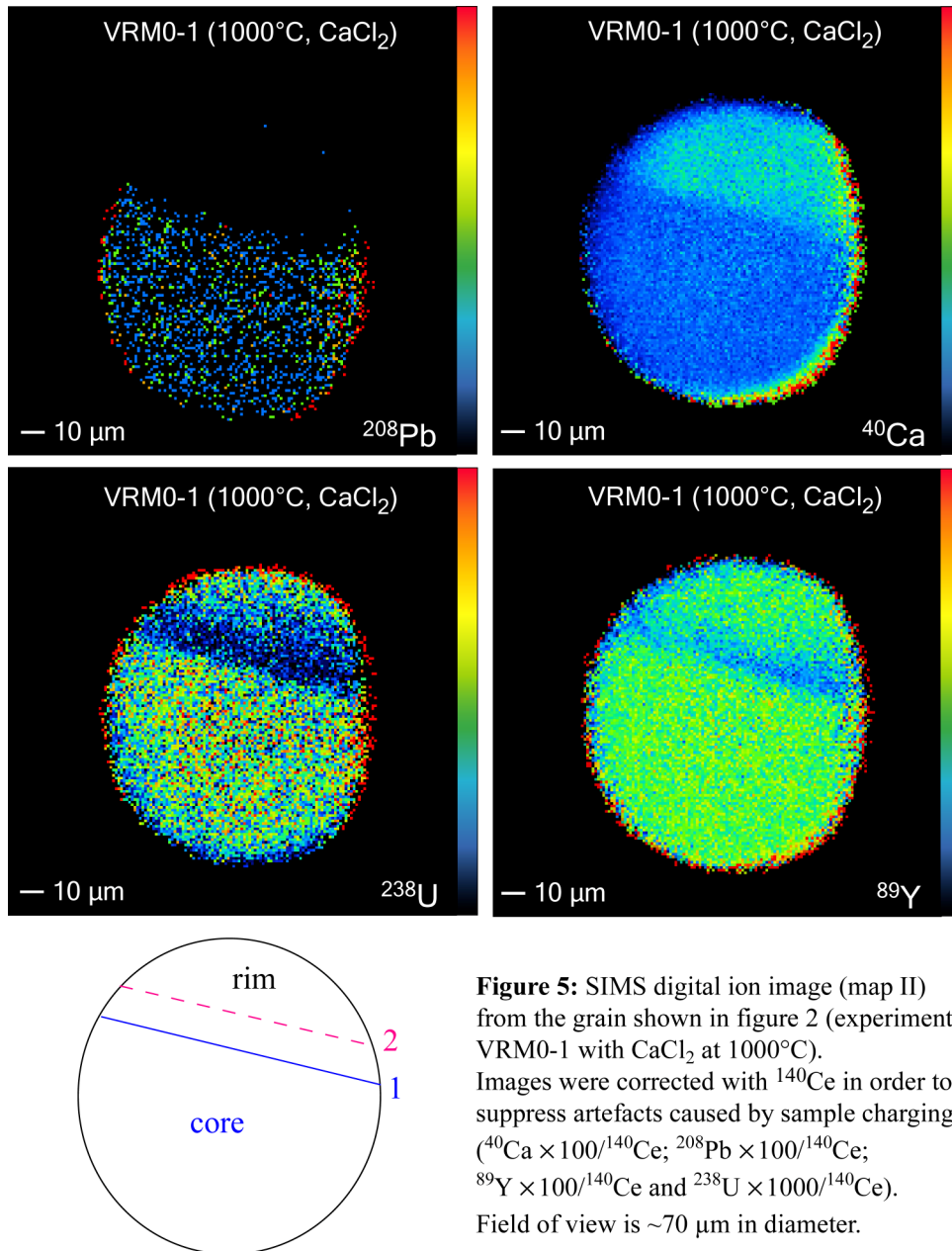


Figure 5: SIMS digital ion image (map II) from the grain shown in figure 2 (experiment VRM0-1 with CaCl₂ at 1000°C). Images were corrected with ¹⁴⁰Ce in order to suppress artefacts caused by sample charging (⁴⁰Ca × 100/¹⁴⁰Ce; ²⁰⁸Pb × 100/¹⁴⁰Ce; ⁸⁹Y × 100/¹⁴⁰Ce and ²³⁸U × 1000/¹⁴⁰Ce). Field of view is ~70 μm in diameter.

Only the experiment with CaCl_2 at 1000°C showed significant variations in monazite chemical composition. In order to confirm this result a second grain was analysed. BSE imaging and EMP traverses of these two monazite fragments both document significant zonation. Figure 2 shows BSE image for one grain prepared for EMP. Two domains are clearly visible demarked by a “bright” discontinuity (1). The external domain (rim) shows sharper faces as compared to the internal domain (core). On this grain, EMP profile E-F from the rim to the core of the grain (Figure 3), X-ray imaging (Figure 4) and SIMS imaging (Figure 5) were performed. The EMP and SIMS maps show that the results obtained on the profile can be generalised to the whole grain. Two zones with different chemical compositions, separated by a sharp boundary (1) could be readily distinguished in all data sets. At a distance of $102\ \mu\text{m}$ from the rim, a significant enrichment in Th and Si is observed over a $2\text{-}4\ \mu\text{m}$ distance, correlated with a P and Ce depletion. The rim is free of Pb but enriched in Ca relative to the initial monazite (Figures 3, 4 and 5). Furthermore, in contrast to the core, the ThSiO_4 end-member newly formed in the rim is greater than the REEPO_4 component (Table 1). A more gradual decrease in both U and Y concentrations at about $80\ \mu\text{m}$ from E is also observed (Figure 3). The $(\text{Y}+\text{HREE})\text{PO}_4$ xenotime and USiO_4 coffinite components decrease (Table 1) whereas Ca increases. U and Y are depleted between (1) and (2) over a distance of $\sim 30\ \mu\text{m}$ (Figures 4 and 5), whereas Ca is enriched. The discontinuity (2), better visible using SIMS imaging (Figure 5), is more diffuse. Furthermore, the Si content increases gradually starting $60\ \mu\text{m}$ away from E (Figure 3). The core showed the same composition than the initial monazite (Table 1) and no other significant variations were observed.

4-3 - Isotopic modifications:

The results from U-Pb isotope analyses are reported in table 2. For the experiments employing H_2O , $\text{H}_2\text{O}+\text{SiO}_2$, NaCl , SrCl_2 and CaCl_2 at 800°C , single grains analyses yielded sub-concordant to concordant U-Pb ages in the range of 458-475 Ma (Table 2 and Figure 6). U and Pb concentrations coincide within error limits (Table 2). A duplicate of the experiment at 1100°C with H_2O demonstrates the reproducibility of the U-Pb isotope analyses and the homogeneity of run products.

Significant discordancy was only observed at 1000°C when CaCl_2 or SrCl_2 were present in the fluid. In the SrCl_2 enriched fluid, the discordancy was about 16 % (Table 2 and Figure 6),

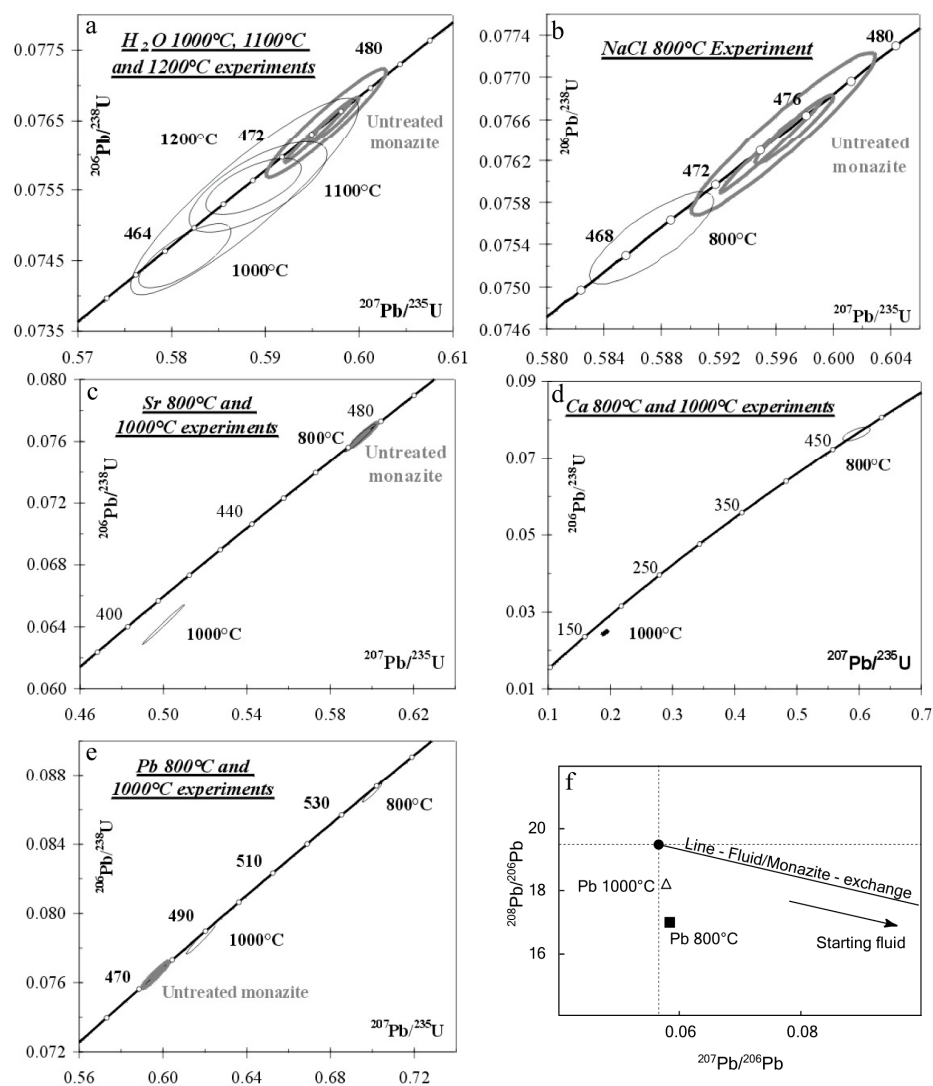


Figure 6: U-Pb concordia diagrams for monazites experimentally treated by several fluids.

a) untreated monazite and experiments with H_2O

b) experiments with NaCl

c) Experiments with $SrCl_2$

d) Experiments with $CaCl_2$

e) Experiments with Pb-spike.

f) $^{208}Pb/^{206}Pb$ vs. $^{207}Pb/^{206}Pb$ diagram. Pb 800°C and Pb 1000°C correspond to the experimental values measured with ID-TIMS (see table 2)

Individual error ellipses are quoted at the 2σ level. The analytical point for H_2O+SiO_2 is not plotted in the diagram owing to the very large error ellipse. Nevertheless, the point is centred on the untreated monazite and consequently can be considered as concordant.

whereas in the case of CaCl_2 enriched fluid the discordancy was 68% (Figure 6). This Pb-loss is in agreement with the EMP results, which show a volume of about 70% from the newly grown, Pb-free monazite.

U-Pb analyses of experiments with the Pb-enriched fluid show very different isotopic Pb ratios than before the experiments, this effect is most pronounced in the 800°C run. The $^{208}\text{Pb}/^{206}\text{Pb}$ ratio decreases from ~19.5 to 17.0 at 800°C and 18.2 at 1000°C and the $^{207}\text{Pb}/^{206}\text{Pb}$ increase from ~0.0566 to 0.0584 at 800°C and 0.0571 at 1000°C, reflecting an enrichment of both ^{207}Pb and ^{206}Pb relative to ^{208}Pb (Table 2). This results in sub-concordant analytical data points where the apparent $^{207}\text{Pb}/^{206}\text{Pb}$ age is older than that of the initial monazite (Figure 6). Thus, the $^{207}\text{Pb}/^{206}\text{Pb}$ age obtained from the experiment at 800°C (543 Ma) is older than that for the experiment at 1000°C (495 Ma). SIMS traverses from epoxy to the centre of the grains, with a 3 μm step size, were performed in one grain produced from each of these two experiments: A-B for VRM0-7 (800°C) and C-D for VRM0-18 (1000°C) (Figures 7 and 8). The observed ^{208}Pb and ^{206}Pb secondary ion intensities were normalised to ^{140}Ce to compensate for any drift in the primary ion beam intensity. For the experiment at 800°C, the $^{206}\text{Pb}/^{140}\text{Ce}$ ratio increases exponentially from the centre B to the boundary of the grain, while the $^{208}\text{Pb}/^{140}\text{Ce}$ ratio slowly increases (Figures 8a). The weaker increase in ^{208}Pb results from the very high initial ^{208}Pb content in monazite (~95%); a so small variation in ^{208}Pb will not be possible to detect. For the experiment at 1000°C, the same trends were observed but they are less pronounced (Figures 8b). These results are in good agreement with results from ID-TIMS.

5 - Discussion

Even experiments at the very high temperature of 1200°C (5 days in water) showed no resetting, neither by diffusion nor by dissolution-precipitation. For all runs, EMP traverses show no diffusion profiles, and in particular no Pb-diffusion profile. For Pb, this is in agreement with the data about Pb diffusion in monazite (Suzuki et al., 1994; Smith and Giletti, 1997). From these data we can calculate the diffusion distance for Pb in monazite using the Einstein relation:

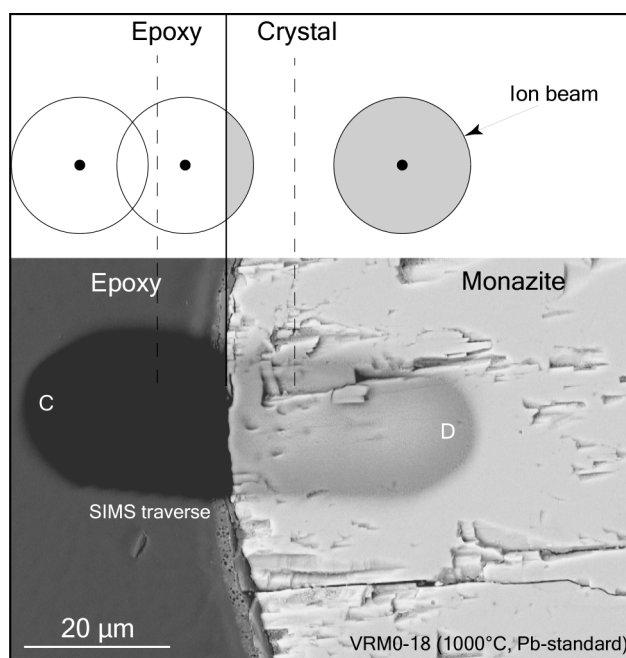


Figure 7: BSE image of a monazite grain prepared for SIMS. Grain in epoxy. Step scan of the ion beam is visible (see the drawing too) and indicates that the Au-coat has been removed from a $\sim 15 \mu\text{m}$ wide path.

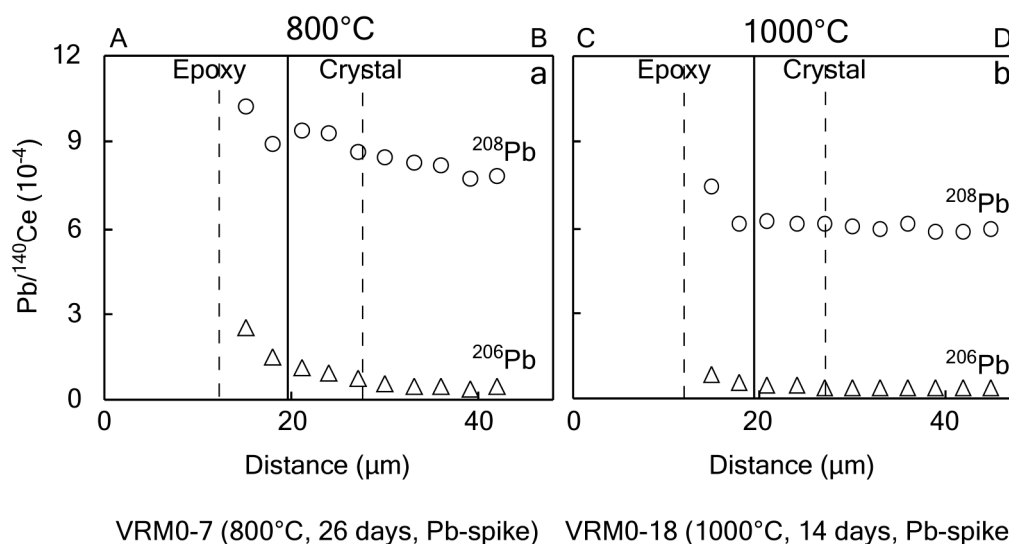


Figure 8: SIMS traverses of a grain from VRM0-7 (800°C, Pb-spike) on the left (a) and on a grain from VRM0-18 (1000°C, Pb-spike) on the right (b). $^{206}\text{Pb}/^{140}\text{Ce}$, $^{208}\text{Pb}/^{140}\text{Ce}$ were determined. The full lines indicate the boundary between the epoxy and the grain. Ion beam diameter was about $15 \mu\text{m}$ (figure 7) when using a $3 \mu\text{m}$ step length. We have divided the Pb signal against ^{140}Ce in order to compensate for any drift in the primary beam intensity.

$$x = \sqrt{4Dt}$$

where x is the characteristic distance for diffusion (m)

D is the diffusion coefficient (m^2/s)

t is the duration (s) at fixed temperature

From the data of Smith and Giletti (1997), we can calculate that at 1200°C , a diffusion of only 40 nm would be generated in 5 days. This cannot be detected by EMP.

In the water experiments, the presence of both ThO_2 crystals and of a Th-poor layer in the newly formed monazites are related to the absence of SiO_2 in the initial solution. The starting material, containing Th, initially undergoes a dissolution step, which subsequently results in the precipitation of Pb-free monazite faces. Th is insoluble in water (Faure, 1986), consequently 1 atom of Si (Franz et al., 1996; Van Emden et al, 1997; Förster, 1998) is necessary for the following substitution conditions: $\text{Th}^{4+} + \text{Si}^{4+} = \text{REE}^{3+} + \text{P}^{5+}$. The Si, coming from the dissolved monazite, stays in the fluid and the insoluble Th precipitates as euhedral ThO_2 crystals. When SiO_2 is present in the initial solution neither ThO_2 crystals nor Th-poor layer appear. The dissolution of monazite and the subsequent formation of ThO_2 are prohibited by the presence of SiO_2 in the initial solution.

Strong chemical modification was observed only for the 1000°C - CaCl_2 experiment (Table 1 and Figure 3, 4 and 5). Only ~20 grains were recovered from the initial 30, showing that some grains were totally dissolved during the run. We interpret this as resulting from a dissolution/precipitation mechanism that operated in this run. Because the P-T conditions in this run were different from the conditions of formation of the starting monazite, the newly formed monazite has a distinctly new composition. Because very little is known about the thermodynamic of REE-phosphate and other monazite end-members, we cannot discuss in more detail the change in composition and the formation of the Th-rich limit. However, it seems likely that the starting monazite dissolved up to interface (1) and then began to crystallise from (1) to the grain margin (Figure 4). Because Th is very insoluble in the fluid, the first monazite that recrystallised was enriched in ThSiO_4 and because Y, HREE and U are less compatible the initial product was depleted in these elements. At a certain moment during the crystallisation process a progressive enrichment in U, Y and HREE was initiated.

A very important conclusion from this experiment was that Pb was not reincorporated into the newly formed monazite. This confirms the results of Teufel and Heinrich (1997) who showed that recrystallization is associated with strong discordancy. Finally, no self-diffusion of Pb or inter-diffusion of Ca-Pb were observed, even at the interface between the two zones where the optimal conditions for such diffusion were present. Relative to solid state diffusion, dissolution/precipitation is clearly a more efficient, faster mechanism for inducing discordancy.

More intense Pb-loss was observed in the experiment using CaCl₂ fluid (67% discordancy), than was the case with SrCl₂ (16% discordancy). This underlines the importance of the fluid composition in resetting process. However, in the run at 1000°C with SrCl₂ neither overgrowths nor chemical heterogeneity were observed. We cannot say at present if this discordancy results from simple Pb-loss from Sr-Pb exchange or from the formation of a small Pb-free-overgrowth, because neither dissolution features nor diffusion profiles were observed using SEM and EMP.

We have shown that no significant discordancy occurs at 1200°C/5 days/pure water, whereas at 1000°C/21 days/CaCl₂-fluid a 68% discordancy was present (Table 2). Temperature, and consequently volume diffusion, is not the most significant parameter which causes discordancy. As a consequence, the concept of “closure temperature” from Dodson (1973) must be invoked with extreme caution.

Our most surprising result relates to the Pb-enriched fluid experiments that however not reflect a “normal” geologic environment, as nature seldom provides such extremely Pb-enriched-fluid. The starting monazite ($^{208}\text{Pb}/^{206}\text{Pb}\sim 19.5$ and $^{207}\text{Pb}/^{206}\text{Pb}\sim 0.0566$) was mixed with NBS 982 standard ($^{208}\text{Pb}/^{206}\text{Pb}=1.00$ and $^{207}\text{Pb}/^{206}\text{Pb}=0.467$; Table 2). After experiments, the measured $^{208}\text{Pb}/^{206}\text{Pb}$ ratios of the monazite were ~ 17 at 800°C and ~ 18 at 1000°C; the measured $^{207}\text{Pb}/^{206}\text{Pb}$ ratios were ~ 0.058 at 800°C and ~ 0.057 at 1000°C. These lower $^{208}\text{Pb}/^{206}\text{Pb}$ and higher $^{207}\text{Pb}/^{206}\text{Pb}$ ratios are clearly related to a contamination of the monazite by the Pb-bearing fluid. In a $^{208}\text{Pb}/^{206}\text{Pb}$ vs. $^{207}\text{Pb}/^{206}\text{Pb}$ diagram (Figure 6f), both 800°C and 1000°C treated monazites plot significantly below the mixing line between the starting monazite and the NBS Pb spike. This implies that the decrease of ^{208}Pb relative to ^{206}Pb and ^{207}Pb is not the product just of a simple contamination mechanism. In the starting monazite $\sim 95\%$ of the Pb is ^{208}Pb . Consequently, if monazite is affected by a Pb-loss, the $^{208}\text{Pb}/^{206}\text{Pb}$ ratio will decrease. Additionally, the increase of ^{206}Pb and at a lower scale ^{208}Pb , observed on

the SIMS diagrams (Figure 8), implies a Pb-excess in the newly formed monazite rim, possibly the by-product of a $\text{Ca}_{\text{monazite}}\text{-Pb}_{\text{fluid}}$ exchange.

Using this mechanism for generating older ages in natural monazites is not realistic. The contamination of the starting monazite has clearly occurred. Furthermore, a highly ^{208}Pb enriched component apparently was leached out of the monazite (in fact this second mechanism must have involved a component which was $\gg 95\%$ ^{208}Pb). It is difficult to distinguish which phenomenon was the earliest and their relative intensity. The first one will produce Pb-excess in monazite and the second one the ^{208}Pb -loss. Two mechanisms are possible: (1) exchange involving both Pb-Pb self-diffusion and $\text{Ca}_{\text{monazite}}\text{-Pb}_{\text{fluid}}$ inter-diffusion, or (2) a partial dissolution of the starting monazite with a subsequent precipitation of newly grown monazite containing Pb predominantly derived from the fluid. This second of these hypothesis seems unlikely, because no dissolution features were visible in the 800°C -product and SIMS traverse suggest a diffusion profile rather than a sharp interface (Figure 8a). Consequently, at 800°C a diffusion mechanism is favoured, nevertheless the distance is not defined, because of the large ion beam diameter ($\sim 15\ \mu\text{m}$; Figure 7). At 1000°C , SEM images demonstrate that dissolution/precipitation was active (Figure 1h).

Finally, the results obtained on the experiments at 800°C and 1000°C suggest the activity of different mechanisms and, surprisingly, those occurring at 800°C apparently were much more efficient. This cannot be an artefact because of the good agreement between SIMS (Figure 8) and ID-TIMS (Figure 6) data, performed on different monazite fragments. However, an interpretation of that difference is tricky, because two parameters, temperature and duration, were different, associated with variations of kinetic and solubility.

6 - Conclusions

Significant dissolution-precipitation and corresponding discordancy only occurred for experiments with CaCl_2 or Pb-bearing fluids at 1000°C . In the case of experiments with a SrCl_2 fluid the effect was much weaker. Diffusion profiles were not observed for any element, including Pb. One exception may be for the 800°C experiment with Pb-bearing fluid. In that case, we propose as preliminary interpretation a Pb exchange via $\text{Pb}_{\text{fluid}}\text{-Ca}_{\text{monazite}}$ inter-diffusion, suggesting a mechanism for creating a Pb-excess in monazite. Additional to this exchange, it appears that ^{208}Pb may have been preferentially lost from the monazite products

of both the 800 and 1000°C experiments. Although this phenomenon is not well understood, we underline that this situation is not a “natural” condition, as nature seldom provides such extremely Pb-enriched-fluids. We conclude that dissolution/precipitation is the dominant mechanism by which the U-Pb monazite system can be modified and its impact depends both on the fluid composition and temperature.

The presence of Ca in the fluid has major consequences on U-Pb isotopic system of monazite. In nature a monazite frequently occurs as inclusions in either a plagioclase or a garnet. In this case, circulation of a fluid in the rock could mobilise the Ca from the host phase which can result in a partial or total resetting of monazite (De Wolf et al., 1993; Braun et al., 1998; Montel et al., 2000). If such a fluid is rich in SiO₂, then Th would be reincorporated into the monazite structure, favouring the crystallisation of a Th-rich and Pb-free rim. In natural samples Th-rich zones frequently occur. These latter are often younger, i.e., contain a lower Pb content than the adjacent domains (Cocherie et al., 1998; Crowley and Ghent, 1999). In the presence of intense deformation it is possible to obtain discordant U-Pb monazite ages, resulting from new overgrowths of Pb-free monazites produced by dissolution/precipitation (Krohe and Wawrzenitz, 2000). In nature, resetting (discordancy) by diffusion is unlikely. Fluid occurrences and compositions, and textural positions of the monazite in the rock (Paquette et al., 1999; Montel et al., 2000) are more important. The use of the closure temperature concept from Dodson (1973) must then be viewed with caution in the case of the U-Th-Pb system in monazite.

Acknowledgements

We would like to thank very much Moacyr Marinho who kindly provide us the monazite sample. We thank B. Wunder and R. Schulz for their help with the experiments using piston cylinder. Thanks to D. Rhede and O. Appelt for help with EMP analyses and imaging and U. Glenz for SEM. Our thanks go to E.M. Schemmert who produced good grain mounts.

Appendix: SIMS analytical details

Images used a 12.7 kV, 20 nA, ¹⁶O- primary beam which was rastered over an area of 150 x 150 µm. Samples were cleaned in ethanol, dried at 75°C and coated with a conductive gold film prior to analysis. The selected area for imaging was initially pre-sputtered in order

to remove the gold coat. Digital image acquisition, employing a resistive anode encoder, involved peak-stepping 20 times through the cycle: ^1H (8 seconds), ^{28}Si (8 s), ^{31}P (8 s), ^{40}Ca (8 s), ^{89}Y (8 s), ^{140}Ce (8 s), ^{206}Pb (60 s), ^{208}Pb (30 s), ^{232}Th (8 s), ^{238}U (30 s). Total analytical time per imaged area was thus some 65 minutes. For these analyses the mass spectrometer was operated at low mass resolving power employing a 10kV secondary ion extraction potential in conjunction with a 50V energy bandpass. In order to suppress artefacts due both to sample charging as well as from polyatomic ions a -80V bias was applied to our sample. The field-of-view for our images was circa 75 μm in diameter and our spatial resolution was better than 2 μm .

We employed a 0.1nA $^{16}\text{O}^-$ primary beam operated in shaped beam mode using a 100 μm primary L4 aperture. Subsequent measurements with both a stylus profilometer and using backscattered electron imaging (Figure 7) indicated a beam diameter of 12 μm of which circa 80% of the primary intensity was focused to a diameter of < 6 μm . An automatic 600s preburn was conducted prior to each analysis in order to sputter off the sample's gold coat and so that equilibrium sputtering conditions would be established. Our mass spectrometer was operated at low mass resolution ($M/\text{DM} = 400$) using a 400 μm contrast aperture in conjunction with a 60 μm diameter field-of-view. Isobaric molecular interferences were suppressed using a 100V offset voltage. Each analysis involved 50 cycles of the peak-stepping sequence: $^{139.5}\text{bkg}$ (0.1 seconds), ^{140}Ce (2 s), ^{206}Pb (10 s), ^{208}Pb (2 s), $^{208.5}\text{bkg}$ (0.1 s). A single analysis, including the 10 minutes preburn, lasted 24 minutes followed by an automatic 3 μm sample movement using the instrument's stepping motor.

References

- Bertrand, J.M., Roddick, J.C., Van Kranendonk, M.J. and Ermanovics I., 1993. U-Pb geochronology of deformation and metamorphism across a central transect of the Early Proterozoic Torngat Orogen, North River map area, Labrador. *Can. J. Earth Sci.*, 30, 1470-1489.
- Black, L.P., Fitzgerald, F.D. and Harley, S.L., 1984. Pb isotopic composition, colour, and microstructure of monazites from a polymetamorphic rock in Antarctica. *Contrib. Mineral. Petrol.*, 85, 141-181.

- Braun, I., Montel, J.M. and Nicollet, C., 1998. Electron microprobe dating of monazites from high-grade gneisses and pegmatites of the Kerala Khondalite Belt, southern India. *Chem. Geol.*, 146, 65-85.
- Childe, F., Doig, R. and Gariépy, C., 1993. Monazite as a metamorphic chronometer, south of the Grenville Front, western Quebec. *Can. J. Earth Sci.*, 30, 1056-1065.
- Cocherie, A., Legendre, O., Peucat, J.J. and Kouamelan, A.N., 1998. Geochronology of polygenetic monazites constrained by in situ electron microprobe Th-U-total lead determination: implications for lead behaviour in monazite. *Geochim. Cosmochim. Acta*, 62, 2475-2497.
- Copeland, P. and Parrish, R.R., 1988. Identification of inherited radiogenic Pb in monazite and its implications for U-Pb systematics. *Nature*, 333, 760-763.
- Corfu F., 1988. Differential response of U-Pb systems in coexisting accessory minerals, Winnipeg River Subprovince, Canadian Shield: implications for Archean crustal growth and stabilisation. *Contrib. Mineral. Petrol.*, 98, 312-325.
- Crowley, J.L. and Ghent, E.D., 1999. An electron microprobe study of the U-Th-Pb systematics of metamorphosed monazite: the role of Pb diffusion versus overgrowth and recrystallization. *Chem. Geol.*, 157, 285-302.
- Cruz, M.J., Cunha, J.C., Merlet, C. and Sabaté, P., 1996. Datação pontual das monazitas da região de Itambé, Bahia, através da microsonda eletrônica. XXXIX Congresso Brasileiro de Geologia.
- De Wolf, C.P., Belshaw, N. and O’Nions, R.K., 1993. A metamorphic history from micron-scale $^{207}\text{Pb}/^{206}\text{Pb}$ chronometry of Archean monazite. *Earth Planet. Sci. Lett.*, 120, 207-220.
- Dodson, M.H., 1973. Closure temperature in cooling geochronological and petrological systems. *Contrib. Mineral. Petrol.*, 40, 257-259.

- Faure, G., 1986. Principles of isotope geology. Second edition. New York.
- Förster, H.J., 1998a. The chemical composition of REE-Y-Th-U-rich accessory minerals in peraluminous granites of the Erzgebirge-Fichtelgebirge region, Germany, Part I: The monazite-(Ce)-brabantite solid solution series. *Am. Mineral.*, 83, 1302-1315.
- Förster, H.J., 1998b. The chemical composition of REE-Y-Th-U-rich accessory minerals in peraluminous granites of the Erzgebirge-Fichtelgebirge region, Germany, Part II: xenotime. *Am. Mineral.*, 83, 259-272.
- Franz, G., Andrehs, G. and Rhede, D., 1996. Crystal chemistry of monazite and xenotime from Saxothuringian-Moldanubian metapelites, NE Bavaria, Germany. *Eur. J. Mineral.*, 8, 1097-1118.
- Grove, M. and Harrison, T.M., 1999. Monazite Th-Pb age depth profiling. *Geology*, 27, 487-490.
- Harrison, T.M., McKeegan, K.D. and LeFort, P., 1995. Detection of inherited monazite in the Manaslu leucogranite by $^{208}\text{Pb}/^{232}\text{Th}$ ion microprobe dating: Crystallization age and tectonic implications. *Earth Planet. Sci. Lett.*, 133, 271-282.
- Kalt, A., Corfu, F. and Wijbrans, J.R., 2000. Time calibration of a P-T path from a Variscan high-temperature low-pressure metamorphic complex (Bayerische Wald, Germany), and the detection of inherited monazite. *Contrib. Mineral. Petrol.*, 128, 143-163.
- Krogh, T.E., 1982. Improved accuracy of U-Pb zircon ages by the creation of more concordant systems using an air abrasion technique. *Geochim. Cosmochim. Acta*, 46, 637-649.
- Krohe, A. and Wawrzenitz, N., 2000. Domainal variations of U-Pb monazite ages and Rb-Sr whole-rock dates in polymetamorphic paragneisses (KTB Drill Core, Germany): influence of strain and deformation mechanisms on isotope systems. *J. Metamorphic Geol.*, 18, 271-291.

- Landzirotti, A. and Hanson, G.N., 1995. U-Pb dating of major and accessory minerals formed during metamorphism and deformation of metapelites. *Geochim. Cosmochim. Acta*, 59, 2513-2526.
- Montel, J.M., Foret, S., Veschambre, M., Nicollet, C. and Provost, A., 1996. Electron microprobe dating of monazite. *Chem. Geol.*, 131, 37-53.
- Montel, J.M., Kornprobst, J. and Vielzeuf, D., 2000. Preservation of old U-Th-Pb ages in shielded monazite: example from the Beni Bousera Hercynian kinzigites (Morocco). *J. Metamorphic Geol.*, 18, 335-342.
- Paquette, J.L., Montel, J.M. and Chopin, C., 1999. U-Th-Pb dating of the Brossasco ultrahigh-pressure metagranite, Dora-Maira massif, western Alps. *Eur. J. Mineral.*, 11, 69-77.
- Parrish, R.R., 1987. An improved micro-capsule for zircon dissolution in U-Pb geochronology. *Chem. Geol., Isot. Geosci.*, 66, 99-102.
- Parrish, R.R., 1990. U-Pb dating of monazite and its application to geological problems. *Can J. Earth Sci.*, 27, 1431-1450.
- Parrish, R.R., 1995. Thermal evolution of the southeastern Canadian Cordillera. *Can J. Earth Sci.*, 32, 1618-1642.
- Pin, C. and Paquette, J.L., 1997. A mantle-derived bimodal suite in the Hercynian Belt: Nd isotope and trace element evidence for a subduction-related rift origin of the Late Devonian Brévenne metavolcanics, Massif Central (France). *Contrib. Mineral. Petrol.*, 129, 222-238.
- Poitrasson, F., Chenery, S. and Bland, D.J., 1996. Contrasted monazite hydrothermal alteration mechanisms and their geochemical implications. *Earth Planet. Sci. Lett.*, 145, 79-96.

- Poitrasson, F., Chenery, S. and Shepherd, T.J., 2000. Electron microprobe and LA-ICP-MS study of monazite hydrothermal alteration: Implications for U-Th-Pb geochronology and nuclear ceramics. *Geochim. Cosmochim. Acta.*, 64, 3283-3297.
- Rubatto, D., Williams, I.S. and Buick, I.S., 2001. Zircon and monazite response to prograde metamorphism in the Reynolds Range, central Australia., *Contrib. Mineral. Petrol.*, 140, 458-468.
- Schärer, U., Xu, R.H. and Allègre, C.J., 1986. U-(Th)-Pb systematics and ages of Himalayan leucogranites, South Tibet. *Earth Planet. Sci. Lett.*, 77, 35-48.
- Seydoux-Guillaume, A.M., Wirth, R., Nasdala, L., Gottschalk, M., Montel, J.M. and Heinrich, W., submitted. XRD, TEM and raman study of experimental annealing of natural monazite. Submitted in *Phys. Chem. Mineral.*
- Shannon, R.D., 1976. Revised effective ionic radii and systematic studies of interatomic distances in halide and chalcogenides. *Acta Cryst.*, 32, 751-767.
- Simpson, R.L., Parrish, R.R., Searle, M.P. and Waters, D.J., 2000. Two episodes of monazite crystallization during metamorphism and crustal melting in the Everest region of the Nepalese Himalaya. *Geology*, 28, 403-406.
- Smith, H.A. and Barreiro, B., 1990. Monazite U-Pb dating of staurolite grade metamorphism in pelitic schists. *Contrib. Mineral. Petrol.*, 105, 602-615.
- Smith, H.A. and Giletti, B.J., 1997. Lead diffusion in monazite. *Geochim. Cosmochim. Acta*, 61, 1047-1055.
- Suzuki, K. and Adachi, M., 1994. Middle Precambrian detrital monazite and zircon from the Hida gneiss on Oki-Dogo Island, Japan: their origin and implications for the correlation of basement gneiss of Southwest Japan and Korea. *Tectonophysics*, 235, 277-292.
- Suzuki, K., Adachi M. and Kajizuka I., 1994. Electron microprobe observations of Pb diffusion in metamorphosed detrital monazites. *Earth Plan. Sci. Lett.*, 128, 391-405.

- Teufel, S. and Heinrich, W., 1997. Partial resetting of the U-Pb isotope system in monazite through hydrothermal experiments: an SEM and U-Pb isotope study. *Chem. Geol.*, 137, 273-281.
- Townsend, K.J., Miller, C.F., D'Andrea, J.L., Ayers, J.C., Harrison, T.M. and Coath, C.D., 2001. Low temperature replacement of monazite in the Ireteba granite, Southern Nevada: geochronological implications. *Chem. Geol.*, 172, 95-112.
- Van Emden, B., Thornber, M.R., Graham, J. and Lincoln, F.J., 1997. The incorporation of actinides in monazite and xenotime from placer deposits in western Australia. *Can. Mineral.*, 35, 95-104.
- Vielzeuf, D. and Montel, J.M., 1994. Partial melting of metagreywackes, Part I: Fluid-absent experiments and phase relationships. *Contrib. Mineral. Petrol.*, 117, 375-393.
- Williams, M. L., Jercinovic, M.J. and Terry, M.P., 1999. Age mapping on the electron microprobe: Deconvoluting multistage tectonic histories. *Geology*, 27, 1023-1026.
- Zhu, X.K. and O'Nions, R.K., 1999. Zonation of monazite in metamorphic rocks and its implications for high temperature thermochronology: a case study from the Lewisian terrain. *Earth Planet. Sci. Lett.*, 171, 209-220.
- Zhu, X.K., O'Nions, R.K., Belshaw, N.S. and Gibb, A.J., 1997. Significance of in situ SIMS chronometry of zoned monazite from the Lewisian granulites, northwest Scotland. *Chem. Geol.*, 135, 35-53.

Conclusions

“Pour le savant, croire la science achevée est toujours une illusion aussi complète que le serait pour l’historien de croire l’histoire terminée.”

Louis de Broglie - *Physique et microphysique*

CONCLUSIONS

In this thesis we first tried to understand how Th is partitioned between monazite and xenotime and if this distribution has an influence on the $\text{CePO}_4\text{-YPO}_4$ geothermometer. It has been demonstrated that for a ThSiO_4 content in the bulk composition of 0.1 or 0.2 mole fraction, Th was almost partitioned in monazite. The incorporation of ThSiO_4 depends on the X_{ThSiO_4} content, whereas Y incorporation is more temperature dependent. Xenotime is apparently Th-free. For a ThSiO_4 content in the bulk composition of 0.5 mole fraction, thorite is additionally formed for temperature $<1000^\circ\text{C}$. This indicates a saturation of monazite (and xenotime), i.e. solvus between monazite and thorite (and thorite and xenotime) has been intersected. Above 1000°C only monazite, a small amount of xenotime and no thorite were present. This indicates that the solvus shrinks considerably at high temperatures. All ThSiO_4 is also partitioned between monazite and xenotime. The position of the solvus depends on the Th content present in the system and also on the phases present. Our results show that the interpretation of the calculated temperatures using the Y-partitioning between monazite and xenotime should be treated with caution. The Th content in monazite has to be taking into account.

The structure investigations of a natural, chemically homogeneous monazite crystal concordant at 474 Ma (2.5×10^{16} α/mg accumulated), indicate that the crystal consists of two domains (A) and (B), which are basically two monazite crystals with slightly different lattice parameters. Diffraction domains (A), showing sharp reflections with high amplitude, are assigned to a well-crystallised lattice with small volume expansion (1%). Diffraction domains (B), exhibiting very broad reflections with low amplitude, represent a distorted lattice, which can be referred to old alpha-recoil tracks. It is suggested that the (A) domains correspond to well-crystallised areas, within which He atoms are trapped, causing an expansion of the lattice. Diffraction domains (B) are interpreted as a distorted monazite crystal lattice composed of “islands” with an expanded lattice (interstitials), and “islands” of a compressed monazite lattice, (vacancies). Both the “islands” will pose stress (compression and/or dilatation) on the lattice in the vicinity. The broadening of the (B)-reflections is due to the expanded/compressed diffraction domains and due to the different amount of the distortion. Therefore, in the (B) domains, He cannot accumulate because quality of the crystal net is very poor, unable to trap atoms.

The behaviour of this monazite under healing was investigated. With increasing temperature, alpha-recoil-tracks are healed, i.e. diffraction domains (B) progressively disappear. At the same time, He diffuses out of the monazite lattice, inducing a relaxation of the lattice resulting in a volume decrease. At 900°C only one phase remains that is a monazite with well-crystallised lattice and minimum unit-cell volume. This study confirms the good crystallinity observed for most of natural monazites. In natural samples, Pb-diffusion will occur predominantly within a pristine, organised crystal structure. Because it is known that Pb-diffusion in monazite is very slow (Suzuki et al. 1994; Smith and Giletti 1997), we suggest that Pb-diffusion will not be an efficient mechanism for resetting.

In a third part, experiments on the same monazite as used in part II were focused on the understanding of the resetting mechanisms of the U-Pb isotope system. It could be shown that dissolution/precipitation is the predominant mechanism by which the U-Pb monazite system can be modified and its extension is strongly dependent on the fluid composition. At 1000°C in a CaCl₂ fluid significant dissolution/precipitation, demonstrated by presence of inherited core and newly formed Ca-rich/Pb-free monazite rim, and corresponding discordancy (68%), occurred. In the case of a fluid with SrCl₂ the effect is weaker (16% discordancy). In a pure water fluid, no significant modifications are visible even at 1200°C/5 days. Temperature, and consequently volume diffusion, was never observed in our study except for the very particular experiment at 800°C using Pb-spike. Therefore, we propose that volume diffusion is neither the only nor the most significant parameter that causes discordancy. In nature, resetting (discordancy) by diffusion is most therefore unlikely, whereas fluid occurrences, fluid compositions, and textural positions of the monazite in the rock (Paquette et al., 1999; Montel et al., 2000) are the most important parameters. As a consequence, the concept of “closure temperature” from Dodson (1973) must be viewed with extreme caution.

Experiments with Pb-bearing fluid demonstrated the possibility to create a Pb-excess in monazite, maybe by a Pb exchange via Pb_{fluid}-Ca_{monazite} inter-diffusion. Additional to this exchange, it appears that ²⁰⁸Pb may have been preferentially lost from the monazite products of both the 800 and 1000°C experiments. Although this phenomenon is not well understood, we underline that this situation is not a “natural” condition, as nature seldom provides such extremely Pb-enriched-fluids.

Each part of the thesis was done with other authors and the papers were submitted in different international journals:

PartI:

Seydoux-Guillaume A.M., Wirth R., Heinrich W. and Montel J.M. Experimental determination of the Th partitioning between monazite and xenotime using Analytical Electron Microscopy. *Submitted to European Journal of Mineralogy.*

PartII:

Seydoux-Guillaume A.M., Wirth R., Nasdala L., Gottschalk M., Montel J.M. and Heinrich W. An XRD and TEM study of an experimentally annealed monazite. *Accepted in Physics and Chemistry of Minerals*

Nasdala, L., Lengauer, C.L., Hanchar, J.M., Kronz, A., Blanc, P., Kennedy, A.K., **Seydoux-Guillaume A.M.** Annealing metamictisation and the recovery of cathodoluminescence. *Submitted to Chemical Geology*

PartIII:

Seydoux-Guillaume A.M., Paquette J.L., Wiedenbeck M., Montel J.M. and Heinrich W. Experimental resetting of the U-Th-Pb system in monazite. *Submitted to Chemical Geology*

References

“Quand nous avons soif, il nous semble que nous pourrions boire tout un océan: c’est la foi; et quand nous nous mettons à boire, nous buvons un verre ou deux: c’est la science.”

Anton Tchekhov - *Calepin*

References

- Andrehs, G. & Heinrich, W. (1998):** Experimental determination of REE distributions between monazite and xenotime: potential for temperature-calibrated geochronology. *Chem. Geol.*, **149**, 83-96.
- Barth, S., Oberli, F., Meier, M. (1994):** Th-Pb versus U-Pb isotope systematics in allanite from co-genetic rhyolite and granodiorite: implications for geochronology. *Earth Planet. Sci. Lett.*, **124**, 149-159.
- Bea, F. (1996):** Residence of REE, Y, Th and U in Granites and crustal protholiths; implications for the chemistry of crustal melts. *J. Petrol.*, **37**, 521-552.
- Bertrand, J.M., Roddick, J.C., Van Kranendonk, M.J., Ermanovics, I. (1993):** U-Pb geochronology of deformation and metamorphism across a central transect of the Early Proterozoic Torngat Orogen, North River map area, Labrador. *Can. J. Earth Sci.*, **30**, 1470-1489.
- Berzelius, J.J. (1829):** Undersokning at ett nytt mineral (Thorit). *Akad. Stockholm Handl.*, **1**, not seen, cited in Smitts, 1989.
- Black, L.P., Fitzgerald, F.D., Harley, S.L. (1984):** Pb isotopic composition, colour, and microstructure of monazites from a polymetamorphic rock in Antarctica. *Contrib. Mineral. Petrol.*, **85**, 141-181.
- Boatner, L.A., Abraham, M.M., Rappaz, M. (1981):** The characterization of nuclear waste forms by EPR spectroscopy. In: *Scientific Basis for Nuclear Waste Management*, Moore JG (ed), **3**, 181-188 Plenum Press New York.
- Boatner, L.A., Beall, G.W., Abraham, M.M., Finch, C.B., Huray, P.G., Rappaz, M. (1980):** Monazite and other lanthanide orthophosphates as alternative actinide waste forms. In: *Scientific Basis for Nuclear Waste Management*, Northrup Jr CJM (ed), **2**, 289-296 Plenum Press New York.
- Boatner, L.A. & Sales, B.C. (1988):** Monazite. In: *Radioactive Waste Forms for the Future*. Lutze W, Ewing RC (ed), 495-564 Elsevier.
- Braun, I., Montel, J.M., Nicollet, C. (1998):** Electron microprobe dating of monazites from high-grade gneisses and pegmatites of the Kerala Khondalite Belt, southern India. *Chem. Geol.*, **146**, 65-85.
- Cherniak, D.J. (1993):** Lead diffusion in titanite and preliminary results on the effect of radiation damage on Pb transport. *Chem. Geol.*, **110**, 177-194.
- Cherniak, D.J., Lanford, W.A., Ryerson, F.J. (1991):** Lead diffusion in apatite and zircon using ion implantation and Rutherford back-scattering techniques. *Geochim. Cosmochim. Acta*, **55**, 1663-1673.
- Childe, F., Doig, R., Gariépy, C. (1993):** Monazite as a metamorphic chronometer, south of the Grenville Front, western Quebec. *Can. J. Earth Sci.*, **30**, 1056-1065.
- Cliff, G. & Lorimer, G.W. (1975):** The quantitative analysis of thin specimens. *J. Microsc.*, **103**, 203-207.

- Cocherie, A., Legendre, O., Peucat, J.J., Kouamelan, A.N. (1998):** Geochronology of polygenetic monazites constrained by in situ electron microprobe Th-U-total lead determination: implications for lead behavior in monazite. *Geochim. Cosmochim. Acta*, **62**, 2475-2497.
- Copeland, P. & Parrish, R.R. (1988):** Identification of inherited radiogenic Pb in monazite and its implications for U-Pb systematics. *Nature*, **333**, 760-763.
- Corfu, F. (1988):** Differential response of U-Pb systems in coexisting accessory minerals, Winnipeg River Subprovince, Canadian Shield: implications for Archean crustal growth and stabilization. *Contrib. Mineral. Petrol.*, **98**, 312-325.
- Crowley, J.L. & Ghent, E.D. (1999):** An electron microprobe study of the U-Th-Pb systematics of metamorphosed monazite: the role of Pb diffusion versus overgrowth and recrystallization. *Chem. Geol.*, **157**, 285-302.
- Cruz, M.J., Cunha, J.C., Merlet, C., Sabaté, P. (1996):** Datação pontual das monazitas da região de Itambé, Bahia, através da microsonda eletrônica. *XXXIX Congresso Brasileiro de Geologia*.
- De Wolf, C.P., Belshaw, N., O'Nions, R.K. (1993):** A metamorphic history from micron-scale $^{207}\text{Pb}/^{206}\text{Pb}$ chronometry of Archean monazite. *Earth Planet. Sci. Lett.*, **120**, 207-220.
- Devidal, J.L. & Montel, J.M. (1999):** Crystal chemistry of the brabantite-monazite group. *EUG X, J. Conf. Abstract.*, **4**, 524.
- Dodson, M.H. (1973):** Closure temperature in cooling geochronological and petrological systems. *Contrib. Mineral. Petrol.*, **40**, 257-259.
- Egerton, R.F. (1996):** Electron energy-loss spectroscopy in the electron microscope. *Plenum Press, New York*, 301-306.
- Erichsen, L.V. (1951):** Über die Heliumabgabe von Monazit in abhängigkeit von Gasphase, Druck und Temperatur. *N. Jahrb. Mineral. Monatshefte*, 25-33.
- Ewing, R.C. (1975):** The crystal chemistry of complex niobium and tantalum oxides IV The metamict state: Discussion. *Am. Mineral.*, **60**, 728-733.
- Ewing, R.C., Chakoumakos, B.C., Lumpkin, G.R., Murakami, T., Gregor, R.B., Lytle, F.W. (1988):** Metamict minerals: natural analogues for radiation damage effects in ceramic nuclear waste forms. *Nucl. Instr. Meth.* **B32**, 487-497.
- Ewing, R.C., Meldrum, A., Wang, L.M., Wang, S.X. (2000):** Radiation-Induced Amorphization. In: *Reviews in Mineralogy and Geochemistry*, Ribbe PH (ed), **39**, 319-361 Mineralogical Society of America, Washington DC.
- Ewing, R.C., Weber, W.J., Clinard, F.W. Jr. (1995):** Radiation effects in nuclear waste forms. *Progress. Nucl. Energy*, **29**, 63-127.

- Faure, G. (1986):** Principles of isotope geology. *Second edition. New York.*
- Firestone, R.B. & Shirley, V.S. (1996):** Table of isotopes 2. *John Wiley & Sons Inc, C5-C6.*
- Förster, H.J. (1998a):** The chemical composition of REE-Y-Th-U-rich accessory minerals in peraluminous granites of the Erzgebirge-Fichtelgebirge region, Germany, Part I: The monazite-(Ce)-brabantite solid solution series. *Am. Mineral.*, **83**, 259-272.
- (1998b): The chemical composition of REE-Y-Th-U-rich accessory minerals in peraluminous granites of the Erzgebirge-Fichtelgebirge region, Germany, Part II: Xenotime. *Am. Mineral.*, **83**, 1302-1315.
- Franz, G., Andrehs, G., Rhede, D. (1996):** Crystal chemistry of monazite and xenotime from Saxothuringian-Moldanubian metapelites, NE Bavaria, Germany. *Eur. J. Mineral.*, **8**, 1097-1118.
- Gögen, K. & Wagner, G.A. (2000):** Alpha-recoil track dating of Quaternary volcanics. *Chem. Geol.*, **166**, 127-137.
- Gratz, R. & Heinrich, W. (1997):** Monazite-xenotime thermobarometry: experimental calibration of the miscibility gap in the binary system $\text{CePO}_4\text{-YPO}_4$. *Am. Mineral.*, **82**, 772-780.
- (1998): Monazite-xenotime thermobarometry. III. Experimental calibration of the partitioning of Gd between monazite and xenotime. *Eur. J. Mineral.*, **10**, 579-588.
- Grove, M. & Harrison, T.M. (1999):** Monazite Th-Pb age depth profiling. *Geology*, **27**, 487-490.
- Harlov, D. & Förster, H.J.:** High grade fluid metasomatism on both a local and regional scale: the Seward Peninsula, Alaska and the Val Strona di Omega, Ivrea-Verbano Zone, Northern Italy. Part II: phosphate mineral chemistry. *In Press in J. Petrol.*
- Harrison, T.M., McKeegan, K.D., LeFort, P. (1995):** Detection of inherited monazite in the Manaslu leucogranite by $^{208}\text{Pb}/^{232}\text{Th}$ ion microprobe dating: Crystallization age and tectonic implications. *Earth Planet. Sci. Lett.*, **133**, 271-282.
- Heinrich, W., Andrehs, G., Franz, G. (1997):** Monazite-xenotime miscibility gap thermometry: I. An empirical calibration. *J. Metamorphic Geol.*, **15**, 3-17.
- Holland, H.D. & Gottfried, D. (1955):** The effect of nuclear radiation on the structure of zircon. *Acta Crystallogr.*, **8**: 291-300.
- Irmer, G. (1985):** Zum Einfluß der Apparatefunktion auf die Bestimmung von Streuquerschnitten und Lebensdauern aus optischen Phononenspektren. *Exper. Techn. Phys.*, **33**, 501-506.
- Joy, D.C., Romig, A.D., Goldstein, J.I. (1989):** Principles of analytical electron microscopy. *Plenum Press New-York and London.*

- Kalt, A., Corfu, F., Wijbrans, J.R. (2000):** Time calibration of a P-T path from a Variscan high-temperature low-pressure metamorphic complex (Bayerische Wald, Germany), and the detection of inherited monazite. *Contrib. Mineral. Petrol.*, **128**, 143-163.
- Karioris, F.G., Appaji Gowda, K., Cartz, L. (1981):** Heavy ion bombardment of monoclinic ThSiO₄, ThO₂ and monazite. *Rad. Eff. Lett.*, **58**, 1-3.
- Krogh, T.E. (1982):** Improved accuracy of U-Pb zircon ages by the creation of more concordant systems using an air abrasion technique. *Geochim. Cosmochim. Acta*, **46**, 637-649.
- Krohe, A. & Wawrzenitz, N. (2000):** Domainal variations of U-Pb monazite ages and Rb-Sr whole-rock dates in polymetamorphic paragneisses (KTB Drill Core, Germany): influence of strain and deformation mechanisms on isotope systems. *J. Metamorphic Geol.*, **18**, 271-291.
- Landzirotti, A. & Hanson, G.N. (1995):** U-Pb dating of major and accessory minerals formed during metamorphism and deformation of metapelites. *Geochim. Cosmochim. Acta*, **59**, 2513-2526.
- Larson, A.C. & Von Dreele, R.B. (1988):** GSAS-Generalized structure analysis system. *Los Alamos National Laboratory Report LAUR*, **86-758**, 1-150.
- Lumpkin, G.L. & Ewing, R.C. (1988):** Alpha-decay damage in minerals of the pyrochlore groups. *Phys. Chem. Mineral.*, **16**, 2-20.
- Meldrum, A., Boatner, L.A., Ewing, R.C. (1997):** Electron-irradiation-induced nucleation and growth in amorphous LaPO₄, ScPO₄, and zircon. *J. Matter. Res.*, **12**, 1816-1827.
- (2000): A comparison of radiation effects in crystalline ABO₄-type phosphates and silicates. *Mineral. Mag.*, **64**, 183-192.
- Meldrum, A., Boatner, L.A., Weber, W.J., Ewing, R.C. (1998):** Radiation damage in zircon and monazite. *Geochim. Cosmochim. Acta*, **62**, 2509-2520.
- Meldrum, A., Boatner, L.A., Zinkle, S.J., Wang, S.X., Wang, L.M., Ewing, R.C. (1999):** Effects of dose rate and temperature on the crystalline-to-metamict transformation in the ABO₄ orthosilicates. *Can. Mineral.*, **37**, 207-221.
- Meldrum, A., Wang, L.M., Ewing, R.C. (1996):** Ion-beam-induced amorphization of monazite. *Nucl. Instr. Meth. Phys. Res.*, **B116**, 220-224.
- Montel, J.M. & Seydoux, A.M. (1998):** Sm-Nd interdiffusion in monazite. *EMPG VII, Terra Abst. Suppl. 1 to Terra Nova*, **10**, 42.
- Montel, J.M., Foret, S., Veschambre, M., Nicollet, C., Provost, A. (1996):** Electron microprobe dating of monazite. *Chem. Geol.*, **131**, 37-53.

- Montel, J.M., Kornprobst, J., Vielzeuf, D. (2000):** Preservation of old U-Th-Pb ages in shielded monazite: example from the Beni Bousera Hercynian kinzigites (Morocco). *J. Metamorphic Geol.*, **18**, 335-342.
- Murakami, T., Chakoumakos, B.C., Ewing, R.C. (1986):** X-Ray Powder Diffraction Analysis of Alpha-Event Radiation Damage in Zircon ($ZrSiO_4$). In: *Advances in ceramics: Nuclear waste management II*, Clark DE, White WB and Machiels J (ed) **20**, 745-753 American Ceramic Society, Columbus, Ohio.
- Murakami, T., Chakoumakos, B.C., Ewing, R.C., Lumpkin, G.R., Weber, W.J. (1991):** Alpha-decay event damage in zircon. *Am. Mineral.*, **76**, 1510-1532.
- Nabelek, P.I. & Glascock, M.D. (1995):** REE-depleted leucogranites, Black Hills, South Dakota: a consequence of disequilibrium melting of monazite-bearing schists. *J. Petrol.*, **36**, 1055-1071.
- Nasdala, L., Finger, F., Kinny, P. (1999):** Can monazite become metamict? *Eur. J. Mineral.*, **11**, Beih 1, 164.
- Nasdala, L. & Massonne, H-J. (2000):** Microdiamonds from the Saxonian Erzgebirge, Germany: in situ micro-Raman characterisation. *Eur. J. Mineral.*, **12**, 495-498.
- Nasdala, L., Pidgeon, R.T., Wolf, D. (1996):** Heterogeneous metamictization of zircon on a microscale. *Geochim. Cosmochim. Acta*, **60**, 1091-1097.
- Nasdala, L., Wenzel, M., Andrut, M., Wirth, R., Blaum, P. (2001a):** The nature of radiohaloes in biotite. *Am. Mineral.*, **86**, 498-512.
- Nasdala, L., Wenzel, M., Vavra, G., Irmer, G., Wenzel, T., Kober, B. (2001b):** Metamictisation of natural zircon: Accumulation versus thermal annealing of radioactivity-induced damage. *Contrib. Mineral. Petrol.*, **141**, 125-144.
- Nasdala, L., Wolf, D., Irmer, G. (1995):** The degree of metamictization in zircon: a Raman spectroscopic study. *Eur. J. Mineral.*, **7**, 471-478.
- Ni, Y., Hughes, J.M., Mariano, A.N. (1995):** Crystal chemistry of the monazite and xenotime structures. *Am. Mineral.*, **80**, 21-26.
- Ouchani, S., Dran, J.C., Chaumont, J. (1997):** Evidence of ionization annealing upon helium-ion irradiation of pre-damaged fluorapatite. *Nucl. Instr. Meth. Phys. Res.*, **B132**, 447-451.
- Overstreet, W.C. (1967):** The geological occurrence of monazite. *U.S.G.S., Prof. Paper 530*.
- Owen, M.R. (1988):** Radiation-damage halos in quartz. *Geology*, **16**, 529-532.
- Pabst, A. & Hutton, C.O. (1951):** Huttonite a new monoclinic thorium silicate. *Am. Mineral.*, **36**, 60-69.
- Paquette, J.L., Montel, J.M., Chopin, C. (1999):** U-Th-Pb dating of the Brossasco ultrahigh-pressure metagranite, Dora-Maira massif, western Alps. *Eur. J. Mineral.*, **11**, 69-77.

- Parrish, R.R. (1987):** An improved micro-capsule for zircon dissolution in U-Pb geochronology. *Chem. Geol., Isot. Geosci.*, **66**, 99-102.
- (1990): U-Pb dating of monazite and its application to geological problems. *Can J. Earth Sci.*, **27**, 1431-1450.
- (1995): Thermal evolution of the southeastern Canadian Cordillera. *Can. J. Earth Sci.*, **32**, 1618-1642.
- Parrish, R.R. & Carr, S.R. (1994):** U-Pb problematics of very high-U accessory minerals: examples from the Himalaya and Cordillera and implication for U-Pb geochronology. *Abstract ICOG 8, U.S.G.S. Circular*, **1107**, p. 128.
- Pin, C. & Paquette, J.L. (1997):** A mantle-derived bimodal suite in the Hercynian Belt: Nd isotope and trace element evidence for a subduction-related rift origin of the Late Devonian Brévenne metovolcanics, Massif Central (France)., *Contrib. Mineral. Petrol.*, **129**, 222-238.
- Podor, R. (1995):** Raman spectra of the actinide-bearing monazites. *Eur. J. Mineral.*, **7**, 1353-1360.
- Podor, R. & Cuney, M. (1995):** Experimental study of the solid solution between monazite-(La) and $(\text{Ca}_{0.5}\text{U}_{0.5})\text{PO}_4$ at 780°C and 200 MPa. *Am. Mineral.*, **80**, 1261-1268.
- (1997): Experimental study of Th-bearing LaPO_4 (780°C, 200 MPa): implications for monazite and actinide orthophosphate stability. *Am. Mineral.*, **82**, 765-771.
- Poitrasson, F., Chenery, S., Bland, D.J. (1996):** Contrasted monazite hydrothermal alteration mechanisms and their geochemical implications. *Earth Planet. Sci. Lett.*, **145**, 79-96.
- Poitrasson, F., Chenery, S., Shepherd, T.J. (2000):** Electron microprobe and LA-ICP-MS study of monazite hydrothermal alteration: Implications for U-Th-Pb geochronology and nuclear ceramics. *Geochim. Cosmochim. Acta.*, **64**, 3283-3297.
- Pyle, J.M., Spear, F.S., Rudnick, R.L., McDonough, W.F. (2001):** Monazite-xenotime-garnet equilibrium in metapelites and a new monazite-garnet-thermometer. *J. Petrol.*, **42**, 2083-2107.
- Rubatto, D., Williams, I.S., Buick, I.S. (2001):** Zircon and monazite response to prograde metamorphism in the Reynolds Range, central Australia., *Contrib. Mineral. Petrol.*, **140**, 458-468.
- Salje, E.K.H. (2000):** Structural transformations in minerals The role of temperature and radiation damage. *Berichte der Deutschen Mineralogischen Gesellschaft, Beihefte zum Eur. J. Miner.*, **12**, 175.
- Salje, E.K.H., Chrosch, J., Ewing, R.C. (1999):** Is “metamictization” of zircon a phase transition? *Am. Mineral.*, **84**, 1107-1116.
- Schärer, U., Xu, R.H., Allègre, C.J. (1986):** U-(Th)-Pb systematics and ages of Himalayan leucogranites, South Tibet. *Earth Planet. Sci. Lett.*, **77**, 35-48.

- Seydoux, A.M., Montel, J.M., Paquette, J.L., Marinho, M. (1999):** Experimental study of the resetting of the U-Th-Pb geochronological system of monazite. *EUG X, Terra Nova 10, Abst. Suppl.*, **1**, 800.
- Seydoux, A.M. & Montel, J.M. (1997):** Experimental determination of the Thorite-Huttonite phase transition. *EUG IX, Terra Nova 9 Abst. Suppl.*, **1**, 421.
- Seydoux-Guillaume A.M. & Montel J.M.:** Experimental investigation of the thorite-huttonite phase transition. *Submitted in European Journal of Mineralogy.*
- Seydoux-Guillaume, A.M., Paquette, J.L., Wiedenbeck, M., Montel, J.M., Heinrich, W.:** Experimental resetting of the U-Th-Pb system in monazite. *Submitted to Chem. Geol.*
- Seydoux-Guillaume, A.M., Wirth, R., Nasdala, L., Gottschalk, M., Montel, J.M., Heinrich, W.:** An XRD, TEM and Raman study of an experimentally annealed monazite. *Submitted to Phys. Chem. Mineral.*
- Shannon, R.D. (1976):** Revised effective ionic radii and systematic studies of interatomic distances in halide and chalcogenides. *Acta Cryst.*, **32**, 751-767.
- Simpson, R.L., Parrish, R.R., Searle, M.P., Waters, D.J. (2000):** Two episodes of monazite crystallization during metamorphism and crustal melting in the Everest region of the Nepalese Himalaya. *Geology*, **28**, 403-406.
- Smith, H.A. & Barreiro, B. (1990):** Monazite U-Pb dating of staurolite grade metamorphism in pelitic schists. *Contrib. Mineral. Petrol.*, **105**, 602-615.
- Smith, H.A. & Giletti, B.J. (1997):** Lead diffusion in monazite. *Geochim. Cosmochim. Acta*, **61**, 1047-1055.
- Speer, J.A. (1982):** Zircon. *In: Reviews in Mineralogy Ribbe PH (ed)*, **5**, 67-112. *Mineralogical Society of America, Washington DC.*
- Suzuki, K. & Adachi, M. (1994):** Middle Precambrian detrital monazite and zircon from the Hida gneiss on Oki-Dogo Island, Japan: their origin and implications for the correlation of basement gneiss of Southwest Japan and Korea. *Tectonophysics*, **235**, 277-292.
- Suzuki, K., Adachi, M., Kajizuka I. (1994):** Electron microprobe observations of Pb diffusion in metamorphosed detrital monazites. *Earth Plan. Sci. Lett.*, **128**, 391-405.
- Taylor, M. & Ewing, R.C. (1978):** The crystal structures of ThSiO₄ polymorphs: huttonite and thorite. *Acta Crystallogr.*, **B34**, 1074-1079.
- Teufel, S. & Heinrich, W. (1997):** Partial resetting of the U-Pb isotope system in monazite through hydrothermal experiments: an SEM and U-Pb isotope study. *Chem. Geol.*, **137**, 273-281.
- Townsend, K.J., Miller, C.F., D'Andrea, J.L., Ayers, J.C., Harrison, T.M., Coath, C.D. (2001):** Low temperature replacement of monazite in the Ireteba granite, Southern Nevada: geochronological implications. *Chem. Geol.*, **172**, 95-112.

- Van Emden, B., Thornber, M.R., Graham, J., Lincoln, F.J. (1997):** The incorporation of actinides in monazite and xenotime from placer deposits in western Australia. *Can. Mineral.*, **35**, 95-104.
- Vielzeuf, D. & Montel, J.M. (1994):** Partial melting of metagreywackes, Part I: Fluid-absent experiments and phase relationships. *Contrib. Mineral. Petrol.*, **117**, 375-393.
- Viskupic, K. & Hodges, K.V. (2001):** Monazite-xenotime thermochronometry: methodology and an example from the Nepalese Himalaya. *Contrib. Mineral. Petrol.*, **141**, 233-247.
- Weber, W.J., Ewing, R.C., Catlow, C.R.A., Diaz de la Rubia, T., Hobbs, L.W., Kinoshita, C., Matzke, H.J., Motta, A.T., Nastasi, M., Salje, E.H.K., Vance, E.R., Zinkle, S.J. (1998):** Radiation effects in crystalline ceramics for the immobilization of high-level nuclear waste and plutonium. *J. Mater. Res.*, **13**, 1434-1484.
- Weber, W.J., Ewing, R.C., Wang, L.M. (1994):** The radiation-induced crystalline-to-amorphous transition in zircon. *J. Mater. Res.*, **9**, 688-698.
- Williams, M.L., Jercinovic, M.J., Terry, M.P. (1999):** Age mapping on the electron microprobe: Deconvoluting multistage tectonic histories. *Geology*, **27**, 1023-1026.
- Zhu, X.K. & O'Nions, R.K. (1999):** Zonation of monazite in metamorphic rocks and its implications for high temperature thermochronology: a case study from the Lewisian terrain. *Earth Planet. Sci. Lett.*, **171**, 209-220.
- Zhu, X.K., O'Nions, R.K., Belshaw, N.S., Gibb, A.J. (1997):** Significance of in situ SIMS chronometry of zoned monazite from the Lewisian granulites, northwest Scotland. *Chem. Geol.*, **135**, 35-53.

Acknowledgements



First, I would like to thank my two supervisors **Jean-Marc Montel** and **Wilhelm Heinrich** who gave me the opportunity to work on my PhD at the GFZ-Potsdam.

Mon plus grand merci revient à **Jean-Marc**, mon directeur historique. Il m'a mis le pied à l'étrier de la minéralogie expérimentale il y a 5 ans à Clermont et m'a ainsi donné le goût du travail expérimental. C'est également grâce à lui que j'ai pu faire cette thèse. Merci pour votre aide toujours présente et votre confiance envers ma valeur scientifique.

Herzlichen Dank auch an **Wilhelm Heinrich**, meinem deutschen Betreuer, der mich gut am GFZ aufgenommen hat. Ich bin dafür dankbar, daß mir der experimentelle und analytische Gerätepool des GFZ zur Verfügung stand, um den mich viele französische Doktoranden beneiden, denn viele der wissenschaftlichen Arbeiten hätten nicht in Frankreich gemacht werden können.

Merci à **Jean-Louis Paquette** pour son apprentissage de la chimie isotopique, son humour toujours décapant ainsi que son acharnement à corriger mon anglais et mon style déplorable.

Herzlichen Dank zum **Richard Wirth** für sein Vertrauen, das TEM allein zu benutzen, den theoretischen und praktischen TEM Unterrichten, und seine Geduld mir alles zu erklären.

Vielen Dank an **Matthias Gottschalk** für die sehr interessante Diskussionen, für seine präzise und konstruktive Korrekturen und für die viele Zeit, die er verbrachte, um mir die Rietveld Methode beizubringen.

Danke an **Michael Wiedenbeck** für seinen Einsatz, um meine Probe mit der SIMS zu messen.

Bernd Wunder, **Stefan Melzer** und **Reiner Schulz** für die Hilfe beim Experimentieren, **Oona Appelt** und **Dieter Rhede** für die Hilfe an der Mikrosonde, **Frau Glenz** für ihren Beistand am REM, **Frau Pech** und **Frau Schemmert** für das Präparieren meiner Proben, dem ganzes P.B. 4.1 - Besten Dank.

Merci **Damien** pour ton amour, ton soutien, ton respect et ta compréhension dans mes choix, surtout celui de venir faire ma thèse à Potsdam.

A **mes parents**, merci pour leur soutien aussi bien financier que moral tout au long de mes études et leur compréhension et respect de mes choix.

Enfin, merci à **Gaël** mon frère adoré, ma p'tite soeur (belle) **Marion**, les **Bisounours**, **Cath**, **AnneV**, **Bruno**, **Filip**, **François** et **Karine**, **Birgit**, **Alex Fabienne** et **Thommy**, **Nancy Florian** et **Judith**, toute l'équipe de **hand SCC**...et tous ceux que j'ai oublié.